



Ramakrishna Mission Residential College (Autonomous)
Kolkata 700103, WB, India

Collaborative research in coordination chemistry of organic radicals
Number 12

Institute 1: Ramakrishna Mission Residential College (Autonomous)

Concerned Faculty: Dr. Prasanta Ghosh, Dept of Chemistry
&

Institute 2: Max-Planck-Institut für Chemische Energiekonversion

Stiftstrasse 34 - 36 / D - 45470 Mülheim an der Ruhr

Concerned Scientist: Dr Thomas Weyhermüller

Period of Investigation: 02-02-2016 to 27-10-2016

Project: Anion radical complexes of oxidovanadium(IV)

Output: The result was published in a journal of international repute

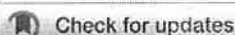
Publication: Coordination of *o*-benzosemiquinonate, *o*-iminobenzosemiquinonate and aldimine anion radicals to oxidovanadium(IV)

Madhusudan Shit, Suvendu Maity, Sachinath Bera, Thomas Weyhermüller and Prasanta Ghosh*

New J. Chem., 2017, 41, 4564-4572.


Dr. Prasanta Ghosh

Dr Thomas Weyhermüller



Cite this: *New J. Chem.*, 2017, 41, 4564

Coordination of *o*-benzosemiquinonate, *o*-iminobenzosemiquinonate and aldimine anion radicals to oxidovanadium(IV)[†]

Madhusudan Shit,^{ab} Sachinath Bera,^a Suvendu Maity,^a Thomas Weyhermüller^c and Prasanta Ghosh^{ab} 

The study focuses on the stabilization of organic radicals by the oxidovanadium(IV) ion and it proves to be significant in exploring the bioactivity of vanadium. In addition to the *o*-benzosemiquinonate and *o*-iminobenzosemiquinonate anion radicals, the existence of reactive aldimine anion radicals coordinated to oxidovanadium(IV) ion was detected. Radical and non-radical oxidovanadium(IV) complexes of the types $[(L_1^-)(VO)(acac)]$ (1), $[(L_2^-)(VO)(acac)]$ (2), $[(L_1^-)(VO)(sq^{\bullet-})]$ (3), $[(L_1^-)(VO)(t-Bu_{sq}^{\bullet-})]$ (4), $[(L_1^-)(VO)(NO_2isq^{\bullet-})]$ (5) and $[(L_1)_2(VO)_2(SO_4)] \cdot \frac{1}{2}CH_2Cl_2$ ($6 \cdot \frac{1}{2}CH_2Cl_2$) containing redox non-innocent tridentate NNO-donor aldimines (L_1H and L_2H) as coligands are reported ($acac$ = acetylacetonato, $sq^{\bullet-}$ = *o*-benzosemiquinonate, $t-Bu_{sq}^{\bullet-}$ = 3,5-di-*tert*-butyl-*o*-benzosemiquinonate and $NO_2isq^{\bullet-}$ = *p*-nitro-*o*-iminobenzosemiquinonate anion radicals). The $sq^{\bullet-}$, $t-Bu_{sq}^{\bullet-}$ and $NO_2isq^{\bullet-}$ states in complexes were established by X-ray crystallography, EPR spectroscopy and solid state cross polarization magic angle spinning (CP/MAS) ^{51}V NMR spectroscopy, where the ^{51}V nuclei in **3–5** were deshielded in a range from –100.3 to +608.7 ppm. The cathodic waves of **1** and **2** due to $L_1^-/L_1^{\bullet-}$ and $L_2^-/L_2^{\bullet-}$ redox couples are reversible. Density functional theory (DFT) calculations authenticated that **1**^{•–} and **2**^{•–} are open shell pi radical ($L_1^{\bullet-}$ and $L_2^{\bullet-}$) complexes of oxidovanadium(IV). The energies of the open shell singlet (OSS) and triplet solutions of **1**^{•–} and **2**^{•–} are lower than the corresponding closed shell singlet (CSS) solutions. In **1**^{•–} and **2**^{•–} ions, 35–39% beta spin is localized on the $\pi_{aldimine}^*$ function. The UV-vis-NIR absorption spectra of the complexes were analyzed by spectroelectrochemical measurements and time dependent (TD) DFT calculations.

Received 16th January 2017,
Accepted 26th April 2017

DOI: 10.1039/c7nj00186j

rsc.li/njc

Introduction

The diverse activities of the organic radicals in biology¹ and catalysis² act as stimuli for the development of the coordination chemistry of organic radicals in the laboratory. Numerous organic radicals are now documented; however, it should be mentioned that the types of organic radicals are still very limited in scope. Stabilization of the organic radicals in metal complexes is an ongoing challenge in chemical research. Semiquinonate anion radicals³ are relatively more stable, while phenoxyl,⁴ thiyl,⁵ aminyl,⁶ and azo-anion⁷ radicals are reactive, having shorter lifetimes.

The stabilization of the α -diimine anion radicals has been successful in several instances.⁸ Participation of these anion radicals in the catalytic cycle of the olefin polymerization reaction is also documented. The iminopyridine anion radical complexes of transition metal ions were also reported.⁹ Notably, the formation of the aldimine anion radical in the vast coordination chemistry of salicylaldimines¹⁰ has not been documented to date. In this study, the same was investigated with the oxidovanadium(IV) ion.

Recently, it was disclosed that the oxidovanadium(IV) ion, which is bioactive,¹¹ is an agent that can stabilize reactive organic radicals coupling anti-ferromagnetically.¹² The literature reveals that oxidovanadium complexes of aldimines are functional.¹⁰ The oxidovanadium complexes of salicylaldimine and salicylaldehyde hydrazones were considered as potential anti-cancer drugs.¹³ Oxidovanadium complexes of salicylaldehyde hydrazones exhibit insulin mimicking activities.¹⁴ Thus, the coordination chemistry of the oxidovanadium ion with redox active aldimine ligands is a worthwhile investigation.

It was documented that the VO(*o*-benzosemiquinonate) fragment is oxidizing, while the VO(*o*-iminobenzosemiquinonate) is reducing

^a Department of Chemistry, R. K. Mission Residential College, Narendrapur, Kolkata-103, India. E-mail: ghosh@pghosh.in

^b Department of Chemistry, Dinabandhu Andrews College, Garia, Kolkata-84, India

^c Max-Planck-Institut für Chemische Energiekonversion, Stiftstr. 34-36, 45470 Mülheim an der Ruhr, Germany

[†] Electronic supplementary information (ESI) available: Crystallographic parameter, bond lengths, ESI-mass, fluid solution ^{51}V NMR, IR and UV-vis/NIR spectra, gas phase optimize coordinates. CCDC 1506825–1506828. For ESI and crystallographic data in CIF or other electronic format see DOI: 10.1039/c7nj00186j

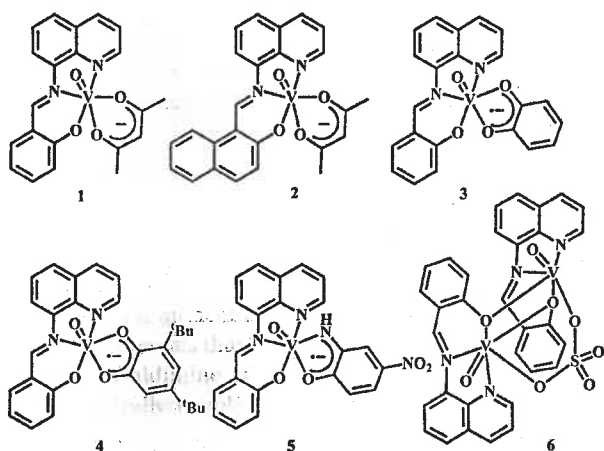


Chart 1 Isolated mono and dinuclear oxidovanadium(IV) complexes.

in nature.¹² In this search, the coordination chemistry of the oxidovanadium ion with NNO donor aldimines using particularly catechols and aminophenols as coligands was explored. Acetylacetonato (acac), *o*-benzosemiquinonato ($\text{sq}^{\bullet-}$) and 3,5-di-*tert*-butyl-*o*-benzosemiquinonato ($^t\text{-Bu}\text{sq}^{\bullet-}$) and *p*-nitro-*o*-iminobenzosemiquinonato ($^{\text{NO}_2}\text{isq}^{\bullet-}$) complexes of oxido vanadium(IV) of the types $[(\text{L}_1^-)(\text{V}^{\text{IV}}\text{O})(\text{acac})]$ (1), $[(\text{L}_2^-)(\text{V}^{\text{IV}}\text{O})(\text{acac})]$ (2), $[(\text{L}_1^-)(\text{V}^{\text{IV}}\text{O})(\text{sq}^{\bullet-})]$ (3), $[(\text{L}_1^-)(\text{V}^{\text{IV}}\text{O})(^t\text{-Bu}\text{sq}^{\bullet-})]$ (4) and $[(\text{L}_1^-)(\text{V}^{\text{IV}}\text{O})(^{\text{NO}_2}\text{isq}^{\bullet-})]$ (5) as depicted in Chart 1 were successfully isolated, where L_1^- and L_2^- are tridentate NNO-donor aldimine ligands. In addition, a dinuclear complex of the type $[(\text{L}_1^-)_2(\text{V}^{\text{IV}}\text{O})_2(\text{SO}_4)] \cdot \frac{1}{2}\text{CH}_2\text{Cl}_2$ ($6 \cdot \frac{1}{2}\text{CH}_2\text{Cl}_2$), was authenticated.

This study reveals that L_1H and L_2H are redox active, and the formation of aldimine anion radicals ($\text{L}_1^{\bullet 2-}$ and $\text{L}_2^{\bullet 2-}$) anti-ferromagnetically coupled to the oxidovanadium(IV) ion was successfully detected. The molecular and electronic structures of the complexes were confirmed by single crystal X-ray crystallography, electron paramagnetic resonance (EPR) and solid state cross polarization magic angle spinning (CP/MAS) ^{51}V nuclear paramagnetic resonance (NMR) spectroscopy and density functional theory (DFT) calculations.

Experimental

Materials and methods

Catechol (cat), 3,5-di-*tert*-butylcatechol ($^t\text{-Bu}\text{cat}$), 2-amino-4-nitrophenol ($^{\text{NO}_2}\text{ap}$) and 8-aminoquinoline were purchased from Sigma-Aldrich and analytical-grade salicylaldehyde, acetylacetone, vanadyl sulphate were obtained from commercial suppliers and used without further purification. The synthetic precursors L_1H and L_2H ^{15a,b} and $\text{VO}(\text{acac})_2$ ^{15c} were prepared by reported procedures. Spectroscopic-grade solvents were used for spectroscopic and electrochemical measurements. The C, H, and N contents of the compounds were obtained using a PerkinElmer 2400 Series II elemental analyzer. The elemental analyses were performed after evaporating the solvents under high vacuum. Infrared spectra of the samples were measured from 4000 to 400 cm^{-1} with KBr pellets at 295 K on a PerkinElmer

Spectrum RX 1 Fourier transform infrared (FT-IR) spectrophotometer. ^1H spectra in CDCl_3 were recorded on a Bruker DPX 500 MHz spectrometer. ^{51}V NMR spectra in CDCl_3 solution were recorded on Bruker AV 400 spectrometer, and chemical shifts were measured referenced to an aqueous solution of ammonium metavanadate at -574.3 ppm. Solid state CP/MAS analyses were carried out on a JEOL ECX 400 spectrometer, and chemical shifts were measured referenced to the isotropic peak of V_2O_5 at -612 ppm. Mass spectra were recorded on a LCMS 2020 with a dedicated ESI probe, using LCMS Lab solution software. Electronic absorption spectra of the solutions of the complexes were recorded on a PerkinElmer Lambda 750 spectrophotometer in the range of 3300–175 nm. The X-band EPR spectra were recorded on a Magnetech GmbH MiniScope MS400 spectrometer, where the microwave frequency was measured with an FC400 frequency counter. The EPR spectra were simulated using the EasySpin software.¹⁶ The electro-analytical instrument BASi Epsilon-EC in CH_2Cl_2 containing 0.2 M tetra-butylammonium hexafluorophosphate as supporting electrolyte was used for cyclic voltammetric experiments. The BASi platinum working electrode, platinum auxiliary electrode, Ag/AgCl reference electrode were used for the measurements. The redox potential data were referenced to ferrocenium/ferrocene, Fc^+/Fc , couple. BASi SEC-C thin-layer quartz glass spectroelectrochemical cell kit (light path length of 1 mm) with platinum gauze working electrode and SEC-C platinum counter electrode were used for spectroelectrochemistry measurements.

Syntheses

(*E*)-2-((Quinolin-8-ylimino)methyl)phenol (L_1H) and (*E*)-1-((quinoline-8-ylimino)methyl)naphthalen-2-ol (L_2H) were prepared following a reported procedure.^{15a}

$[(\text{L}_1^-)(\text{V}^{\text{IV}}\text{O})(\text{acac})]$ (1). To L_1H (248 mg, 1.00 mmol) methanol (20 mL) was added and heated at 325 K to produce a clear solution. To this solution, $\text{VO}(\text{acac})_2$ (262 mg, 1.00 mmol) in CH_2Cl_2 (5 mL) was added. The resulting solution was allowed to evaporate slowly in air at 295 K. After 4–5 days, green crystals of 1 separated out, which were collected upon filtration and washed with two portions (5 mL) of di-ethylether and dried in air. Yield: 280 mg, 0.67 mmol ($\sim 67\%$ with respect to vanadium). Mass spectral data [electrospray ionization (ESI) positive ion, CH_3OH]: m/z 413 for $[\text{1}]^+$. Anal. calcd for $\text{C}_{21}\text{H}_{18}\text{N}_2\text{O}_4\text{V}$: C, 61.02; H, 4.39; N, 6.78; found: C, 60.85; H, 4.37; N, 6.75. IR/ cm^{-1} (KBr): ν 2900(m, $-\text{CH}_3$), 1606(s, $\text{C}=\text{N}$), 1590(s, $\text{C}=\text{N}_{\text{py}}$), 1532(m, acac), 1514(s, acac), 1507(s), 1463(m), 1429(m), 1403(m), 1391(m), 1320(m), 1313(m), 1149(m), 940(s, $\text{V}=\text{O}$), 834(m), 763(m).

$[(\text{L}_2^-)(\text{V}^{\text{IV}}\text{O})(\text{acac})]$ (2). 2 was similarly prepared following the above procedure using L_2H (298 mg, 1.00 mmol). Yield: 340 mg, 0.73 mmol ($\sim 73\%$ with respect to vanadium). Mass spectral data [electrospray ionization (ESI) positive ion, CH_3OH]: m/z 463 for $[\text{2}]^+$. Anal. calcd for $\text{C}_{25}\text{H}_{20}\text{N}_2\text{O}_4\text{V}$: C, 64.80; H, 4.35; N, 6.05; found: C, 64.53; H, 4.33; N, 6.02. IR/ cm^{-1} (KBr): ν 2916(m, $-\text{CH}_3$), 1618(s, $\text{C}=\text{N}$), 1600(s, $\text{C}=\text{N}_{\text{py}}$), 1537(m, acac), 1510(m, acac),

1458(m), 1425(m), 1383(m), 1303(m), 1258 (m), 1383(s), 1142(m), 940(s) (V=O), 827(m), 752(m).

$[(L_1^-)(V^VO)(sq^{*-})]$ (3). To L_1H (248 mg, 1.00 mmol) methanol (20 mL) was added and heated at 325 K to leave a clear solution. To this solution, $VO(acac)_2$ (262 mg, 1.00 mmol) in CH_2Cl_2 (5 mL), followed by catechol (110.0 mg, 1.00 mmol) in methanol (5 mL) were added. The resultant solution was allowed to evaporate slowly in air. After 4–5 days, a green mass of 3 separated out, which was collected upon filtration and washed with two portions (5 mL) of di-ethylether and dried in air. Yield: 210 mg, 0.50 mmol (~60% with respect to vanadium). Mass spectral data [electrospray ionization (ESI) positive ion, CH_3OH]: m/z 422 for $[3]^+$, 346 for $[3-sq + MeOH]^+$. Anal. calcd for $C_{22}H_{15}N_2O_4V$: C, 62.57; H, 3.58; N, 6.63; found: C, 62.15; H, 3.52; N, 6.58. δ 9.13 (s, 1H), 8.69 (d, 1H), 8.40 (d, 1H), 8.04 (d, 1H), 7.89 (d, 2H), 7.79 (t, 1H), 7.66–7.54 (m, 3H), 7.10 (d, 2H), 6.90–6.77 (m, 3H), ppm. IR/ cm^{-1} (KBr): ν 3056(m), 1606(s, C=N), 1588(s C=N_{py}), 1532(s), 1514(s), 1428(m), 1386(s), 1319(m), 1267(m), 1149(m), 940(s) (V=O), 834(m), 763(m).

$[(L_1^-)(V^VO)(t-Bu sq^{*-})]$ (4). 4 (black crystals) was similarly prepared by the procedure described for 3 using 3,5-di-*tert*-butylcatechol, $t-Bu cat$ (222.0 mg, 1.00 mmol). Yield: 320 mg, 0.60 mmol (~60% with respect to vanadium). Mass spectral data [electrospray ionization (ESI) positive ion, CH_3OH]: m/z 535 for $[4]^+$, 377 for $[4-t-Bu sq + 2MeOH]^+$, 346 for $[4-t-Bu sq + MeOH]^+$. Anal. calcd for $C_{30}H_{31}N_2O_4V$: C, 67.41; H, 5.85; N, 5.24; found: C, 67.15; H, 5.82; N, 5.22. 1H NMR ($CDCl_3$, 300 MHz, 300 K): δ 9.07 (s, 1H), 8.68 (d, 1H), 8.37 (d, 1H), 8.02 (d, 1H), 7.84 (d, 1H), 7.75 (t, 1H), 7.65 (t, 3H), 7.06 (d, 1H), 6.79 (t, 1H), 6.12 (s, 1H), 6.13 (s, 1H), 1.56 (s, 18H) ppm. IR/ cm^{-1} (KBr): ν 2950(m, *t*-Bu), 2922(m, *t*-Bu), 2857(m, *t*-Bu), 1606(s, C=N), 1586(s, C=N_{py}), 1532(s), 1507(s), 1462(s), 1398(s), 1431(s), 1385(m), 1358(m), 1324(m), 1240(m), 1212 (m), 1149(m), 932(s) (V=O), 755(m).

$[(L_1^-)(V^VO)(NO_2 isq^{*-})]$ (5). 5 (black crystals) was similarly prepared using *p*-nitro-*o*-aminophenol, $NO_2 ap$, (144.0 mg, 1.0 mmol). Yield: 280 mg, 0.60 mmol (~60% with respect to vanadium). Mass spectral data [electrospray ionization (ESI) positive ion, CH_3OH]: m/z 467 for $[5]^+$, 346 for $[5-NO_2 isq + MeOH]^+$. Anal. calcd for $C_{22}H_{15}N_4O_5V$: C, 55.65; H, 3.24; N, 12.01; found: C, 55.45; H, 3.24; N, 11.97. 1H NMR ($CDCl_3$, 300 MHz, 300 K): δ 14.65 (s, NH), 9.18 (s, 1H), 8.76 (d, 1H), 8.60 (d, 1H), 8.44 (t, 3H), 8.16 (d, 1H), 8.01 (d, 1H), 7.84 (s, 1H), 7.61 (d, 1H), 7.47 (d, 1H), 7.04 (s, 1H), 6.79 (d, 1H), 6.57 (d, 1H) ppm. IR/ cm^{-1} (KBr): ν 3420(m, -NH), 1606(s, C=N), 1588(m, C=N_{py}), 1578(m), 1532(m), 1508(m), 1464(m), 1429(m), 1385(m), 1308(s, -NO₂), 1267(m), 1214(m), 1149(s), 940(m) (V=O), 755(m).

$[(L_1^-)_2(V^VO)_2(SO_4)] \cdot \frac{1}{2}CH_2Cl_2$ ($6\frac{1}{2}CH_2Cl_2$). To L_1H (248 mg, 1.00 mmol), a mixture of methanol and CH_2Cl_2 (3:1, 40 mL) and $VOSO_4$ (163 mg, 1.00 mmol) was added. The reaction mixture was refluxed for 30 min and was allowed to evaporate slowly in air. After 7 days, yellow crystals of $6\frac{1}{2}CH_2Cl_2$ separated out, which were collected upon filtration and washed with two

portions (5 mL) of di-ethylether and dried in air. Yield: 220 mg, 0.30 mmol (~60% with respect to vanadium). Mass spectral data [electrospray ionization (ESI) positive ion, CH_3OH]: m/z 727 for $[6]^+$, 659 for $[6-SO_4 + MeOH]^+$, 346 for $[VO(L_1)(MeOH)]^+$. Anal. calcd for $C_{32}H_{22}N_4O_8SV_2$: C, 53.05; H, 3.06; N, 7.73; found: C, 52.83; H, 3.05; N, 7.69. IR/ cm^{-1} (KBr): ν 3428(b), 2925(m), 1604(s), 1539(m), 1507(m), 1464(m), 1436(m), 1382(m), 1296(m), 1217(m), 1149(m), 1125(m), 938(s) (V=O), 877(s), 834(m), 751(m).

Single crystal X-ray structural determination of the complexes (CCDC 1506825–1506828)

Dark single crystals of 1, 4, 5 and $6\frac{1}{2}CH_2Cl_2$ were picked with nylon loops and mounted on a Bruker APEX-II CCD and a Bruker AXS D8 QUEST ECO diffractometer equipped with a Mo-target rotating-anode X-ray source and a graphite monochromator (Mo $K\alpha$, $\lambda = 0.71073$ Å). Final cell constants were obtained from least-square fits of all measured reflections. Intensity data were corrected for absorption using intensities of redundant reflections. The structures were readily solved by direct methods and subsequent difference Fourier techniques. The Siemens SHELXS-97^{17a} software package was used for solution, and SHELXL-97^{17b} was used for the refinement and XS. Ver. 2013/1,^{17c} XT. Ver. 2014/4^{17d} and XL. Ver. 2014/7^{17e} were used for structure solution and refinement. All non-hydrogen atoms were refined anisotropically. Hydrogen atoms were placed at the calculated positions and refined as riding atoms with isotropic displacement parameters.

Density functional theory (DFT) calculations

All calculations reported in this article were done with the Gaussian 03W¹⁸ program package supported by GaussView 4.1. The DFT¹⁹ and time-dependent (TD) DFT²⁰ calculations were performed at the level of Becke three parameter hybrid functional with the nonlocal correlation functional of Lee–Yang–Parr (B3LYP).²¹ Gas-phase geometries of 1^- and 2^- were optimized with singlet spin state, while 1 and 2 were optimized with doublet spin state, using Pulay's Direct Inversion²² in the Iterative Subspace (DIIS), "tight" convergent self-consistent field procedure²³ ignoring symmetry. All calculations were performed with a LANL2DZ basis set,²⁴ along with the corresponding effective core potential (ECP) for vanadium, 6-31+G*(d,p)²⁵ basis set for C, O, N atoms, and 6-31G²⁶ for H atoms. The closed shell singlet (CSS) solutions of 1^- and 2^- , are unstable, and the solutions were re-optimized with open shell singlet states. In both cases the energies of OSS solutions that are stable are lower than the CSS solutions. The 60 lowest singlet excitation energies on each of the optimized geometries of 4 and 5 were elucidated by TD DFT calculations.

Results and discussion

Syntheses and characterization

L_1H and L_2H were isolated from the reactions of 8-amioquinoline and salicylaldehyde or 2-hydroxynaphthaldehyde in boiling ethanol. The reactions of L_1H and L_2H with $VO(acac)_2$ in methanol at 295 K afforded 1–2 in good yields. Isolations of bis(L_1) and bis(L_2)

complexes of the types $[(L_1^-)_2VO]$ and $[(L_2^-)_2VO]$ did not succeed; however, the reaction of $VOSO_4$ with excess L_1H in boiling methanol generated a sulfato bridged dinuclear complex, **6**. To investigate the redox activities of the $VO(o\text{-benzosemiquinonate})$ and $VO(o\text{-iminobenzosemiquinonate})$ fragments having L_1^- and L_2^- as coligands, **3**, **4** and **5** were isolated from the reactions of $VO(acac)_3$ with L_1H and catechol (cat) or 3,5-di-*tert*-butylcatechol (*t*-Bu²cat) or *p*-nitro-*o*-aminophenol (NO_2ap) at 295 K using air as an oxidizing agent. A similar reaction with un-substituted *o*-aminophenol did not yield any crystalline product. Details of the procedures are outlined in the Experimental section. The complexes were characterized by elemental analyses: 1H and ^{51}V NMR, mass (see Fig. S2–S7, ESI†) and IR spectroscopy (see Fig. S8–S11, ESI†). The analytical and the selected spectral data are listed in the syntheses section. Notably, the $V=O$ stretching frequencies of **1–6** appear at 940, 940, 940, 932, 940 and 938 cm^{-1} respectively.

Assignment of the electronic states of the complexes

The X-ray crystallography, redox activity, EPR spectral and solid state CP/MAS ^{51}V NMR spectroscopy, and density functional theory (DFT) calculations, as discussed below, were used to authenticate the electronic structures of the complexes. We failed to characterize complexes **2** and **3** by single crystal X-ray crystallography. However, the compositions of **2** and **3** were authenticated by mass and IR spectra (see Fig. S8–S11, ESI†). The electronic states were elucidated by comparing the cyclic voltammograms and the EPR spectra of (**1**, **2**) and (**3**, **4**) pairs (*vide infra*).

X-ray crystallography

The crystallographic data of **1**, **4**, **5** and $6 \cdot \frac{1}{2}CH_2Cl_2$ are summarized in Table S1 (ESI†). **1** crystallizes in the $P2_1/c$ space group. The molecular geometry of **1** in crystals with the atom labeling scheme is illustrated in Fig. 1 and the selected bond parameters are summarized in Table 1. The VO_4N_2 octahedron is distorted. The $V-N_{imine}$ length is relatively shorter than $V-N_{py}$ length and two $V-O_{acac}$ lengths are different. The $V=O$ length is $1.614(2)\text{ \AA}$. The $V-O_{phenolato}$ length, $1.951(2)\text{ \AA}$, *cis* to $V=O$ bond correlates well to those of the oxidovanadium(IV) complexes.¹² The $V-O(21)$

Table 1 Selected experimental bond lengths (\AA) of **1** and the calculated bond lengths of **1** and **1**[−]

	Exp.		Calcd	
	1	1	1 -(OSS)	1 -(triplet)
$V(1)-O(1)_{phenolato}$	1.951(2)	1.959	1.992	1.946
$V(1)-N(9)_{imine}$	2.076(2)	2.101	2.067	2.083
$V(1)-N(18)_{py}$	2.129(2)	2.157	2.186	2.135
$V(1)-O(21)_{acac}$	2.144(2)	2.244	2.333	2.308
$V(1)-O(25)_{acac}$	1.989(2)	2.002	2.026	2.052
$V(1)-O(30)_{oxo}$	1.614(2)	1.589	1.598	1.592
$C(8)-N(9)$	1.299(2)	1.309	1.324	1.329

length, $2.144(2)\text{ \AA}$, is relatively longer than $V-O(25)$ length, $1.989(2)\text{ \AA}$, which may be due to the stronger trans effect of $V=O$ bond.^{12d} The $C=N$ length is $1.299(2)\text{ \AA}$.

4 crystallizes in the $P2_1/c$ space group. The gross geometry of **4** as shown in Fig. 2(a) is similar to that of **1**, where only the redox innocent acac ligand is replaced by a redox non-innocent dioxolene ligand. The bis-deprotonated catecholato complexes of oxidovanadium(IV) are rare,^{11a,12a,f} however, mono-deprotonated catecholato complexes of oxidovanadium(IV) are documented.²⁷ **4** can be expressed by two electronic states as depicted in Scheme 1. The $V-O_{phenolato}$, $V-N_{py}$ and $V-N_{imine}$ lengths, listed in Table 2, are similar to those of **1**. Moreover, the average C–O lengths of the dioxolene ligand, 1.305 \AA , are relatively shorter and the C–C lengths of the phenyl ring exhibit a quinoidal distortion, two shorter lengths being $1.388(2)$ and $1.381(2)\text{ \AA}$.

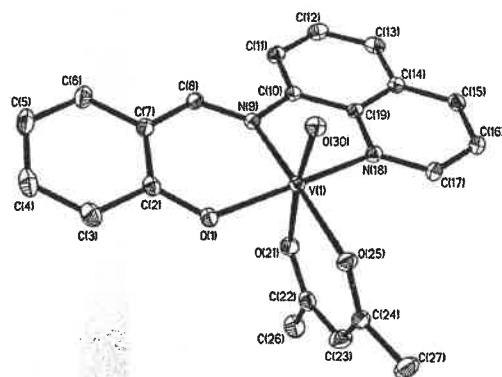


Fig. 1 Molecular geometry of (a) **1** in crystals (40% thermal ellipsoid, and H atoms are omitted for clarity).

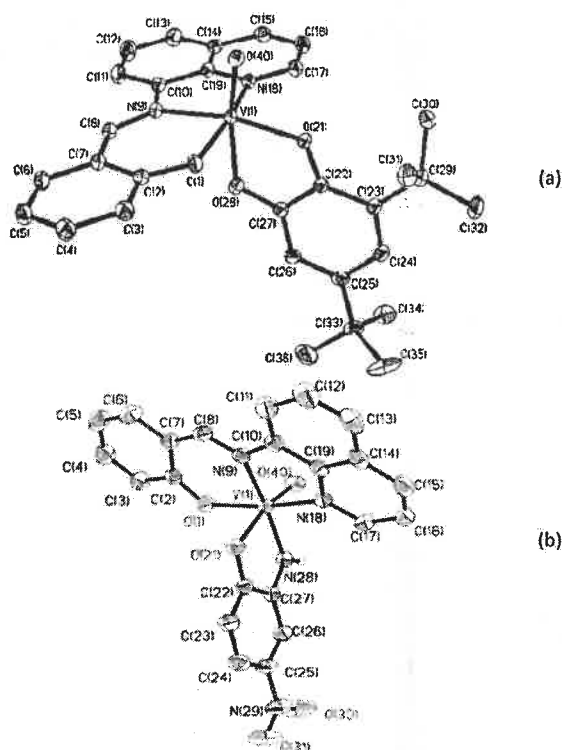


Fig. 2 Molecular geometries of (a) **4** and (b) **5** in crystals (40% thermal ellipsoid, and H atoms are omitted for clarity).

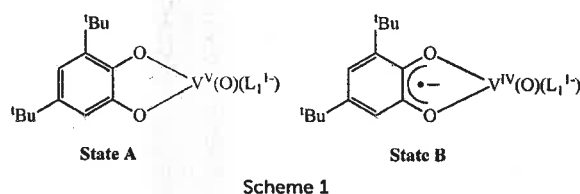


Table 2 Selected experimental bond lengths (Å) of **4** and **5** and the corresponding calculated bond lengths

Bonds	Exp.		Calc.	
	4	5	4	5
V(1)–O(1) _{phenolato}	1.929(2)	1.924(2)	1.911	1.908
V(1)–N(9) _{imine}	2.106(2)	2.130(2)	2.138	2.153
V(1)–N(18) _{py}	2.104(2)	2.116(2)	2.145	2.153
V(1)–O(21)	1.917(2)	2.158(2)	1.847	2.160
V(1)–O(28)	2.130(2)		2.149	
V(1)–N(28)		1.907(2)		1.883
V(1)–O(40) _{oxo}	1.623(2)	1.594(2)	1.589	1.587
C(8)–N(9)	1.310(2)	1.289(4)	1.308	1.308
O(21)–C(22)	1.318(2)	1.293(3)	1.330	1.289
C(23)–C(24)	1.388(2)	1.375(4)	1.393	1.383
C(25)–C(26)	1.381(2)	1.384(4)	1.389	1.395
C(22)–C(27)	1.435(2)	1.433(4)	1.433	1.442
C(27)–O(28)	1.292(2)		1.298	
C(27)–N(28)		1.359(4)		1.371

The features corroborate well to those of the *o*-benzosemiquinonate anion radicals coordinated to transition metal ions. Thus, the X-ray bond parameters support the existence of the electronic state B (Scheme 1) in **4**, which is defined as a $t\text{-Bu}^{\text{sq}}\text{V}^{\text{IV}}$ complex of oxidovanadium(IV).

5 crystallizes in the $P2_1/c$ space group and is iso-structural to **4** as depicted in Fig. 2(b). The V–O_{phenolato}, V–N_{py} and V–N_{imine} lengths are similar to those of **1** and **4** (see Table 2). The bond parameters of the redox non-innocent *p*-nitro-*o*-aminophenol ligand do not correlate to those of the dianionic *o*-amidophenolato state, rather the relatively shorter C–O, 1.293(3) Å and C–N, 1.359(4) Å lengths, and a quinoidal distortion of the phenyl ring correlates well to those of the *o*-iminobenzosemiquinone anion radicals coordinated to transition metal ions. Therefore, **5** is defined as a $\text{NO}^{\text{sq}}\text{V}^{\text{IV}}$ complex of oxidovanadium(IV).

6 crystallizes in the $C2/c$ space group. The molecular geometry in the crystals and the atom labeling scheme of **6** are depicted in Fig. 3. In **6**, two (L_{NNO})(VO) units are bridged by one sulfate and phenoxide functions, making two octahedral VO₄N₂ coordination spheres. The bond parameters of the two coordination spheres are summarized in Table 3. The average V=O lengths are 1.588(3) Å. The average V–O_{phenolato} and V–O_{imine} lengths are 1.965(2) and 2.076(2) Å, which are similar to those of **1**.

Redox activity

The redox activities of the complexes were investigated by cyclic voltammetry. The cyclic voltammograms of **1**–**6** are shown in Fig. 4, and the redox potential data referenced to the ferrocenium/ferrocene (Fc⁺/Fc) couple are summarized in Table 4. A significant observation is that both cathodic and anodic waves of **1** and **2**, as depicted in Fig. 4(a) and (b), are reversible. The anodic wave of **1**

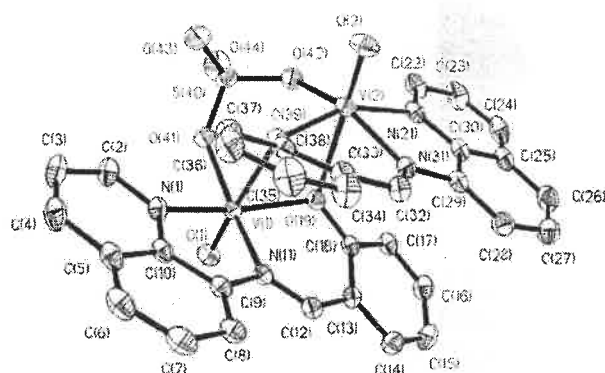


Fig. 3 Molecular geometry of $6 \cdot \frac{1}{2}\text{CH}_2\text{Cl}_2$ in crystals (40% thermal ellipsoid, CH_2Cl_2 and H atoms are omitted for clarity).

Table 3 Selected experimental bond lengths (Å) of $6 \cdot \frac{1}{2}\text{CH}_2\text{Cl}_2$

V(1)–O(1) _{oxo}	1.591(2)	V(2)–O(2)	1.586(3)
V(1)–N(1) _{py}	2.104(3)	V(2)–N(29)	2.100(3)
V(1)–N(11) _{imine}	2.072(2)	V(2)–N(31)	2.080(3)
V(1)–O(19) _{phenolato}	1.972(2)	V(2)–O(39)	1.956(2)
V(1)–O(41) _{sulfato}	1.963(2)	V(2)–O(42)	1.985(2)
V(1)–O(39)	2.436(2)	V(2)–O(19)	2.482(2)

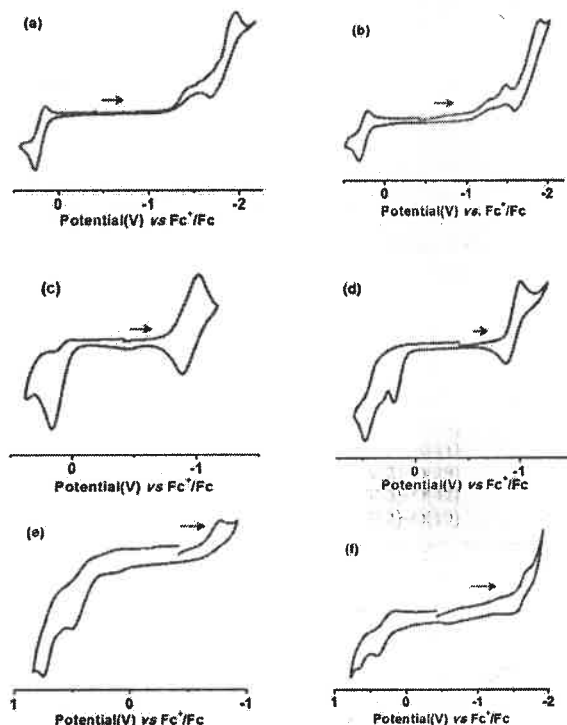


Fig. 4 Cyclic voltammograms of (a) **1**, (b) **2**, (c) **3**, (d) **4**, (e) **5**, (f) **6** in CH_2Cl_2 (0.20 M $[\text{N}(\text{n-Bu})_4]\text{PF}_6$) at 295 K. Potential data are referenced to Fc⁺/Fc couple (platinum working, platinum auxiliary and Ag/AgCl as reference electrodes).

and **2** at +0.20 and +0.26 V, respectively, are assigned to the V^{VO}/V^{VO} redox couple, while the cathodic waves at –1.82 and –1.75 V are assigned to (L[–])(VO)/(L^{2–})(VO) redox couples. Reversible formation of the aldimine anion radicals (L₁^{•2–} and L₂^{•2–})

Table 4 Redox potential data (referenced to Fc^+/Fc couple) of 1–6 determined by cyclic voltammetry in CH_2Cl_2

Complexes	E_1^1 (V) (ΔE^a , mV)	E_2^2 (V) (ΔE^a , mV)
1	+0.20 (110)	–1.82 (250)
2	+0.26 (105)	–1.75 (260)
3	+0.18 ^b	–0.95 (125)
4	+0.46 ^b , 0.20 ^b	–0.92 (120)
5	+0.50 ^b , +0.75 ^b	–0.77 ^c
6	+0.61 (100), +0.29 (250)	–1.66 ^c

^a Peak to peak separation in mV. ^b Anodic peak. ^c Cathodic peak.

coordinated to a transition metal ion is unprecedented. However, the cathodic wave is not quite reversible in the case of 6, which exhibits two consecutive anodic redox waves at +0.29 and +0.61 V due to $\text{VO}^{3+}/\text{VO}^{2+}$ redox couples, as shown in Fig. 4(f). The redox activities of 3–5 are different from those of 1 and 2. The cathodic waves of 3 and 4 due to $\text{sq}^{\bullet-}/\text{cat}^{2-}$ redox couple (Fig. 4(c) and (d)) are reversible, whereas the anodic waves due to $\text{VO}^{3+}/\text{VO}^{2+}$ redox couple are irreversible. Notably, the $\text{isq}^{\bullet-}/\text{ap}^{2-}$ redox couple of 5 is irreversible as shown in (Fig. 4(e)), but 5 displays two anodic peaks at +0.50 and +0.75 V due to $\text{isq}^{\bullet-}/\text{ap}^{2-}$ and $\text{VO}^{3+}/\text{VO}^{2+}$ redox couples. The features are similar to those for the *o*-iminobenzosemiquinonate anion radical complexes of oxidovanadium(IV) reported recently.¹²

X-band EPR spectroscopy

The X-band EPR spectra of 1 and 2 in CH_2Cl_2 were recorded. The spectra as shown in Fig. 5, are similar to those of the typical oxidovanadium complexes.^{12a,f} The simulated *g* values and the coupling parameters (*A*) corresponding to the oxidovanadium(IV) state are summarized in Table 5. It is recorded that 6 in CH_2Cl_2 exhibits an EPR signal as depicted in Fig. 5(d) due to the monomeric oxidovanadium(IV) ion. The EPR signal of 6 in CH_2Cl_2 predicts a partial conversion of the dimer to the EPR active monomeric unit. 3–5 are EPR silent, confirming the singlet ground states of these complexes, due to the anti-ferromagnetic coupling of the paramagnetic oxidovanadium(IV) ion with the $\text{sq}^{\bullet-}$, $^t\text{-Bu}^{\bullet}\text{sq}^{\bullet-}$ and $^{\text{NO}_2}\text{isq}^{\bullet-}$ radicals. The spectrum of the reduced

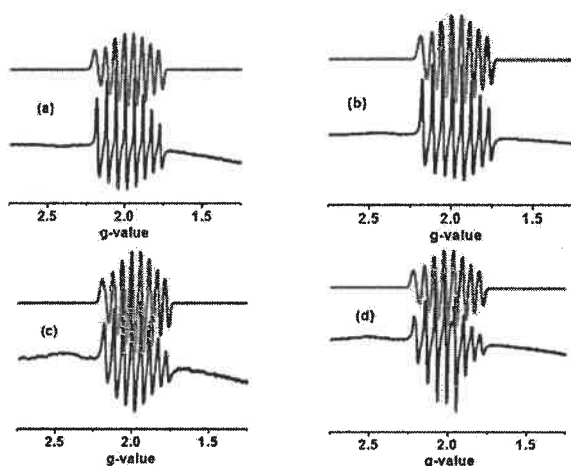


Fig. 5 X-Band EPR spectra of (a) 1, (b) 2, (c) 4[–] and (d) 6 in CH_2Cl_2 solution at 295 K (black, experimental; red, simulated).

Table 5 X-Band EPR spectral parameters of 1, 2, 4[–] and 6 in CH_2Cl_2 at 295 K

Complexes	<i>g</i>	<i>A</i> (G)	<i>Iw</i> (mT)
1	1.963	82.8 (51 V, <i>I</i> = 7/2)	3.8
2	1.964	83.2 (51 V, <i>I</i> = 7/2)	3.8
4 [–]	1.962	82.8 (51 V, <i>I</i> = 7/2)	3.2
6	1.972	84.5 (51 V, <i>I</i> = 7/2)	3.5

anion, 4[–], is similar to that of 1 and 2 inferring that 4[–] is an oxidovanadium(IV) complex of catecholato(2[–]) ion.¹²

⁵¹V and CP/MAS ⁵¹V NMR spectroscopy

The fluid solution ⁵¹V NMR spectra of diamagnetic 3–5 were recorded in CDCl_3 and are shown in Fig. S1 (ESI†). The solid state CP/MAS ⁵¹V NMR spectra of these complexes were also recorded using 6–12 kHz frequencies and are depicted in Fig. 6. The solution and CP/MAS spectral data (obtained using 10 kHz frequency) are summarized in Table 6. It is observed that in both cases the ⁵¹V NMR signals of 3, 4 and 5 are deshielded significantly, particularly in the solid state the chemical shift spans a range of –100.3 to +608.7 ppm with respect to the isotropic peak of V_2O_5 at –612 ppm. The larger de-shielding of the ⁵¹V nuclei of 3–5 in both solid and solution state compare well to those of the coupled dinuclear oxidovanadium(IV) complexes, e.g. ⁵¹V NMR signals of $[\text{V}_2(\text{cp})_2(\mu^2\text{-N-Tol})_2(\text{Me})_2]$ and $[\text{V}_2(\mu^2\text{-N-Bu})_2(\text{O-Bu})_2(\text{CH}_2\text{-Bu})_2]$ appear at +674 and +967 ppm.²⁸ The spectral parameters correlate well to those of the oxidovanadium(IV)

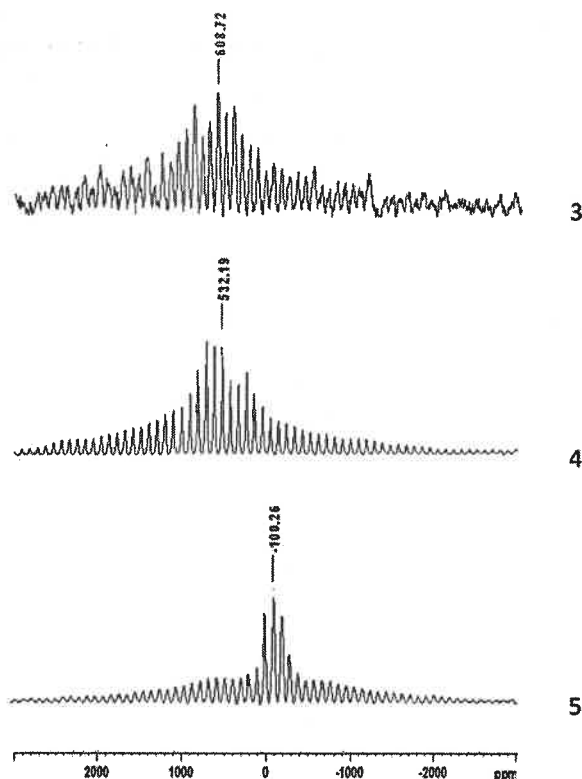


Fig. 6 CP/MAS ⁵¹V NMR spectra of 3–5 (using 10 kHz frequency).

Table 6 Experimental isotropic chemical shifts of ^{51}V nuclei of 3–5

Complexes	CP/MAS ^a	CDCl_3^b
3	+608.7	+380.6
4	+530.9	+525.3
5	−100.3	0.0

^a Chemical shifts of the solid were referred to isotropic peak of V_2O_5 at −612 ppm. ^b Chemical shifts of the solutions were referred to aqueous solution of ammonium metavanadate at −574.3 ppm.

complexes incorporating semiquinonate anion radicals as reported recently,¹² and infer the coordination of $\text{sq}^{\bullet-}$, $^t\text{Bu}\text{sq}^{\bullet-}$ and $\text{NO}_2\text{sq}^{\bullet-}$ radicals to oxidovanadium(IV) in 3, 4 and 5.

Density functional theory (DFT) calculations

The electronic structures of the diamagnetic 1^- and 2^- were elucidated by DFT calculations. Gas phase geometries of 1^- and 2^- were optimized with the singlet and triplet spin states, while that of 1 and 2 were optimized with the doublet spin state. The closed shell singlet (CSS) solutions of both 1^- and 2^- ions are unstable due to open shell singlet (OSS) perturbation. The OSS solutions of 1^- and 2^- with 100% di-radical character are 18.1 and 18.2 kcal mol^{−1}, respectively, and are more stable than the corresponding CSS solutions. Notably, the triplet solutions of 1^- and 2^- are 22.4 and 20.50 kcal mol^{−1} lower than the singlet states. The OSS solutions with optimized bond parameters of the ions are summarized in Table 1. It is recoded that the C=N lengths are relatively longer in the 1^- and 2^- ions. The calculated C=N lengths are 1.309 Å for 1 and 1.303 Å for 2, while those of 1^- and 2^- ions are 1.324 and 1.329 Å, respectively. Analyses of the Mulliken spin show that the beta spin disperses mainly on the tri-dented NNO-ligand, particularly on the aldimine function (1^- , 35% and 2^- , 39%), while the α spin is localized on the vanadium as depicted in Fig. 7. This feature correlates with the reduction of the L_1^{1-} and L_2^{1-} to $\text{L}_1^{\bullet 2-}$ and $\text{L}_2^{\bullet 2-}$ in 1^- and 2^- ion. Thus, 1^- and 2^- are defined as aldimine anion radical complexes of oxidovanadium(IV).

Electronic spectra

The UV-vis/NIR absorption spectra of 1–6 complexes were recorded in CH_2Cl_2 at 295 K and the spectra are illustrated in Fig. 8. The spectral data are summarized in Table 7. The spectra of 1, 2 and 6 display stronger absorption bands at 435, 475 and 420 nm due to $d_v \rightarrow \pi_{\text{imine}}^*$ transitions. Electronic spectra of 4 and 5 that display lower energy absorption bands above 600 nm are different from those of 1, 2 and 6. However, the electronic spectra of 4 and 5 corroborate well to those of *o*-benzosemiquinonate and *o*-iminobenzosemiquinonate anion radical complexes of the oxidovanadium(IV) ion.¹² The λ_{max} of 4 at 850 nm is assigned to dioxolene \rightarrow vanadium charge transfer (LMCT). TD DFT calculation on the singlet state of 4 was performed to elucidate the excitation energies in CH_2Cl_2 . The λ_{cal} , 711.5 nm ($f = 0.08$) is due to LMCT and ILCT transitions. Similarly the λ_{cal} of 5 is 562.3 nm ($f = 0.11$) because of the LMCT and ILCT transitions. The LMCT transitions of 4 and 5 are defined as CSS \rightarrow OSS perturbation transitions, where the CSS solution is unstable.

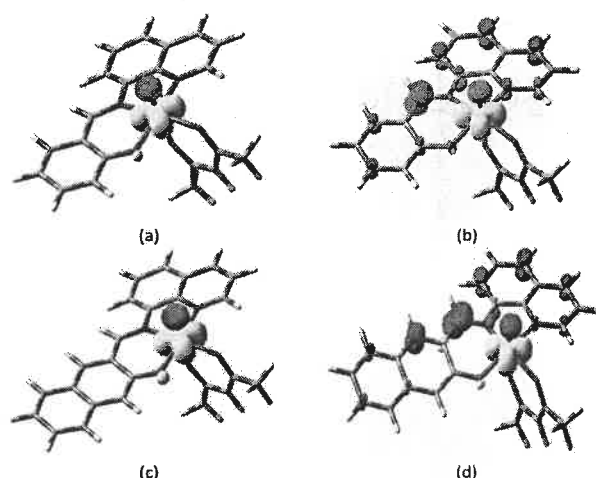


Fig. 7 Atomic spin of (a) 1 (V, 1.18; O30, −0.15) and (b) 1^- (V, 1.18; C8, −0.35; C11, −0.17; C13, −0.20; C15, −0.18; O30, −0.14) (c) 2 (V, 1.18; O30, −0.15) and (d) 2^- (V, 1.16; C6, −0.18; C8, −0.39; C11, −0.16; C13, −0.17; C15, −0.12; O30, −0.14) obtained from DFT calculations (yellow, alpha spin and red, beta spin).

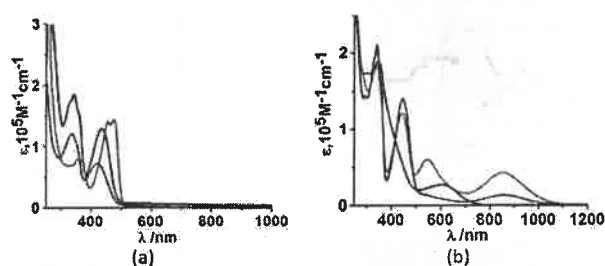


Fig. 8 UV-vis-NIR absorption spectra of (a) 1 (blue), 2 (green), 6 (violet) and (b) 3 (blue), 4 (red) and 5 (black) in CH_2Cl_2 at 295 K.

Table 7 Electronic spectral data of 1–6, 1^- , 2^- and 4^- in CH_2Cl_2 at 295 K

Comp.	λ_{max} , nm (ϵ , $10^5 \text{ M}^{-1} \text{ cm}^{-1}$)
1	435 (1.30), 360 (1.52), 345 (1.85), 330 (1.73)
2	475 (1.44), 455 (1.41), 360 (0.80), 330 (0.70)
3	865 (0.14), 540 (0.14), 445 (1.40), 340 (2.10), 355 (1.60)
4	850 (0.43), 535 (0.60), 440 (1.22), 355 (1.42), 340 (1.75)
5	605 (0.28), 410 (0.95)sh, 345 (1.89), 300 (1.75)
6	420 (0.73), 350 (1.02), 335 (1.22)
1^-	435 (0.90), 355 (1.59), 345 (1.90), 330 (1.76)
2^-	475 (1.18), 455 (1.20), 425 (0.84), 360 (0.70), 325 (0.73)
4^-	850 (0.15), 530 (0.23), 435 (0.45), 385 (0.63), 345 (1.45)

The change in the electronic spectra during $1 \rightarrow 1^-$, $2 \rightarrow 2^-$, $4 \rightarrow 4^-$ and $5 \rightarrow 5^-$ conversions was recorded by spectro-electrochemical measurements in CH_2Cl_2 at 295 K, and the results are shown in Fig. 9. In 1^- and 2^- ions the π_{imine}^* is partly occupied, and the intensity of the LMCT ($d_v \rightarrow \pi_{\text{imine}}^*$) transition decreases in the reduced anions, predicting a ligand based reduction. Similarly, as the 4^- and 5^- ions contain oxidovanadium(IV) ions, the intensity of the LMCT transitions decreases during $4 \rightarrow 4^-$ and $5 \rightarrow 5^-$ transformations, indicating ligand based oxidations.

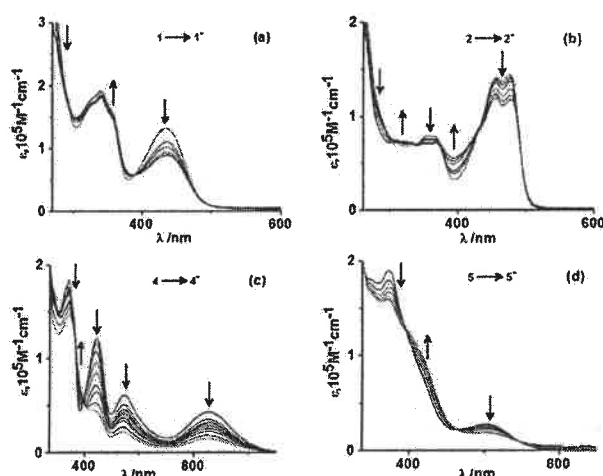


Fig. 9 Change of UV-vis/NIR absorption spectra during the conversions of (a) $1 \rightarrow 1^-$, (b) $2 \rightarrow 2^-$, (c) $4 \rightarrow 4^-$ and (d) $5 \rightarrow 5^-$ were recorded by spectroelectrochemical measurements in CH_2Cl_2 at 295 K.

Conclusion

Stabilization of an organic radical with transition metal ions has been a challenge in chemical research. This study reveals that the paramagnetic oxidovanadium(IV) ion can stabilize organic radicals coupling anti-ferromagnetically. It was disclosed that, the NNO donor aldimine ligands, (*E*)-2-((quinolin-8-ylimino)methyl)phenol (L_1H) and (*E*)-1-((quinolin-8-ylimino)methyl)naphthalen-2-ol (L_2H) are redox non-innocent towards the oxidovanadium(IV) ion. The coordination of the hitherto unknown aldimine anion radicals ($\text{L}_1^{\bullet 2-}$ and $\text{L}_2^{\bullet 2-}$) to oxidovanadium(IV) was detected. In addition, *o*-benzosemiquinonate ($\text{sq}^{\bullet -}$), 3,5-di-*tert*-butyl-*o*-benzosemiquinonate ($^t\text{Bu}_{35}\text{sq}^{\bullet -}$) and *p*-nitro-*o*-imino-benzosemiquinonate ($^{\text{NO}_2}\text{isq}^{\bullet -}$) anion radical complexes of oxidovanadium(IV) and their redox features substantiated by single crystal X-ray crystallography on representative complexes, the solid state CP/MAS ^{51}V NMR and EPR spectroscopy, cyclic voltammetry and DFT calculations are reported.

Acknowledgements

Financial support received from Department of Science and Technology (EMR/2016/005222) and University Grants Commission (F. No. 43-214/2014(SR)) New Delhi, India is gratefully acknowledged. S. B. acknowledges (08/531(0006)/2012-EMR-I) CSIR, New Delhi, India, for fellowships. We are gratefully to Dr P. R. Rajamohan and Central NMR Facility, National Chemical Laboratory, Pune, India for ^{51}V NMR spectroscopy.

Notes and references

- (a) J. W. Whittaker, *Arch. Biochem. Biophys.*, 2005, **433**, 227–239; (b) F. Himo and P. E. M. Siegbahn, *Chem. Rev.*, 2003, **103**, 2421–2456; (c) J. Stubbe and W. A. van der Donk, *Chem. Rev.*, 1998, **98**, 705–762; (d) K. E. Silva, T. E. Elgren, L. Que Jr. and M. T. Stankovich, *Biochemistry*, 1995, **34**, 14093–14103.
- (a) D. L. J. Broere, L. L. Metz, B. de Bruin, J. N. H. Reek, M. A. Siegler and J. I. Vlucht, *Angew. Chem., Int. Ed.*, 2015, **54**, 1516–1520; (b) D. L. J. Broere, R. Plessius and J. I. Vlucht, *Chem. Soc. Rev.*, 2015, **44**, 6886–6915; (c) O. R. Luca and R. H. Crabtree, *Chem. Soc. Rev.*, 2013, **42**, 1440–1459; (d) V. Lyaskovskyy and B. de Bruin, *ACS Catal.*, 2012, **02**, 270–279.
- (a) C. G. Pierpont, *Coord. Chem. Rev.*, 2001, **219–221**, 415–433; (b) C. G. Pierpont, *Coord. Chem. Rev.*, 2001, **216–217**, 99–125; (c) C. Drouza and A. D. Keramidas, *Inorg. Chem.*, 2008, **47**, 7211–7224.
- (a) C. T. Lyons and T. D. P. Stack, *Coord. Chem. Rev.*, 2013, **257**, 528–540; (b) P. Chaudhuri and K. Wieghardt, *Prog. Inorg. Chem.*, 2001, **50**, 151; (c) Y. Wang, J. L. DuBois, B. Hedman, K. O. Hodgson and T. D. P. Stack, *Science*, 1998, **279**, 537–540; (d) A. Sokolowski, J. Müller, T. Weyhermüller, R. Schnepf, P. Hildebrandt, K. Hildenbrand, E. Bothe and K. Wieghardt, *J. Am. Chem. Soc.*, 1997, **119**, 8889–8900.
- S. Kimura, E. Bill, E. Bothe, T. Weyhermüller and K. Wieghardt, *J. Am. Chem. Soc.*, 2001, **123**, 6025–6039.
- (a) A. Kochem, G. Gellon, N. Leconte, B. Baptiste, C. Philouze, O. Jarjays, M. Orio and F. Thomas, *Chem. – Eur. J.*, 2013, **19**, 16707–16721; (b) C.-C. Tsou, F.-T. Tsai, H.-Y. Chen, I.-J. Hsu and W.-F. Liaw, *Inorg. Chem.*, 2013, **52**, 1631–1639; (c) Y. Miyazato, T. Wada, J. T. Muckerman, E. Fujita and K. Tanaka, *Angew. Chem., Int. Ed.*, 2007, **46**, 5728–5730; (d) T. Buttner, J. Geier, G. Frison, J. Harmer, C. Calle, A. Schweiger, H. Schonberg and H. Grutzmacher, *Science*, 2005, **307**, 235–238; (e) F. N. Penkert, T. Weyhermüller, E. Bill, P. Hildebrandt, S. Lecomte and K. Wieghardt, *J. Am. Chem. Soc.*, 2000, **122**, 9663–9673.
- (a) S. Maity, S. Kundu, T. Weyhermüller and P. Ghosh, *Inorg. Chem.*, 2015, **54**, 1300–1313; (b) K. Pramanik, M. Shivakumar, P. Ghosh and A. Chakravorty, *Inorg. Chem.*, 2000, **39**, 195–199; (c) M. Shivakumar, K. Pramanik, P. Ghosh and A. Chakravorty, *Inorg. Chem.*, 1998, **37**, 5968–5969.
- (a) G. Skara, B. Pinter, P. Geerlings and F. De Proft, *Chem. Sci.*, 2015, **6**, 4109–4117; (b) C. Wolff, A. Gottschlich, J. England, K. Wieghardt, W. Saak, D. Haase and R. Beckhaus, *Inorg. Chem.*, 2015, **54**, 4811–4820; (c) S. C. Patra, T. Weyhermüller and P. Ghosh, *Inorg. Chem.*, 2014, **53**, 2427–2440; (d) K. Chłopek, E. Bill, T. Weyhermüller and K. Wieghardt, *Inorg. Chem.*, 2005, **44**, 7087–7098.
- (a) S. C. Bart, K. Chłopek, E. Bill, M. W. Bouwkamp, E. Lobkovsky, F. Neese, K. Wieghardt and P. J. Chirik, *J. Am. Chem. Soc.*, 2006, **128**, 13901–13912; (b) A. C. Bowman, C. Milsman, C. C. H. Atienza, E. Lobkovsky, K. Wieghardt and P. J. Chirik, *J. Am. Chem. Soc.*, 2010, **132**, 1676–1684.
- (a) T. A. Alsalam, J. S. Hadi, E. A. Al-Nasir, H. S. Abbo and S. J. J. Titinchi, *Catal. Lett.*, 2010, **136**, 228–233; (b) S. Mohebbi, F. Nikpour and S. Raiati, *J. Mol. Catal. A: Chem.*, 2006, **256**, 265–268; (c) N. S. Venkataramanan, G. Kuppuraj and S. Rajagopal, *Coord. Chem. Rev.*, 2005, **249**, 1249–1268.
- (a) J. C. Pessoa, S. Etcheverry and D. Gambino, *Coord. Chem. Rev.*, 2015, **301–302**, 24–48; (b) D. Rehder, *Future Med. Chem.*, 2012, **4**, 1823–1837; (c) D. C. Crans and T. J. Meade, *Inorg. Chem.*, 2013, **52**, 12181–12183; (d) D. C. Crans, K. A. Woll, K. Prusinskas, M. D. Johnson and E. Norkus, *Inorg. Chem.*,

- 2013, 52, 12262–12275; (e) C. C. McLauchlan and D. C. Crans, *Dalton Trans.*, 2013, 42, 11744–11748; (f) C. J. Schneider, G. Zampella, L. DeGioia and V. L. Pecoraro, ACS Symposium Series, in *Vanadium: The Versatile Metal*, ed. K. Kustin, J. C. Pessoa and D. C. Crans, American Chemical Society, Washington, DC, 2009, ch. 12, vol. 974, pp. 148–162.
- 12 (a) M. Shit, S. Maity, S. Bera, T. Weyhermüller and P. Ghosh, *New J. Chem.*, 2016, 40, 10305–10315; (b) M. Stylianou, C. Drouza, J. Giapintzakis, G. I. Athanasopoulos and A. D. Keramidas, *Inorg. Chem.*, 2015, 54, 7218–7229; (c) S. Ghorai and C. Mukherjee, *Chem. Commun.*, 2012, 48, 10180–10182; (d) A. Saha Roy, P. Saha, N. Das Adhikary and P. Ghosh, *Inorg. Chem.*, 2011, 50, 2488–2500; (e) M. Shit, S. Bera, S. Maity, S. Maji, T. Weyhermüller and P. Ghosh, *Eur. J. Inorg. Chem.*, 2016, 330–338; (f) S. Kundu, S. Maity, T. Weyhermüller and P. Ghosh, *Inorg. Chem.*, 2013, 52, 7417–7430; (g) S. Kundu, S. Maity, A. N. Maity, S.-C. Ke and P. Ghosh, *Dalton Trans.*, 2013, 42, 4586–4601.
- 13 (a) M. Marloye, G. Berger, M. Gelbcke and F. Dufrasne, *Future Med. Chem.*, 2016, 8, 2263–2286; (b) E. Kioseoglou, S. Petanidis, C. Gabriel and A. Salifoglou, *Coord. Chem. Rev.*, 2015, 301–302, 87–105; (c) V. G. Sankareswari, D. Vinod, A. Mahalakshmi, M. Alamelu, G. Kumaresan, R. Ramaraj and S. Rajagopal, *Dalton Trans.*, 2014, 43, 3260–3272; (d) M. Mohamadi, S. Y. Ebrahimipour, M. Torkzadeh-Mahani, S. Foro and A. Akbari, *RSC Adv.*, 2015, 5, 101063; (e) S. Banerjee, A. Dixit, R. N. Shridharan, A. A. Karande and A. R. Chakravarty, *Chem. Commun.*, 2014, 50, 5590–5592.
- 14 (a) T. Koleča-Dobráv, K. Maejima, Y. Yoshikawa, A. Meden, H. Yasui and F. Perdi, *New J. Chem.*, 2017, 41, 735–746; (b) Y. Yoshikawa, H. Sakurai, D. C. Crans, G. Micera and E. Garribba, *Dalton Trans.*, 2014, 43, 6965–6972; (c) D. Sanna, G. Micera and E. Garribba, *Inorg. Chem.*, 2013, 52, 11975–11985; (d) H. Sakurai, S. Funakoshi and Y. Adachi, *Pure Appl. Chem.*, 2005, 77, 1629; (e) Y. Shechter, I. Goldwasser, M. Mironchik, M. Fridkin and D. Gefel, *Coord. Chem. Rev.*, 2003, 237, 3; (f) K. H. Thompson, J. H. McNeill and C. Orvig, *Chem. Rev.*, 1999, 99, 2561.
- 15 (a) J. Wagler, D. Gerlach and G. Roewer, *Inorg. Chim. Acta*, 2007, 360, 1935–1942; (b) P. Fita, E. Luzina, T. Dziembowska, D. Kopeć, P. Piątkowski, Cz. Radzewicz and A. Grabowska, *Chem. Phys. Lett.*, 2005, 416, 305; (c) R. A. Rowe and M. M. Jones, *Inorg. Synth.*, 1957, 5, 113–115.
- 16 (a) S. Stoll, *Int. EPR Soc. Newsletter*, 2003, 13, 24; (b) S. Stoll and A. Schweiger, *J. Magn. Reson.*, 2006, 178, 42.
- 17 (a) G. M. Sheldrick, *ShelXS97*, Universität Göttingen, Göttingen, Germany, 1997; (b) G. M. Sheldrick, *ShelXL97*, Universität Göttingen, Göttingen, Germany, 1997; (c) G. M. Sheldrick, *XS. Version 2013/1*, Georg-August-Universität Göttingen, Göttingen, Germany, 2013; (d) G. M. Sheldrick, *Acta Crystallogr., Sect. A: Found. Adv.*, 2015, 71, 3–8; (e) G. M. Sheldrick, *Acta Crystallogr., Sect. C: Struct. Chem.*, 2015, 71, 3–8.
- 18 M. J. Frisch, G. W. Trucks, H. B. Schlegel, G. E. Scuseria, M. A. Robb, J. R. Cheeseman Jr., J. A. Montgomery, T. Vreven, K. N. Kudin, J. C. Burant, J. M. Millam, S. S. Iyengar, J. Tomasi, V. Barone, B. Mennucci, M. Cossi, G. Scalmani, N. Rega, G. A. Petersson, H. Nakatsuji, M. Hada, M. Ehara, K. Toyota, R. Fukuda, J. Hasegawa, M. Ishida, T. Nakajima, Y. Honda, O. Kitao, H. Nakai, M. Klene, X. Li, J. E. Knox, H. P. Hratchian, J. B. Cross, V. Bakken, C. Adamo, J. Jaramillo, R. Gomperts, R. E. Stratmann, O. Yazyev, J. A. Austin, R. Cammi, C. Pomelli, J. W. Ochterski, P. Y. Ayala, K. Morokuma, G. A. Voth, P. Salvador, J. J. Dannenberg, V. G. Zakrzewski, S. Dapprich, A. D. Daniels, M. C. Strain, O. Farkas, D. K. Malick, A. D. Rabuck, K. Raghavachari, J. B. Foresman, J. V. Ortiz, Q. Cui, A. G. Baboul, S. Clifford, J. Cioslowski, B. B. Stefanov, G. Liu, A. Liashenko, P. Piskorz, I. Komaromi, R. L. Martin, D. J. Fox, T. Keith, M. A. Al-Laham, C. Y. Peng, A. Nanayakkara, M. Challacombe, P. M. W. Gill, B. Johnson, W. Chen, M. W. Wong, C. Gonzalez and J. A. Pople, *Gaussian 03 (Revision E.01)*, Gaussian, Inc., Wallingford, CT, 2004.
- 19 (a) R. G. Parr and W. Yang, *Density Functional Theory of Atoms and Molecules*, Oxford University Press, Oxford, UK, 1989; (b) D. R. Salahub and M. C. Zerner, *The Challenge of d and f Electrons*, ACS Symposium Series 394, American Chemical Society, Washington, DC, 1989; (c) W. Kohn and L. J. Sham, *Phys. Rev.*, 1965, 140, A1133–A1138; (d) P. Hohenberg and W. Kohn, *Phys. Rev.*, 1964, 136, B864–B871.
- 20 (a) R. E. Stratmann, G. E. Scuseria and M. Frisch, *J. Chem. Phys.*, 1998, 109, 8218–8224; (b) M. E. Casida, C. Jamoroski, K. C. Casida and D. R. Salahub, *J. Chem. Phys.*, 1998, 108, 4439–4449; (c) R. Bauernschmitt, M. Haser, O. Treutler and R. Ahlrichs, *Chem. Phys. Lett.*, 1996, 256, 454–464.
- 21 (a) A. D. Becke, *J. Chem. Phys.*, 1993, 98, 5648–5652; (b) B. Miehlich, A. Savin, H. Stoll and H. Preuss, *Chem. Phys. Lett.*, 1989, 157, 200–205; (c) C. Lee, W. Yang and R. G. Parr, *Phys. Rev. B: Condens. Matter Mater. Phys.*, 1988, 37, 785–789.
- 22 P. Pulay, *J. Comput. Chem.*, 1982, 3, 556.
- 23 H. B. Schlegel and J. J. McDouall, in *Computational Advances in Organic Chemistry*, ed. C. Ogretir and I. G. Csizmadia, Kluwer Academic, The Netherlands, 1991, pp. 167–185.
- 24 (a) P. J. Hay and W. R. Wadt, *J. Chem. Phys.*, 1985, 82, 270–283; (b) W. R. Wadt and P. J. Hay, *J. Chem. Phys.*, 1985, 82, 284–298; (c) P. J. Hay and W. R. Wadt, *J. Chem. Phys.*, 1985, 82, 299–310.
- 25 W. J. Hehre, R. Ditchfield and J. A. Pople, *J. Chem. Phys.*, 1972, 56, 2257–2261.
- 26 (a) V. A. Rassolov, M. A. Ratner, J. A. Pople, P. C. Redfern and L. A. Curtiss, *J. Comput. Chem.*, 2001, 22, 976–984; (b) M. M. Francl, W. J. Pietro, W. J. Hehre, J. S. Binkley, D. J. DeFrees, J. A. Pople and M. S. Gordon, *J. Chem. Phys.*, 1982, 77, 3654–3665; (c) P. C. Hariharan and J. A. Pople, *Mol. Phys.*, 1974, 27, 209–214; (d) P. C. Hariharan and J. A. Pople, *Theor. Chim. Acta*, 1973, 28, 213–222; (e) W. J. Hehre, R. Ditchfield and J. A. Pople, *J. Chem. Phys.*, 1972, 56, 2257–2261.
- 27 (a) B. Baruah, S. Das and A. Chakravorty, *Inorg. Chem.*, 2002, 41, 4502–4508; (b) S. P. Rath, K. K. Rajak and A. Chakravorty, *Inorg. Chem.*, 1999, 38, 4376–4377.
- 28 (a) P. B. Chatterjee, O. G. Zapata, L. L. Quinn, G. Hou, H. Hamaed, R. W. Schurko, T. Polenova and D. C. Crans, *Inorg. Chem.*, 2011, 50, 9794–9803; (b) D. Rehder, *Coord. Chem. Rev.*, 2008, 252, 2209–2223.



Ramakrishna Mission Residential College (Autonomous)
Kolkata 700103, WB, India

Collaborative research in coordination chemistry of organic radicals
Number 13

Institute 1: Ramakrishna Mission Residential College (Autonomous)

Concerned Faculty: Dr. Prasanta Ghosh, Dept of Chemistry

&

Institute 2: Max-Planck-Institut für Chemische Energiekonversion

Stiftstrasse 34 - 36 / D - 45470 Mülheim an der Ruhr

Concerned Scientist: Dr Thomas Weyhermüller

Period of Investigation: 03-03-2018 to 31-08-2018

**Project: Proton-Coupled Redox Reactions and Aminyl Radical Complexes
of Transition Metal Ions**

Output: The result was published in a journal of international repute

**Publication: Proton-Coupled Oxidation of a Diarylamine: Amido and
Aminyl Radical Complexes of Ruthenium(II)**

Suman Kundu, Debarpan Dutta, Suwendu Maity, Thomas Weyhermüller and
Prasanta Ghosh*

Inorg. Chem. **2018**, 57, 19, 11948-11960

Dr. Prasanta Ghosh

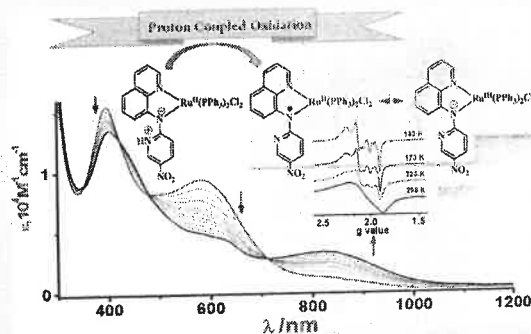
Dr Thomas Weyhermüller

Proton-Coupled Oxidation of a Diarylamine: Amido and Aminyl Radical Complexes of Ruthenium(II)

Suman Kundu,[†] Debarpan Dutta,[†] Suvendu Maity,[†] Thomas Weyhermüller,[‡] and Prasanta Ghosh^{*,†}[†]Department of Chemistry, R. K. Mission Residential College, Narendrapur, Kolkata 700103, India[‡]Max-Planck-Institut für Chemische Energiekonversion, Stiftstrasse 34-36, 45470 Mülheim an der Ruhr, Germany

Supporting Information

ABSTRACT: Diarylamido, Q-N[−]-Py (L[−]), complexes of ruthenium(II), *trans*-[(L[−]H⁺)Ru^{II}(PPh₃)₂Cl₂] (1[−]H⁺) and *trans*-[(L[−])Ru^{II}(PPh₃)₂(CO)Cl] (2), using *N*-(5-nitropyridin-2-yl)-quinolin-8-amine (HL) as a ligand are disclosed (Q and Py refer to quinoline and 5-nitropyridine fragments). 1[−]H⁺ contains a zwitterionic amido ligand (Q-N[−]-PyH⁺) that undergoes a concerted proton electron transfer (CPET) reaction in air, generating *trans*-[(L)Ru(PPh₃)₂Cl₂] (1·CH₂Cl₂). The ground electronic state of 1 is delocalized as [(L[−])Ru^{III} ↔ (L[•])Ru^{II}] (L[•] is an aminyl radical of type Q-N[•]-Py). The 1[−]H⁺/1 redox potential depends on the electrolytes, and the potentials are −1.57 and −1.40 V, respectively, in the presence of [N(*n*-Bu)₄]PF₆ and [N(*n*-Bu)₄]Cl. The rate of 1[−]H⁺ → 1 conversion depends also on the medium and follows the



order $k_{D_2O-CH_2Cl_2} > k_{H_2O-CH_2Cl_2} > k_{CH_2Cl_2}$. In contrast, 2 containing the corresponding amido (L[−]) is stable and endures oxidation at 0.14 V, affording *trans*-[(L[•])Ru^{II}(PPh₃)₂(CO)Cl] (2[•]). The electronic structures of the complexes were authenticated by single-crystal X-ray diffraction studies of HL, 1·CH₂Cl₂, and 2·(toluene), EPR spectroscopy, and density functional theory (DFT) calculations. Notably, the C_Q–N (1.401(2) Å) and C_{Py}–N (1.394(2) Å) lengths in 1·CH₂Cl₂ are relatively longer than the C_Q–N_{amido} (1.396(4) Å) and C_{Py}–N_{amido} (1.372(4) Å) lengths in 2·(toluene). Spin density obtained from DFT calculations scatters on both N and ruthenium atoms, revealing a delocalized state of 1. The notion was further confirmed by variable-temperature EPR spectra of a powder sample and CH₂Cl₂ solution, where the contributions of both [(L[−])Ru^{III}] and [(L[•])Ru^{II}] components were detected. In contrast, 2[•] is an aminyl radical complex of ruthenium(II), where the spin is dominantly localized on the ligand backbone (64%), particularly on N (27%). 2[•] exhibits a strong EPR signal at *g* = 2.003. 1 and 2[•] exhibit absorption bands at 560–630 and 830–840 nm, and the origins of these excitations were elucidated by TDDFT calculations on 1 and 2 in CH₂Cl₂.

INTRODUCTION

Stabilization of aminyl radical (R₁R₂N[•]) to disclose the parallel chemistry to the phenoxyl (PhO[•]) and alkyl (R₃C[•]) radicals which perform several essential biological reactions is a challenge in the coordination chemistry of organic radicals.^{1–5} The R₁R₂N[•] radical is relatively more reactive and hard to stabilize in a free form or upon coordination to a transition-metal ion. In this vast coordination chemistry, only a few aminyl and anilino radical complexes have been isolated and substantiated by single-crystal X-ray crystallography.⁶ The paucity of isolated aminyl radical complexes is the primary obstacle for the growth of the chemistry of this reactive species. Thus, isolation of amine/amido (R₁R₂N[−]) complexes that undergo oxidation to R₁R₂N[•] is rewarding.

Proton-coupled electron transfer (PCET) reactions are significant in analyzing several spontaneous redox reactions occurring in nature.⁷ The term PCET was introduced in 1981 to define a redox reaction where an electron and a proton transfer together, but currently PCET is a wide terminology that covers redox reaction involving transfer of protons and

electrons. The notable PCET reactions are reductions of CO₂ to carbohydrate, O₂ to H₂O, N₂ to NH₃, CO₂ to CH₄, etc. The thermochemistry of these reactions is not simple;⁸ however, it is worth exploring a simple chemical system undergoing concerted or sequential proton and electron transfer reactions and compare with those where no proton transfer occurs and the effect of this on the products. Redox reactions where the e[−]/H⁺ donor orbitals and e[−]/H⁺ acceptor orbitals validate a simultaneous transfer of proton and electron are defined by concerted proton–electron transfer (CPET), electron transfer proton transfer (ETPT), and concerted electron–proton transfer (CEP).^{7b} In this presentation the term CPET has been used for such a reaction and it is different from the sequential proton and electron transfer (PET) reactions. In this study, a proton-coupled oxidation of a diarylamido group coordinated to a transition-metal ion following a CPET path that affords an aminyl radical complex is disclosed. The

Received: May 22, 2018

Published: September 13, 2018



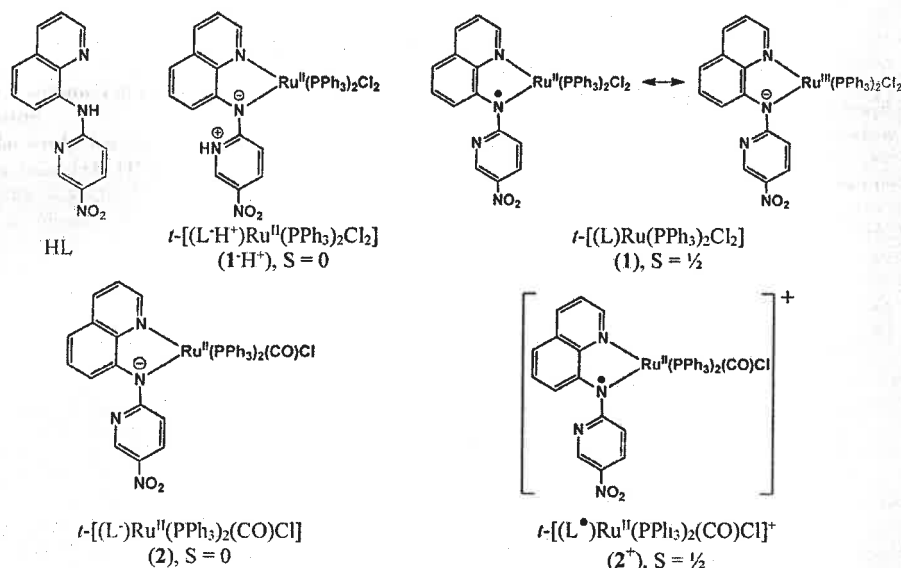
ACS Publications

© 2018 American Chemical Society

11948

DOI: 10.1021/acs.inorgchem.8b01401
Inorg. Chem. 2018, 57, 11948–11960

Chart 1. Reported Diarylamine, Amido, and Aminyl Radical Complexes of Ruthenium(II)



reaction parallels the proton-coupled oxidation of tyrosine to a tyrosine radical.⁹ The oxidation of an amine to an aminyl radical in air is not common in chemical science. In this regard this report is worthy.

In this particular work, diarylamido complexes of ruthenium(II) of the types $trans-[(L-H^+)Ru^{II}(PPh_3)_2Cl_2]$ ($1-H^+$) and $trans-[(L)Ru^{II}(PPh_3)_2(CO)Cl]$ (2), where L^- contains a Q-N-Py fragment as illustrated in Chart 1, were successfully isolated. Q and Py refer to quinoline and 5-nitropyridine fragments of the amine *N*-(5-nitropyridin-2-yl)quinolin-8-amine (HL) used in this study. $1-H^+$ is a zwitterionic diarylamido ($L-H^+$) complex and is not stable in solution. In air, it undergoes a proton-coupled oxidation reaction, generating the paramagnetic complex $trans-[(L)Ru^{II}(PPh_3)_2Cl_2]$ (1 ; CH_2Cl_2), which is delocalized and is a hybrid of two extreme resonance forms, $[(L^-)Ru^{III}] \leftrightarrow [(L^\bullet)Ru^{II}]$. In contrast, 2 is stable in air. However, coulometric oxidation of 2 at 0.14 V versus the Fc^+/Fc couple generates an aminyl radical (L^\bullet) complex of ruthenium(II). The molecular and electronic structures of $1-H^+$, 1 , 2 , and 2^+ were established by single-crystal X-ray crystallography, EPR spectroscopy, and DFT calculations.

EXPERIMENTAL SECTION

Materials and Physical Measurements. Reagents or analytical grade materials were obtained from Sigma-Aldrich and used without further purification. Spectroscopic grade solvents were used for spectroscopic and electrochemical measurements. The C, H, and N contents of the compounds were obtained from a PerkinElmer 2400 Series II elemental analyzer. Infrared spectra of the samples were measured from 4000 to 400 cm^{-1} with KBr pellets at room temperature on a PerkinElmer Spectrum RX 1 FT-IR spectrophotometer. 1H NMR spectra were obtained at 295 K on a Bruker DPX 300 MHz spectrometer. ESI mass spectra were recorded on a micro mass Q-TOF mass spectrometer. Electronic absorption spectra were recorded on a PerkinElmer Lambda 750 spectrophotometer in the range 3300–175 nm. Magnetic susceptibilities at 298 K were measured on a Sherwood Magnetic Susceptibility Balance. The X-band EPR spectra were measured on a Magnetech GmbH MiniScope MS400 spectrometer (equipped with a TC H03 temperature controller), where the microwave frequency was measured with an

FC400 frequency counter. The EPR spectra were simulated using EasySpin software. A BASi Epsilon-EC electroanalytical instrument was used for cyclic voltammetric experiments in CH_2Cl_2 solutions containing 0.2 M tetrabutylammonium hexafluorophosphate as a supporting electrolyte. A BASi platinum working electrode, platinum auxiliary electrode, and Ag/AgCl reference electrode were used for the electrochemical measurements. The redox potential data reported were referenced to the ferrocenium/ferrocene (Fc^+/Fc) couple. A BASi SEC-C thin layer quartz glass spectroelectrochemical cell kit (light path length of 1 mm) with a platinum-gauze working electrode and SEC-C platinum counter electrode was used for spectroelectrochemistry measurements. Bulk electrolysis experiments (constant-potential coulometry) were performed using a platinum-gauze working electrode at 295 K.

Syntheses. *N*-(5-Nitropyridin-2-yl)quinolin-8-amine (HL). To *N,N*-dimethylformamide (10 mL) in a round-bottom flask was added 2-chloro-5-nitropyridine (316 mg, 2.0 mmol) followed by 8-aminoquinoline (288 mg, 2.0 mmol) and $NaHCO_3$ (20 mg, 0.24 mmol). The reaction mixture was refluxed in an oil bath at 393–403 K for 15 h. The resulting mixture was cooled to room temperature, giving a blackish slurry. It was poured into ice-cold water (200 mL) and stirred for 45 min. A yellowish solid separated out, which was collected upon filtration under a suction pump. The residue was dried in air. The compound was purified by column chromatography and recrystallized from a CH_3CN solution. Yellowish crystals of HL separated out, which were filtered and dried in air. Yield: 375 mg (~70% with respect to 8-aminoquinoline). Melting point: 413–416 K. Mass spectrum (ESI, positive ion, CH_3OH): m/z 267 for $[H_2L]^+$, calcd m/z 267.29 for $[H_2L]^+$. Anal. Calcd for $C_{14}H_{10}N_4O_2$ (M_w , 266.25): C, 63.15; H, 3.79; N, 21.04. Found: C, 63.03; H, 3.62; N, 21.41. 1H NMR ($CDCl_3$, 300 MHz): δ (ppm) 9.88 (s, 1H), 9.47 (d, $J = 5.2$, 1H), 9.06 (d, $J = 4.2$, 1H), 8.96 (d, $J = 7.5$, 1H), 8.84 (t, $J = 4.1$, 1H), 8.76 (t, $J = 4.4$, 1H), 8.70 (s, NH), 8.19 (t, $J = 4.2$, 1H), 6.97 (d, $J = 5.1$, 1H), 6.45 (d, $J = 5.2$, 1H). IR/ cm^{-1} (KBr): ν 3315 (s, $\nu_{N-H(air)}$), 1621 (vs, $\nu_{N-H(bend)}$), 1584 (s), 1540 (vs, $\nu_{N-O(asym)}$), 1348 (vs, $\nu_{N-O(sym)}$), 1291 (s), 1116 (s), 1045 (s), 901 (s), 821 (s), 795 (m), 753 (s), 734 (s), 536 (m).

$trans-[(L-H^+)Ru^{II}(PPh_3)_2Cl_2]$ ($1-H^+$). To HL (53 mg, 0.20 mmol) in ethanol (30 mL) was added $[Ru^{II}(PPh_3)_3Cl_2]$ (190 mg, 0.20 mmol), and the mixture was refluxed for 1.5 h under argon. The mixture was then cooled to room temperature. Black crystals of $1-H^+$ separated out, which were collected upon filtration and dried in air. Yield: 110 mg (~57% with respect to ruthenium). Mass spectrum (ESI, positive

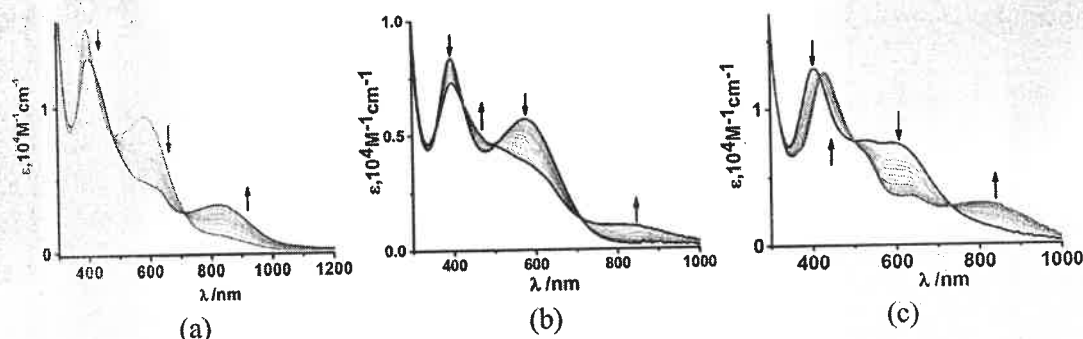


Figure 1. Change in UV-vis-NIR absorption spectra during the conversion of $1\text{-H}^+ \rightarrow 1$ in air: (a) in CH_2Cl_2 ; (b) in CH_2Cl_2 containing 0.2 mM $[\text{N}(\text{n-Bu})_4]\text{PF}_6$ as electrolyte; (c) in CH_2Cl_2 containing 0.2 mM $[\text{N}(\text{n-Bu})_4]\text{Cl}$ as electrolyte at 298 K.

ion, CH_3OH): m/z 664 for $[1 - \text{Cl} - \text{PPh}_3]^+$, calcd m/z 664.04 for $[1 - \text{Cl} - \text{PPh}_3]^+$. Anal. Calcd for $\text{C}_{50}\text{H}_{40}\text{Cl}_2\text{N}_4\text{O}_2\text{P}_2\text{Ru}$: C, 62.37; H, 4.19; N, 5.82. Found: C, 62.42; H, 4.25; N, 5.85. ^1H NMR (CDCl_3 , 300 MHz): δ (ppm) 13.4 (br, PyH^+), 10.01 (s, 1H), 9.51 (d, $J = 5.1$, 1H), 9.41 (d, $J = 6.0$, 1H), 9.32 (d, $J = 6.2$, 1H), 9.20–9.10 (m, 2H), 8.84 (m, 2H), 8.76 (t, $J = 4.0$, 1H), 7.48–7.42 (m, 15H, $-\text{PPh}_3$), 7.16–6.97 (m, 15H, $-\text{PPh}_3$). IR/ cm^{-1} (KBr): ν 3448 (br, $\nu_{\text{N-H(st)}}$), 1622 (s, $\nu_{\text{N-H(bend)}}$), 1599 (s), 1560 (m), 1505 (s, $\nu_{\text{N-O(asym)}}$), 1432 (m), 1339 (vs), 1294 (vs, $\nu_{\text{N-O(sym)}}$), 1229 (m) 1133 (m), 742 (s), 696 (s, $\nu_{\text{Ru-P(sym)}}$), 518 (s, $\nu_{\text{Ru-P(asym)}}$).

trans- $[(\text{L})\text{Ru}(\text{PPh}_3)_2\text{Cl}_2]$ ($1\text{-CH}_2\text{Cl}_2$). Diffusion of *n*-hexane into a CH_2Cl_2 solution of 1-H^+ (96 mg, 0.1 mmol) in air afforded black needles of $1\text{-CH}_2\text{Cl}_2$, which were collected upon filtration and dried in air. Single crystals for X-ray diffraction analysis were collected from this crop. Yield: 45 mg (~46% with respect to ruthenium). Mass spectrum (ESI, positive ion, CH_3OH): m/z 926 for $[1 - \text{Cl}]^+$, calcd m/z 926.13 for $[1 - \text{Cl}]^+$. Anal. Calcd for $\text{C}_{50}\text{H}_{39}\text{Cl}_2\text{N}_4\text{O}_2\text{P}_2\text{Ru}$: C, 62.44; H, 4.09; N, 5.83. Found: C, 62.48; H, 4.15; N, 5.75. IR/ cm^{-1} (KBr): ν 1586 (m), 1568 (m), 1506 (vs, $\nu_{\text{N-O(asym)}}$), 1434 (s), 1339 (vs, $\nu_{\text{N-O(sym)}}$), 1272 (s), 1290 (m), 1093 (m), 821 (s), 745 (s), 694 (s, $\nu_{\text{Ru-P(sym)}}$), 519 (s, $\nu_{\text{Ru-P(asym)}}$).

trans- $[(\text{L})\text{Ru}(\text{PPh}_3)_2(\text{CO})\text{Cl}]$ (**2**). To an HL (53 mg, 0.20 mmol) solution in toluene (30 mL) was added $[\text{Ru}^{\text{II}}(\text{H})(\text{CO})(\text{Cl})(\text{PPh}_3)_3]$ (216 mg, 0.20 mmol), and the mixture was refluxed for 15 min. A dark brown solution was obtained, and it was allowed to evaporate slowly in air at room temperature. After 5–7 days, dark red single crystals of **2** (toluene) separated out, which were collected upon filtration and dried in air. Yield: 92 mg (43% with respect to ruthenium). Mass spectral data [ESI, positive ion, CH_2Cl_2]: m/z 919 for $[2 - \text{Cl}]^+$, calcd m/z 919.15 for $[2 - \text{Cl}]^+$. Anal. Calcd for $\text{C}_{51}\text{H}_{39}\text{ClN}_4\text{O}_3\text{P}_2\text{Ru}$: C, 64.18; H, 4.12; N, 5.87. Found: C, 64.30; H, 4.19; N, 5.82. ^1H NMR (CDCl_3 , 300 MHz): δ (ppm) 10.03 (s, 1H), 9.54 (d, $J = 5.0$, 1H), 9.36 (d, $J = 6.2$, 1H), 9.29 (d, $J = 6.0$, 1H), 9.20–9.10 (m, 2H), 8.92 (m, 2H), 8.81 (t, $J = 4.0$, 1H), 7.49–7.32 (m, 15H, $-\text{PPh}_3$), 7.12–7.01 (m, 15H, $-\text{PPh}_3$). IR/ cm^{-1} (KBr): ν 1957 (vs, ν_{CO}), 1639 (s), 1585 (m), 1481 (vs, $\nu_{\text{N-O(asym)}}$), 1434 (m), 1327 (vs, $\nu_{\text{N-O(sym)}}$), 1281 (s), 1269 (s), 1250 (s), 1113 (s), 745 (s), 696 (s, $\nu_{\text{Ru-P(sym)}}$), 518 (s, $\nu_{\text{Ru-P(asym)}}$).

trans- $[(\text{L})\text{Ru}(\text{PPh}_3)_2(\text{CO})\text{Cl}]^+$ (**2** $^+$). This compound was not isolated but was generated from a bulk electrolysis experiment (constant-potential coulometric oxidation at +0.40 V versus Fc^+/Fc couple) of **2** in CH_2Cl_2 using tetrabutylammonium hexafluorophosphate as a supporting electrolyte and a platinum-gauze electrode. The solution obtained from this experiment was used directly for EPR measurements.

Single-Crystal X-ray Structure Determinations. Single crystals of HL, **1** (CH_2Cl_2 , 100 and 293 K), and **2** (toluene) (CCDC No. 1584966–1584969) were picked up with nylon loops and were mounted on Bruker APEX-II CCD and Bruker AXS D8 QUEST ECO diffractometers equipped with a Mo-target rotating-anode X-ray source and a graphite monochromator (Mo $K\alpha$, $\lambda = 0.71073$ Å). Final cell constants were obtained from least-squares fits of all measured

reflections. Intensity data were corrected for absorption using intensities of redundant reflections. The structures were readily solved by direct methods and subsequent difference Fourier techniques. The SHELXS-97 (Sheldrick 2008) software package was used for solution, and SHELXL-2014/6 (Sheldrick, 2014) was used for the refinement.¹⁰ All non-hydrogen atoms were refined anisotropically. Hydrogen atoms were placed at calculated positions and refined as riding atoms with isotropic displacement parameters.

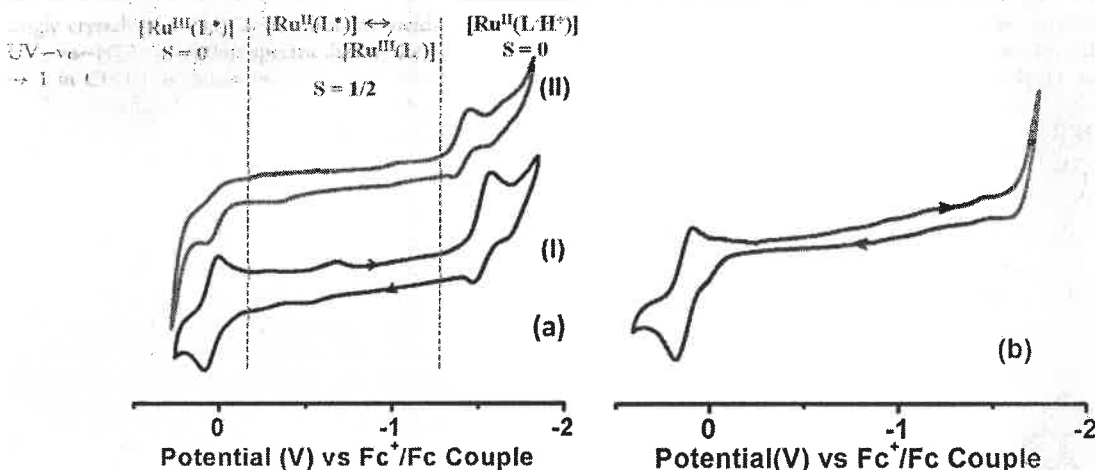
Density Functional Theory (DFT) Calculations. All DFT calculations were performed with the ORCA program package.¹¹ Geometries of **1** and **1** $^+$ using doublet and singlet spin states were successfully optimized using a pure density functional BP method.¹² For comparison, the geometry of **1** was also optimized with a B3LYP¹³ hybrid DFT¹⁴ method. Similarly, geometries of **2** and **2** $^+$ were optimized using a pure density functional BP method. For all calculations, the all-electron valence double- ζ def2-SVP¹⁵ basis set with “new” polarization function developed by the Karlsruhe group was used for P, N, Cl, O, C, and H atoms. For the Ru atom def2-TZVP,¹⁵ a valence triple- ζ basis set with new polarization function, was used. Resolution of identity (RI)¹⁶ and RIJCOSX¹⁷ approximation with a def2/J auxiliary basis set for Coulomb and HF exchange integral for HF and hybrid DFT methods were employed for self-consistent field (SCF) gradient calculations.¹⁸ The geometry optimizations were carried out in redundant internal coordinates without imposing symmetry constraints. The SCF calculations were converged tightly (1×10^{-8} Eh in energy, 1×10^{-7} Eh in the density change, and 1×10^{-7} in maximum element of the DIIS error vector). To perform time-dependent (TD) DFT¹⁹ calculations, the geometries of **1** and **2** were optimized by the BP/DFT method in CH_2Cl_2 using the conductorlike polarizable continuum mode (CPCM).²⁰ TDDFT calculations for electronic absorption spectra were carried out using B3LYP and CAM-B3LYP²¹ functionals in CH_2Cl_2 with application of the CPCM model to screen the effects of solvent.

RESULTS AND DISCUSSION

Syntheses and Characterization. The diarylamine ligand and amido and aminyl radical complexes reported in this paper are shown in Chart 1. Details of the syntheses and their characterization data are outlined in the Experimental Section. HL was isolated in high yields from a single-step reaction of 2-chloro-5-nitropyridine and 8-aminoquinoline (1:1) in *N,N*-dimethylformamide at 393 K. Reaction of HL with $[\text{Ru}^{\text{II}}(\text{PPh}_3)_3\text{Cl}_2]$ in boiling ethanol afforded the zwitterionic amido complex 1-H^+ in good yields, while a similar reaction of HL with $[\text{Ru}^{\text{II}}(\text{H})(\text{CO})(\text{Cl})(\text{PPh}_3)_3]$ in boiling toluene produced the amido complex **2** (toluene). **2** is stable in solution. In contrast, 1-H^+ in CH_2Cl_2 in air suffers one-electron oxidation, furnishing the paramagnetic complex **1** ($\mu_{\text{eff}} = 1.75 \mu_{\text{B}}$ at 293 K). Diffusion of *n*-hexane into a dichloromethane solution of 1-H^+ at 298 K in air produces

Table 1. Redox Potentials of 1^-H^+ and **2** in CH_2Cl_2 Referenced to the Fc^+/Fc Redox Couple Determined by Cyclic Voltammetry at 298 K

compd	electrolyte	$E_{1/2}$, V (ΔE , mV)		
		$[(L^*)Ru^{II}]/[(L^-H^+)Ru^{II}]$	$[(L^*)Ru^{II}]/[(L^-)Ru^{II}]$	$[(L^*)Ru^{III}]/[(L^*)Ru^{II}]$
1^-H^+	$[N(n-Bu)_4]PF_6$	-1.57 (100)		0.00 (90)
	$[N(n-Bu)_4]Cl$	-1.40 (90)		0.00 (80)
2	$[N(n-Bu)_4]PF_6$		+0.14 (76)	

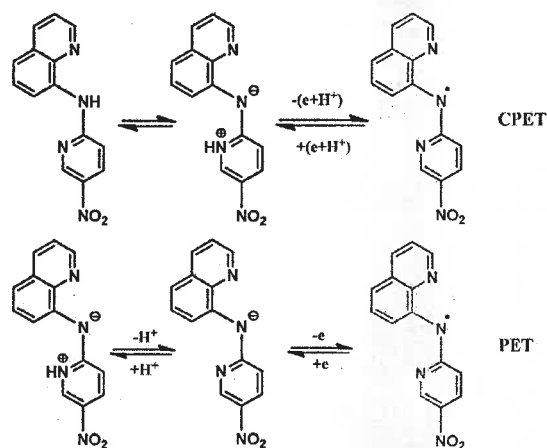
**Figure 2.** Cyclic voltammograms of (a) 1^-H^+ using (I) 0.2 M $[N(n-Bu)_4]PF_6$ and (II) 0.2 M $[N(n-Bu)_4]Cl$ as supporting electrolytes and (b) **2** using 0.2 M $[N(n-Bu)_4]PF_6$ as a supporting electrolyte in CH_2Cl_2 at 298 K. Conditions: scan rate, 100 $mV s^{-1}$; platinum working electrode; potential referenced to Fc^+/Fc redox couple.

single crystals of $1 \cdot CH_2Cl_2$ in moderate yields. The change in UV-vis-NIR absorption spectra during the conversion $1^-H^+ \rightarrow 1$ in CH_2Cl_2 is shown in Figure 1.

The ν_{N-H} band of HL appears at 3315 cm^{-1} . In the 1H NMR spectrum the NH proton appears as a singlet at δ 8.70 ppm. In 1^-H^+ , the NH proton shifts to the pyridine N atom, resulting in the formation of a zwitterionic amido coordinated to a ruthenium(II) ion. The $N_{py}H$ stretching and bending vibrations of 1^-H^+ appear respectively at 3400 (br) and 1622 cm^{-1} . The 1H NMR spectrum of 1^-H^+ displays a broader peak at δ 13.4 ppm due to the $[N_{py}H]^+$ proton.

Proton-Coupled Oxidation. The redox activities of 1^-H^+ and **2** were investigated by cyclic voltammetry in CH_2Cl_2 at 298 K using tetrabutylammonium hexafluorophosphate ($[N(n-Bu)_4]PF_6$) and tetrabutylammonium chloride ($[N(n-Bu)_4]Cl$) as supporting electrolytes. The redox potential data given in Table 1 were referenced to the ferrocenium/ferrocene (Fc^+/Fc) couple. The redox activity of 1^-H^+ significantly depends on the supporting electrolyte used for the study. In the presence of $[N(n-Bu)_4]Cl$, 1^-H^+ exhibits an anodic wave at -1.40 V due to the $[Ru^{II}(L^*)]/[Ru^{II}(L^-H^+)]$ redox couple, as shown in Figure 2a. The same redox couple shifts to -1.57 V in the presence of $[N(n-Bu)_4]PF_6$ salt. The effect of deprotonation of the L^-H^+ ligand that contains a protonated pyridine moiety in the presence of these electrolytes is analyzed. Pyridinium chloride ($pK_a = 5.25$) is a weaker acid than HCl ($pK_a = -7$) and HPF_6 ($pK_a = -20$). On consideration of these parameters, both HPF_6 and HCl are stronger acids and PF_6^- is the weakest conjugated base. In the presence of the electrolytes used for electrochemical study 1^-H^+ does not undergo deprotonation extensively and deprotonation is the least in the presence of $[N(n-Bu)_4]PF_6$.

The protonated L^-H^+ form in the electrochemical cell promotes a proton-coupled oxidation defined as a CPET reaction, as illustrated in Scheme 1, while the same reaction is

Scheme 1. Proton-Coupled Oxidation of 1^-H^+ 

not feasible with the deprotonated L^- form. Thus, the deprotonation of the L^-H^+ ligand results in a positive shift of the redox potential. Expectedly, the redox potentials are relatively higher with the $[N(n-Bu)_4]Cl$ salt, as Cl^- is a stronger conjugate base in comparison to PF_6^- . Following the reaction equilibrium as $1^-H^+ + Cl^- \rightleftharpoons 1^- + HCl$, in the presence of $[N(n-Bu)_4]Cl$, 1^- is generated more and a positive shift of the potential is seen.

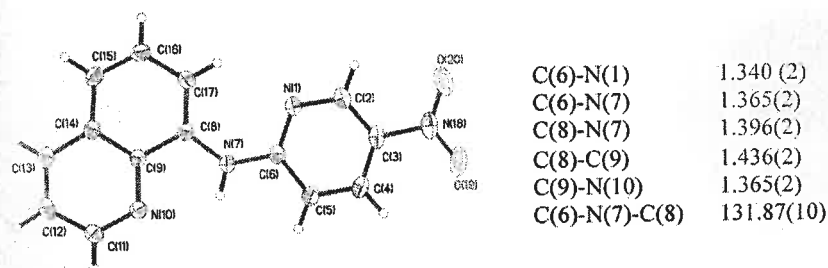


Figure 3. Molecular geometry and selected experimental bond parameters of HL in the crystal form (50% thermal ellipsoids).

The proton-coupled $1^-\text{H}^+ \rightarrow 1$ oxidations in the presence of all these electrolytes are not reversible ($i_a/i_c \neq 1.0$, where i_a and i_c refer to anodic and cathodic current, respectively). The conversion $1^-\text{H}^+ \rightarrow 1$ involves a concerted proton–electron transfer, while the reverse transformation may not involve proton and produces 1^- . The second anodic wave of 1^-H^+ detected in the presence of $[\text{N}(n\text{-Bu})_4]\text{PF}_6$ and $[\text{N}(n\text{-Bu})_4]\text{Cl}$ at 0.0 V is reversible, and the potential of the redox process does not depend on the electrolyte. Bulk electrolysis of 1^-H^+ at +0.20 V affords an EPR-silent solution, while the oxidation 1^-H^+ at −1.2 V by a constant-potential bulk electrolysis experiment generates **1** that contains an organic radical, $[\text{Ru}^{\text{II}}(\text{L}^\bullet)]$. This is due to the conversion of 1^-H^+ to 1^+ containing the antiferromagnetically coupled $[\text{Ru}^{\text{III}}(\text{L}^\bullet)]$ state at +0.20 V. Thus, the second anodic wave is assigned to a ruthenium(III)/ruthenium(II) redox couple. The cyclic voltammogram of **1** also displays a similar anodic wave at 0.0 V due to the ruthenium(III)/ruthenium(II) redox couple. The change in UV–vis spectra during $1^-\text{H}^+ \rightarrow 1^+$ conversion is illustrated in Figure S2a recorded by a spectroelectrochemical measurement. Speciation due to application of the potential of −1.8 to +0.5 V in different segments is shown in Figure 2a. Notably, in the voltammetry study of 1^-H^+ using $[\text{N}(n\text{-Bu})_4]\text{PF}_6$ as an electrolyte, the first scan from −1.0 to +0.3 V is similar to the equilibrium scans, while the first scan from −1 to −1.7 V is different from the equilibrium scans. The anodic wave at 0.0 V is observed in the first scan from −1.0 to +0.3 V (see, Figure S3a), but no cathodic wave at −1.57 V was detected in the first scan from −1 to −1.7 V (see, Figure S3b), implying that the redox wave of 1^-H^+ at −1.57 V is an anodic wave due to the oxidation of $1^-\text{H}^+ \rightarrow 1$.

1^-H^+ is unstable in solution and undergoes oxidation, affording **1**. The rate of oxidation of 1^-H^+ significantly depends on the composition of the medium. The kinetics of the reaction was investigated in dry CH_2Cl_2 and $\text{H}_2\text{O}-\text{CH}_2\text{Cl}_2$ and $\text{D}_2\text{O}-\text{CH}_2\text{Cl}_2$ solvent mixtures. The last two solvent mixtures were prepared by vigorously shaking dry CH_2Cl_2 (10 mL) with H_2O (0.25 mL) and D_2O (0.25 mL), respectively. The reactions were followed by considering the decay of absorbance of 1^-H^+ at 600 nm in the presence of air, and the rate was calculated using the integrated first order rate law $\ln[A] = -kt + \ln[A]_0$, where $\ln[A]$ vs time t gives a straight line with slope of $-k$. The experimental plots of $\log[\text{absorbance}]$ vs t in three cases are depicted in Figure S1, which authenticated that k increases with the basicity of the protic solvent component. In dry CH_2Cl_2 , k is $6.7 \times 10^{-5} \text{ s}^{-1}$, and in moist CH_2Cl_2 it is $8.0 \times 10^{-5} \text{ s}^{-1}$, while k has a maximum in $\text{D}_2\text{O}-\text{CH}_2\text{Cl}_2$, $11 \times 10^{-5} \text{ s}^{-1}$. Notably, D_2O is more basic than H_2O (the pD of D_2O is 7.3, while the pH of H_2O is 7.0) and k is relatively higher in the $\text{D}_2\text{O}-\text{CH}_2\text{Cl}_2$ mixture. We failed to

measure the rate using an organic base (e.g., Et_3N) or alcoholic solvent (e.g., MeOH and EtOH), as the oxidized arylamino radical is reactive and decomposes more quickly. The order of rate constants, $k_{\text{D}_2\text{O}-\text{CH}_2\text{Cl}_2} > k_{\text{H}_2\text{O}-\text{CH}_2\text{Cl}_2} > k_{\text{CH}_2\text{Cl}_2}$, demonstrates that the deprotonation makes the electron transfer reaction faster and the reaction is defined as a CPET reaction. The rate of oxidation of 1^-H^+ in CH_2Cl_2 containing 0.2 M $[\text{N}(n\text{-Bu})_4]\text{PF}_6$ is $8.8 \times 10^{-5} \text{ s}^{-1}$, which is similar to that measured in moist CH_2Cl_2 . The rate of oxidation does not depend on the concentration of electrolyte. The rate is $10 \times 10^{-5} \text{ s}^{-1}$ in CH_2Cl_2 containing 0.4 mM $[\text{N}(n\text{-Bu})_4]\text{PF}_6$. The redox reaction of 1^-H^+ in air was also investigated following the above procedure in CH_2Cl_2 containing 0.2 mM $[\text{N}(n\text{-Bu})_4]\text{Cl}$ salt. The rate with $[\text{N}(n\text{-Bu})_4]\text{Cl}$ is relatively higher and depends on the concentration of the electrolyte. It is consistent with the higher basicity of the Cl^- ion. The rate is $30 \times 10^{-5} \text{ s}^{-1}$ in CH_2Cl_2 containing 0.2 mM $[\text{N}(n\text{-Bu})_4]\text{Cl}$. The changes in the spectra during oxidation of 1^-H^+ in CH_2Cl_2 containing 0.2 mM $[\text{N}(n\text{-Bu})_4]\text{PF}_6$ and 0.2 mM $[\text{N}(n\text{-Bu})_4]\text{Cl}$ electrolytes are shown in Figure 1b,c. However, with an increase in the reaction time, the reaction does not follow first-order kinetics (see Figure S1f). The deviation is due to the reaction of the chloride ion with the oxidized product, and the reaction is not further investigated here.

The effect of protonation/deprotonation is not observed in the cyclic voltammogram of **2**, and the $2/2^+$ redox couple is reversible. **2** exhibits a reversible anodic wave at 0.14 V due to the $\text{L}^\bullet/\text{L}^-$ redox couple, as shown in Figure 2b. The $2^+/2$ redox couple is similar to the $1^-\text{H}^+/1$ redox couple, except that the former couple is shifted to higher potential because of the coordinated π -acidic CO ligand stabilizing the 18e species. Approximately the shift of potential of the $2^+/2$ couple can be estimated by considering the ligand electrochemical parameters²² of CO/Cl and the effect of one proton on the $[\text{Ru}^{\text{II}}(\text{L}^-\text{H}^+)] \rightarrow [\text{Ru}^{\text{II}}(\text{L}^\bullet)]$ conversion. Replacing a chloride ligand by CO would shift the potential positively by 1.23 V.²² In addition, $1^-\text{H}^+ \rightarrow 1$ is a proton-coupled oxidation, while $2 \rightarrow 2^+$ conversion does not involve a proton. The latter conversion will occur at higher potential (by ~0.5 V) in comparison to the former. The potential of the $2^+/2$ redox couple will expectedly shift positively by 1.73 V, and the same is observed in our case with an experimental shift of +1.71 V. The EPR spectrum of the 2^+ ion obtained from a constant-potential coulometric experiment confirmed that 2^+ is a paramagnetic ion (vide infra) and contains an organic radical, different from 1^+ , which is a diamagnetic ion. The change in absorption spectra during $2 \rightarrow 2^+$ conversion was recorded by spectroelectrochemical measurements and is shown in Figure S2b.

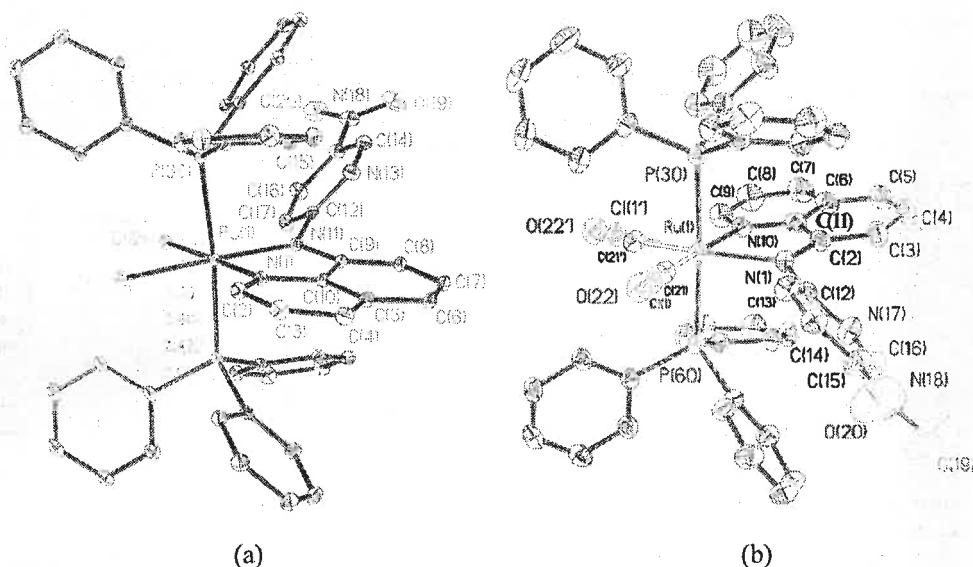


Figure 4. Molecular geometries of (a) 1-CH₂Cl₂ and (b) 2-(toluene) in the crystal form (50% thermal ellipsoids; solvent molecules and hydrogen atoms are omitted for clarity).

Table 2. Selected Experimental Bond Lengths (Å) of 1-CH₂Cl₂ and the Corresponding Calculated Bond Lengths of 1 and 1[−] with Doublet and Singlet Spin States

	exptl		calcd		
	1-CH ₂ Cl ₂ (100 K)	1-CH ₂ Cl ₂ (293 K)	1	1	1 [−]
			BP/DFT	B3LYP/DFT	BP/DFT
Ru–Cl(1)	2.404(1)	2.401(1)	2.402	2.402	2.479
Ru–Cl(2)	2.439(1)	2.436(1)	2.436	2.437	2.488
Ru–P(30)	2.400(1)	2.418 (1)	2.418	2.418	2.401
Ru–P(60)	2.427(1)	2.431 (1)	2.431	2.431	2.378
Ru–N _Q	2.066(2)	2.078(3)	2.077	2.077	2.042
Ru–N _{aminy}	2.037(2)	2.046(3)	2.045	2.045	2.133
C _Q –N _{aminy}	1.401(2)	1.405(4)	1.406	1.406	1.386
C _{py} –N _{aminy}	1.394(2)	1.389(4)	1.388	1.388	1.384

Molecular Structures. The molecular and electronic structures of the complexes were elucidated by single-crystal X-ray bond parameters, fluid and frozen glass EPR spectral parameters, and density functional theory (DFT) calculations. The bond parameters of the three forms of the ligand, i.e., amine (HL), aminyl radical (L[•]), and amido (L[−]), were analyzed by single-crystal X-ray structure determinations of HL, 1-CH₂Cl₂, and 2-(toluene). The crystallographic data of HL, 1-CH₂Cl₂, and 2-(toluene) are given in Table S1. The gas-phase and solution optimized coordinates of the related species are given in the Supporting Information.

HL crystallizes in space group $P\bar{1}$. The molecular geometry of HL in the crystal form and the atom labeling scheme are illustrated in Figure 3. The significant bond parameters are summarized in Figure 3. The C(8)–NH and C(6)–NH lengths are 1.396(2) and 1.365(2) Å, respectively.

1-CH₂Cl₂ and 2-(toluene) crystallize in space group $P2_1/n$. The molecular geometries of 1-CH₂Cl₂ and 2-(toluene) in the crystal form with the atom-labeling scheme are illustrated in Figure 4a,b, respectively. In the case of 1-CH₂Cl₂, the diffraction study was conducted at 293 and 100 K and the significant bond parameters are summarized in Table 2. Notably, the experimental lengths at both temperatures are

comparable. Two bulky PPh₃ ligands lie trans to each other. The Ru–PPh₃ length significantly depends on the oxidation state and the coligands of the ruthenium ion.²³ As PPh₃ is a π -acidic ligand, a Ru^{II}–PPh₃ bond is notably shorter than a Ru^{III}–PPh₃ bond. In the case of 1-CH₂Cl₂, the average Ru–PPh₃ length is 2.413(2) Å, which is relatively shorter than a Ru^{III}–PPh₃ length.²³ Similarly, the Ru–Cl distances, 2.421(1) Å, are relatively longer than those observed in a ruthenium(III) complex.²⁴ The trend of the bond parameters does not confirm that 1-CH₂Cl₂ is an amido complex of ruthenium(III); rather, the lengths are intermediate between those found in cases of ruthenium(II) and ruthenium(III) species. Thus, 1 is considered to be a complex that exhibits resonance forms of the types $[(L^-)Ru^{III} \leftrightarrow (L^{\bullet})Ru^{II}]$. Complexes revealing such resonance forms have been previously discussed in several aspects.²⁵ The Ru–N_Q and Ru–N_{aminy} lengths in 1-CH₂Cl₂ are 2.066(2) and 2.037(2) Å, respectively.

In 2-(toluene) the CO and chloride ligands are crystallographically disordered. The structure was refined with an occupancy of 0.5 for both the chlorine and CO molecules for each of the octahedral sites. The ORTEP plot of 2-(toluene) displays one of the disordered positions of the chloride and CO ligands. The significant bond parameters are summarized

in Table 3. The bond parameters of the coordination sphere of 2·(toluene) are similar to those observed in the case of 1·

Table 3. Selected Experimental Bond Lengths (Å) of 2·(toluene) and the Corresponding Calculated Bond Lengths of 2 and 2⁺, Respectively, with Singlet and Doublet Spin States

	exptl 2·(toluene)	caled	
		2	2 ⁺
Ru–C(21)	1.819(7)	1.840	1.849
Ru–Cl(1)	2.410(2)	2.459	2.409
Ru–P(30)	2.411(2)	2.432	2.496
Ru–P(60)	2.401(2)	2.432	2.487
Ru–N _{amido}	2.130(3)	2.139	2.044
Ru–N _Q	2.131(3)	2.153	2.156
C _{py} –N _{amido}	1.372(4)	1.390	1.420
C _Q –N _{amido}	1.396(4)	1.391	1.391

CH₂Cl₂. The average Ru–PPh₃ length in 2·(toluene) is 2.406(2) Å. The disordered Ru–Cl length is 2.410(2) Å. The Ru–N_Q and Ru–N_{amido} lengths are 2.131(3) and 2.130(3) Å, respectively, which are relatively longer than those in 1·CH₂Cl₂; this may be due to the trans CO ligand.

It is established that the bond parameters of the coordinated L in 1·CH₂Cl₂ are significantly different from those of HL and L[–] in 2·(toluene). Bond lengths around the N center of these three different forms are summarized in Chart 2. The C_Q–N and C_{py}–N lengths in 1·CH₂Cl₂ are 1.401(2) and 1.394(2) Å, respectively, which are longer than those recorded in HL and 2·(toluene). The C_{py}–N distances (a) are comparable in HL and 2·(toluene) due to the participation of the lone pair of N in resonance with the –NO₂ substitution of the pyridine ring, while upon oxidation the effect of resonance is reduced and the length a in L[•] of 1·CH₂Cl₂ increases notably. The trend of a in HL, L[–], and L[•] is as follows: a(L[•]) > a(L[–]) > a(HL). Similarly, C_Q–N lengths (b) follow the trend b(L[•]) > b(HL) ≈ b(L[–]).

EPR Spectroscopy. The variable-temperature EPR spectra of the crystals and the frozen CH₂Cl₂ glass of 1 were recorded at 113–298 K. The experimental and simulated spectra are illustrated in Figure 5. The simulated parameters are summarized in Table 4. Notably, the EPR spectra of crystal and solution samples depend significantly on temperature, as depicted in Figure 5a. At 298 K the spectrum of the crystals is relatively broader. The simulation of the EPR spectrum of the crystal at 133 K was achieved considering two paramagnetic components, [(L[–])Ru^{III}] and [(L[•])Ru^{II}], in 1:1 ratio as given in Figure 5b. The isotropic signal of the [(L[•])Ru^{II}] component appears at g = 2.001. The rhombic spectrum obtained from the

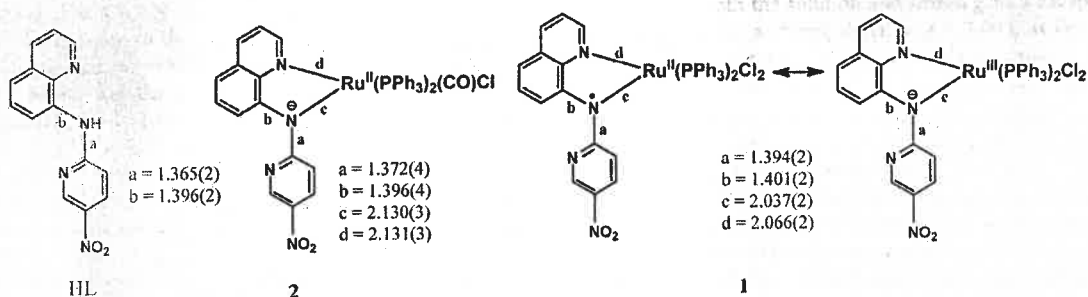
ruthenium(III) component at 133 K displays hyperfine splitting due to the ^{35,37}Cl (I = 3/2) nucleus (see spectrum iii of Figure 5b), and the simulated coupling constants A₁ and A₂ are respectively 46 and 43 G. The simulated spectrum ii of Figure 5b was achieved from spectra ii and iv, implying that 1 is a hybrid of [(L[–])Ru^{III}(PPh₃)₂Cl₂] (g₁ = 2.260, g₂ = 2.131, g₃ = 1.903) and [(L[•])Ru^{II}(PPh₃)₂Cl₂] (g = 2.001) resonance forms, as shown in Chart 2. The anisotropy (Δg) due to the ruthenium(III) ion is 0.36. The higher anisotropy and the hyperfine splitting due to the ^{35,37}Cl (I = 3/2) nucleus are markers of the larger contribution of the ruthenium(III) component in 1 at 113 K.

The EPR spectrum of the frozen CH₂Cl₂ glass of 1 at 113 K is also rhombic and is significantly different from that of the crystals. The simulation of the frozen glass spectrum that displays no hyperfine splitting was also achieved considering [(L[–])Ru^{III}] (g₁ = 2.272, g₂ = 2.231, g₃ = 2.015) and [(L[•])Ru^{II}] (g = 2.003) components (1:1), as depicted in Figure 5c. The relatively smaller anisotropy (0.26) predicts a larger contribution of the [(L[•])Ru^{II}] form in solution in comparison to that in the crystals. The EPR signal of the CH₂Cl₂ solution of 1 is also relatively broader, as shown in Figure 5d. The value g_{avg} = 2.185 deviates significantly from that of an organic radical because of the contribution of the [(L[–])Ru^{III}] resonance form. The unambiguous assignment of the hyperfine splitting due to the ¹⁴N (I = 1) nucleus was not possible with this spectrum.

The EPR study authenticates the contributions of [(L[–])Ru^{III}] and [(L[•])Ru^{II}] components (see Chart 2) to the ground electronic state of 1. However, the contributions of these two resonance forms in the solid and in solution are not equal. On the contrary, both the solution and frozen glass EPR spectra of the 2⁺ ion exhibit a strong signal at g = 2.003, as depicted in Figure 5e, and the spectrum was simulated considering only the [(L[•])Ru^{II}] form. This implies that the 2⁺ ion is an aminyl radical (L[•]) complex of ruthenium(II). Unfortunately, no hyperfine splitting due to the ¹⁴N (I = 1) nucleus was observed in the cases of 1 and 2⁺ ion and no contribution of [(L[–])Ru^{III}] component to 2⁺ ion was detected by EPR spectroscopy.

Density Functional Theory (DFT) Calculations. The electronic structures of 1[–], 1, 2, and 2⁺ were further elucidated by DFT calculations. The gas-phase geometries of 1[–] and 2 were optimized with a singlet spin state, while those of 1 and 2⁺ were optimized with a doublet spin state by a pure BP/DFT method¹² using the def2-TZVP basis set for ruthenium and the def2-SVP basis set for all other atoms. For comparison, the gas-phase geometry of 1 was also optimized with the hybrid B3LYP functional. The calculated bond parameters of 1 from both methods are similar, as given in Table 2. The calculated bond parameters of 2 and 2⁺ are given in Table 3. The

Chart 2. Significant X-ray Bond Lengths of HL, L[–], and L[•] Forms in HL, 2·(toluene), and 1·CH₂Cl₂



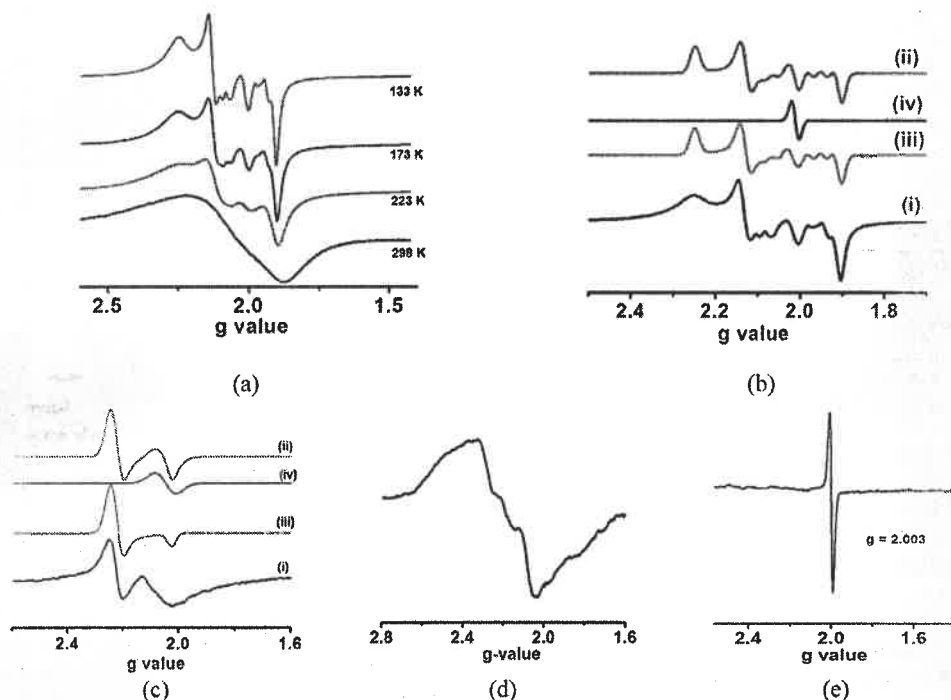


Figure 5. X-band EPR spectra of (a) crystals of **1** (variable temperature) and (b) simulation at 133 K considering $[(L^*)Ru^{II}]$ and $[(L^-)Ru^{III}]$ components ((i) experimental spectrum, (ii) simulated spectrum, (iii) spectrum due to $[(L^-)Ru^{III}]$ component, (iv) spectrum due to $[(L^*)Ru^{II}]$ component), (c) frozen CH_2Cl_2 glass of **1** at 113 K and simulation ((i) experimental spectrum, (ii) simulated spectrum, (iii) spectrum due to $[(L^-)Ru^{III}]$, and (iv) spectrum due to $[(L^*)Ru^{II}]$ components), (d) CH_2Cl_2 solution of **1** at 298 K, and (e) frozen CH_2Cl_2 glass of **2⁺** at 113 K.

Table 4. Simulated EPR Spectral Parameters of **1** and **2⁺**

compd	state	temp (K)	$[(L^*)Ru^{II}]$ component g_1	$[(L^-)Ru^{III}]$ component			coupling constant A (^{55}Fe , $I = 3/2$)	
				g_1	g_2	g_3	A_1 (G)	A_2 (G)
1	crystal	133	2.001	2.260	2.131	1.903	46	43
	frozen glass	113	2.003	2.272	2.231	2.015		
	CH_2Cl_2	298	2.185					
2⁺	CH_2Cl_2	298	2.003					
	CH_2Cl_2	113	2.003					

geometries of **1** and **2** were also optimized in CH_2Cl_2 using the CPCM model for TDDFT calculations.

The calculated Ru–Cl and average Ru–P and Ru–N_{amido} lengths are 2.479, 2.389, and 2.133 Å, respectively, which correlate well with the existence of ruthenium(II) in the **1[−]** ion. An analysis of the molecular orbitals of **1[−]** implies that there is significant mixing between d_{Ru} and ligand molecular orbitals, as shown in Figure 6. The HOMO of **1[−]** is constituted of both d_{Ru} and p_N orbitals, while HOMO-1 and HOMO-2 are two other ruthenium-based t_{2g} orbitals. The LUMO is dominantly localized on the nitro-pyridine fragment, and the LUMO+1 scatters on the quinoline fragment.

Notably, the calculated bond parameters of **1** are similar to those obtained from the single-crystal X-ray diffraction study of **1**· CH_2Cl_2 (see Table 2). The calculated bond lengths of **1[−]** and **1** are significantly different; in particular, the Ru–N_{amido} (2.045 Å) and Ru–Cl (2.402 Å) lengths of **1** are shorter than those of **1[−]**, while the average Ru–P lengths (2.424 Å) of **1** are significantly longer. The feature can be analyzed by considering the partial oxidation of ruthenium(II) ion to ruthenium(III) in **1**. The calculated C_{py} –N[•] and C_Q –N[•] lengths of **1** are 1.388

and 1.406 Å, respectively, while the corresponding experimental lengths of **1**· CH_2Cl_2 are 1.394(2) and 1.401(2) Å at 100 K. The corresponding C_{py} –N_{amido} and C_Q –N_{amido} lengths of **1[−]** are 1.384 and 1.386 Å. The subtle difference in the C_Q –N lengths in **1[−]** and **1** can be estimated by the conversion of the amido to the aminyl form.

Analyses of the frontier MOs give an idea about the mixing of d_{Ru} with the ligand orbitals in **1** and **2⁺**. The SOMO of **1** is constituted of ruthenium (25%) and a ligand fragment; the β -HOMO scatters dominantly on ruthenium (40%), chloride (15%), and ligand. Notably, the β -LUMO is composed of ruthenium (23%) and ligand (40%), while the α -LUMO is localized on the ligand backbone. Similarly, the SOMO of the **2⁺** ion is composed of ruthenium (19%) and ligand fragment (62%) and the β -HOMO is a mixture of ruthenium (33%), chloride (28%), and ligand (32%) orbitals.

Plots of atomic spin obtained from the Mulliken spin-population analysis of **1** using BP and B3LYP methods are illustrated in Figures 7a,b. The calculated atomic spin densities are given in the figure caption. The spin scatters over ruthenium (55%), one of the chlorine (6%) atoms, and the

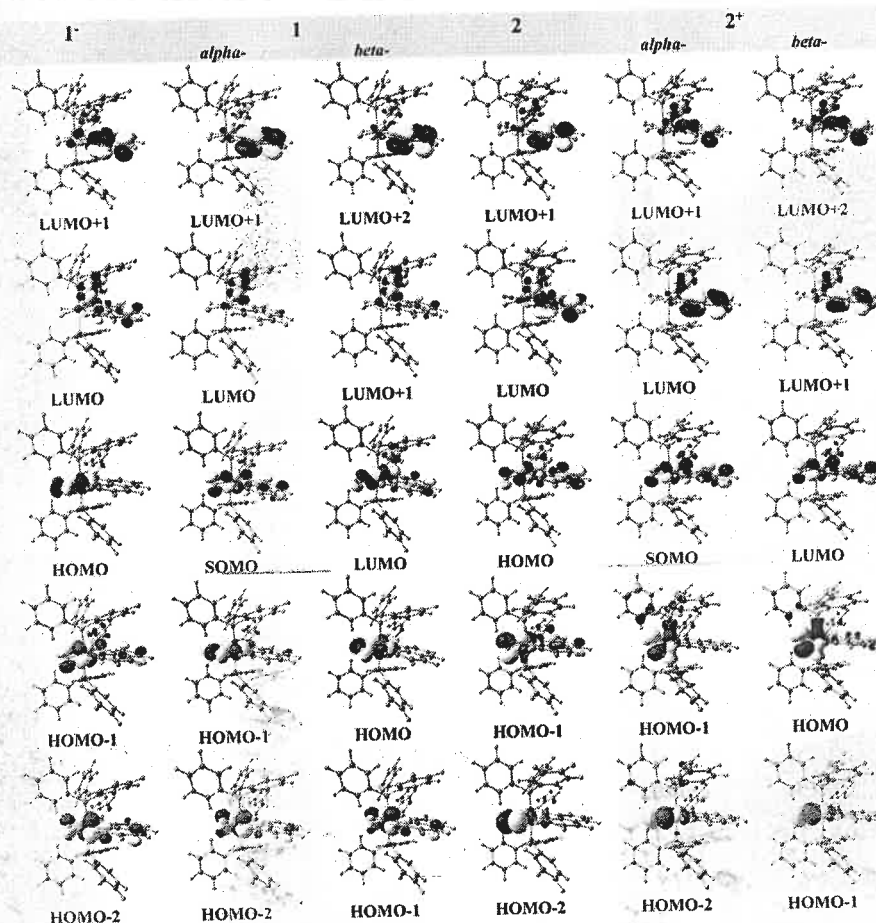


Figure 6. Frontier molecular orbitals of 1^- , 1 , 2 , and 2^+ .

ligand backbone (39%). The effect of the $-\text{NO}_2$ group on the spin distribution in 1 was estimated by optimizing the gas-phase geometry of $1'$ with a doublet spin state, where $1'$ contains *N*-(pyridin-2-yl)quinolin-8-amine as a ligand. It has been established that the frontier molecular orbitals of $1'$ are similar to those of 1 , except that the LUMO of $1'$ is delocalized on the quinoline fragment. The spin density of $1'$ also disperses over ruthenium (55%), one of the chlorine (6%) atoms, and the ligand backbone (43%), as illustrated in Figure 7c.

The DFT calculations reveal that the ground electronic state of 1 is delocalized and can be presented as a hybrid of $[(L^\bullet)\text{Ru}^{\text{II}}]$ and $[(L^-)\text{Ru}^{\text{III}}]$ forms. A similar state was predicted from the variable-temperature EPR spectra (*vide supra*). The calculated spin on the ligand backbone is relatively smaller in comparison to that of the first aminyl radical complex of rhodium(I),⁶¹ where 57% spin density is localized on the nitrogen atom. In both cases localization of spin on the nitrogen p orbital along with the metal d orbital is noteworthy.

The calculated bond lengths of 2 correlate well to those of 2 obtained from a single-crystal X-ray diffraction study (see Table 3). The calculated bond lengths of 2 are similar to those of 1^- , except that the $\text{Ru}-\text{N}_{\text{amido}}$ length in 2 is longer than that in 1^- . This is the effect of the CO ligand trans to the $\text{Ru}-\text{N}_{\text{amido}}$ bond present in 2 . The analysis affirms that the coordination spheres of 1^- and 2 are approximately similar.

The calculated $\text{Ru}-\text{Cl}$ (2.409 Å) and $\text{Ru}-\text{N}_{\text{amido}}$ (2.044 Å) lengths of 2^+ are significantly shorter than those of 2 , while the average $\text{Ru}-\text{P}$ (2.492 Å) length of 2^+ is longer. The $\text{C}_{\text{py}}-\text{N}$ length of 2^+ is significantly longer than that of 2 . A similar trend was observed during the transformation of 1^- to 1 . The constituents of the frontier molecular orbitals of 1^- and 2 are also similar, except that the contribution of d_{Ru} to the HOMO of 2 is smaller than that in 1^- , as illustrated in Figure 6. The HOMO of 2 dominantly disperses on the ligand backbone. Expectedly, the spin density is dominantly localized on the ligand backbone (62%), particularly on the aminyl N atom (35%) in the 2^+ ion, as depicted in Figure 7d. Thus, the contributions of both $[(L^\bullet)\text{Ru}^{\text{II}}]$ and $[(L^-)\text{Ru}^{\text{III}}]$ forms in 1 and the 2^+ ion were predicted. The calculations also imply a larger contribution of the $[(L^\bullet)\text{Ru}]$ form in the 2^+ ion, and the same was established by EPR spectroscopy.

UV-Vis-NIR Absorption Spectra and TDDFT Calculations. The UV-vis-NIR spectra of HL and 1^- , 1 , 2 , and 2^+ complexes were recorded in CH_2Cl_2 at 298 K. Data are summarized in Table 5, and the spectra are shown in Figure 8. HL absorbs strongly at 389 nm. The spectrum of 1^- is different and displays maxima at 395 and 583 nm; the latter band significantly diminishes during $1^- \rightarrow 1$ conversion, as shown in Figure 8b. 1 exhibits a NIR absorption band at 830 nm. The conversion of 1^- to 1 in at 298 K in air occurs via several isosbestic points, which were recorded by time-

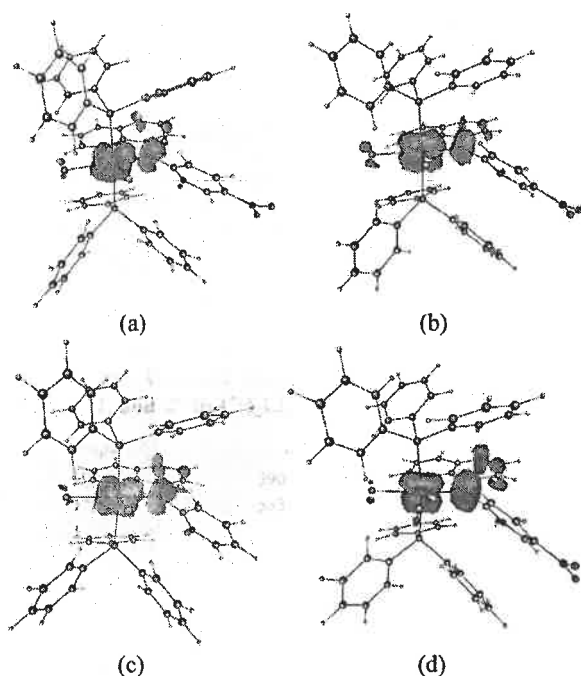


Figure 7. Spin density plots obtained from the Mulliken spin-population analyses of **1** by (a) BP/DFT (spin density: Ru, 0.54; L, 0.40 (N11, 0.17; C8, 0.09; C6, 0.09); Cl1, 0.06) and (b) B3LYP/DFT methods (spin density: Ru, 0.68; L, 0.34 (N11, 0.15; C8, 0.08; C6, 0.07); Cl1, 0.06), (c) the Mulliken spin density plots obtained from the unrestricted BP/DFT calculations on **1'** (spin density: Ru, 0.55; L, 0.43 (N11, 0.18; C8, 0.11; C6, 0.11); Cl1, 0.06), and (d) **2*** (spin density: Ru, 0.31; L, 0.64 (N1, 0.27, C3, 0.17; C5, 0.15); Cl, 0.06) with isovalue 0.005.

Table 5. UV–Vis–NIR Absorption Spectral Data of HL, **1**[−]H⁺, **1**, **2**, and **2*** in CH₂Cl₂ at 298 K

compd	λ_{max} , nm (ϵ , 10 ³ M ^{−1} cm ^{−1})
HL	390 (2.15), 310 (0.51), 246 (2.74)
1 [−] H ⁺	583 (0.95), 395 (1.66)
1	830 (0.33), 630 (0.43), 400 (1.34)
2	555 (0.78), 445 (0.36), 375 (0.32)
2*	840 (0.07), 560 (0.42), 425 (0.35)

dependent UV–vis–NIR absorption spectra as shown in Figure 1. The absorption spectrum of **2** displays an absorption band at 555 nm, while the same band of the **2*** ion appears at 560 nm with a broader absorption band at 840 nm, as illustrated in Figure 8c. The absorption features of **1** and the **2*** ion are approximately similar, except that the NIR band of **2*** ion at 840 nm is relatively weaker. The change in UV–vis–NIR absorption during **2** → **2*** conversion was recorded by spectroelectrochemical measurements and is shown in Figure S2b.

The absorption spectra of HL, **1**, and **2** were elucidated by TDDFT calculations in CH₂Cl₂ using the B3LYP functional and are illustrated in Figure 8d–f. The calculated excitation energies (λ/nm), oscillator strengths (f), and transition types are given in Table S2. The gas-phase absorption spectrum of HL was also calculated and is shown in Figure S4. In the gas phase the calculated wavelength (λ_{cal}) of HL is 382.0 nm due to a $\pi \rightarrow \pi^*$ transition, while the experimental wavelength

(λ_{ex}) is 390 nm. In CH₂Cl₂, the calculation suffers from a large solvent shift and the λ_{cal} value is 501.2 nm. Analyses of the frontier molecular orbitals of **1** and **2** affirmed that there is a significant mixing among metal d orbitals and the π orbitals of the ligand. In both experimental and calculated spectra of the complexes the absorption due to an intraligand transition as observed in the free ligand is not distinctly visible. The λ_{cal} value of **2** at 549.3 nm ($f = 0.33$) is due to a HOMO (π_1) → LUMO (π_1^*) excitation that is defined as an intraligand charge transfer (ILCT) transition. The other significant λ_{cal} values due to ILCT transitions are 472.7 (0.04) and 470.6 nm (0.08). Thus, the λ_{ex} values of **1**[−]H⁺ and **2** at 583 and 555 nm, respectively, are assigned to ILCT transitions. The higher energy λ_{cal} values of **2** at 430.6 (0.04), 348.3 (0.02), and 328.2 (0.03) are due to MLCT transitions (see Table S2). Considering the origins of the calculated spectrum of **2**, the λ_{ex} values at 400 nm for **1**[−]H⁺ and 445 and 375 nm for **2** are assigned to MLCT transitions. The calculated spectrum of **2** in CH₂Cl₂ as illustrated in Figure 8f is quite similar to the experimental spectrum.

The significant bands of **1** and **2*** appear at 630 and 560 nm. The origins of these bands were elucidated by TDDFT calculations on **1** in CH₂Cl₂ using the B3LYP and CAM-B3LYP functionals. In this case the results obtained from the B3LYP/DFT method are closer to those obtained experimentally. The calculation implies that the λ_{ex} value of **1** at 630 nm is due to the mixed metal–ligand to ligand charge transfer (MMLCT) and metal to ligand charge transfer (MLCT) transitions. The calculated near-UV MLCT band of **1** spans a range of 500–300 nm, while that of **2** containing a CO ligand is observed at 400–300 nm. Thus, an absorption band of **1** at 400 nm is assigned to an MLCT transition. The NIR transition at 755.0 nm is due to an excitation from β -HOMO-2 to β -LUMO (65%), and it is defined as a metal to mixed metal–ligand charge transfer (MMLCT) transition. Both β -HOMO-2 and β -LUMO scatter dominantly on the ruthenium (see Figure 6) ion, the t_{2g} state of which had undergone rhombic distortion, producing three distinct energy levels. Due to spin–orbit coupling they produce three Kramers doublets, confirmed by EPR spectra (vide supra).²⁶ It is predicted that the rhombic distortion of the t_{2g} state of the ruthenium(III) ion is one of the origins of the NIR transitions of **1** and the **2*** ion. The weaker absorption of **2*** at 840 nm signifies the smaller contribution of the [(L[−])Ru^{III}] resonance form in **2*** ion, as predicted from DFT calculation. It is the effect of a CO ligand that destabilizes the ruthenium(III) form of the **2*** ion.

CONCLUSIONS

The article reports on the proton-coupled redox chemistry of a diarylamine. Proton-coupled redox reactions constitute elementary steps of several biological redox reactions, and in this context the report on a proton-coupled oxidation of a diarylamine to a diarylaminyl radical that correlates with the proton-coupled oxidation of ArOH to ArO[•] is worthy. The diarylamine studied in this case is *N*-(5-nitropyridin-2-yl)quinolin-8-amine (HL), and it was established that the zwitterionic amido (Q-N[−]-PyH⁺) (L[−]H⁺) complex of ruthenium(II) undergoes a proton-coupled oxidation (Q and Py refer to quinoline and 5-nitropyridine fragments, respectively) in air. The redox activities of the zwitterionic complex *trans*-[(L[−]H⁺)Ru^{II}(PPh₃)₂Cl₂] (**1**[−]H⁺) and the corresponding amido analogue *trans*-[(L[−])Ru^{II}(PPh₃)₂(CO)-Cl] (**2**) are remarkably different. The former promotes a

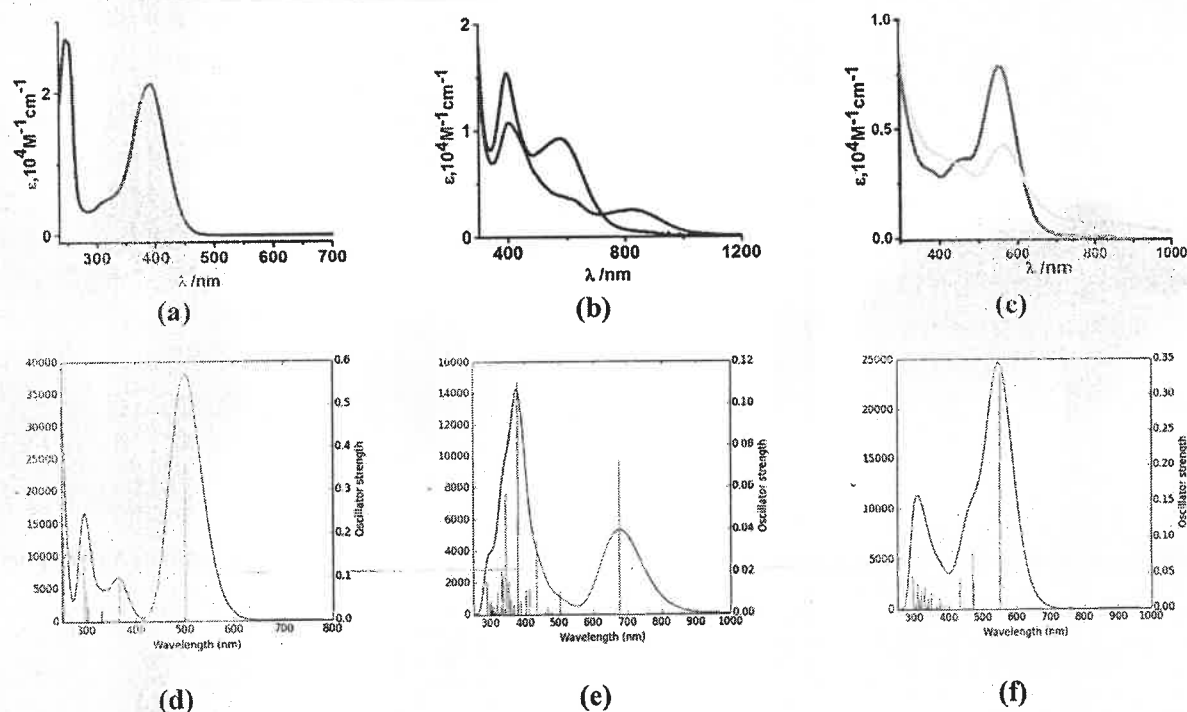


Figure 8. Experimental UV-vis-NIR absorption spectra of (a) HL (b) 1^-H^+ (black) and **1** (blue) (c) **2** (red) and 2^+ (green) in CH_2Cl_2 at 298 K and the calculated spectra of (d) HL (e) **1** and (f) **2** in CH_2Cl_2 using CPCM model.

concerted proton electron transfer (CPET) reaction, yielding *trans*-[(L)Ru(PPh₃)₂Cl₂]-CH₂Cl₂ (**1**-CH₂Cl₂), which has a delocalized ground state of [(L⁻)Ru^{III}] and [(L[•])Ru^{II}] forms, while the amido complex **2** is stable in solution. The potentials of the $1^-H^+/1$ redox couple depend on the electrolytes, and they are respectively -1.57 and -1.40 V in the presence of [N(*n*-Bu)₄]PF₆ and [N(*n*-Bu)₄]Cl. The rate of oxidation of 1^-H^+ also depends on the composition of the medium, and the rate is higher under more basic conditions. Coulometric oxidation of **2** at 0.14 V affords an aminyl radical complex of the type *trans*-[(L[•])Ru^{II}(PPh₃)₂(CO)Cl]⁺ (**2**[•]). The bond parameters of HL, L⁻, and L[•] authenticated by single-crystal X-ray structure determinations and DFT calculations are significantly different. The C_Q-N[•] and C_{Py}-N[•] lengths are relatively longer than the corresponding C_Q-N_{amide} and C_{Py}-N_{amide} lengths. The delocalized ground state of **1** was authenticated by EPR spectroscopy, Mulliken spin density distribution, and UV-vis-NIR absorption spectra. As the coordination chemistry of the aminyl radical is very limited in scope, the study of the proton-coupled oxidation of a coordinated diarylamine furnishing nitrogen-centered radical species is significant in chemical science.

■ ASSOCIATED CONTENT

Supporting Information

The Supporting Information is available free of charge on the ACS Publications website at DOI: 10.1021/acs.inorgchem.8b01401.

Experimental plots of log[absorbance] vs time of oxidation of 1^-H^+ in different solvent mixtures, crystallographic data, TDDFT calculations, and gas-phase optimized and X-ray coordinates (PDF)

Accession Codes

CCDC 1584966–1584969 contain the supplementary crystallographic data for this paper. These data can be obtained free of charge via www.ccdc.cam.ac.uk/data_request/cif, or by emailing data_request@ccdc.cam.ac.uk, or by contacting The Cambridge Crystallographic Data Centre, 12 Union Road, Cambridge CB2 1EZ, UK; fax: +44 1223 336033.

■ AUTHOR INFORMATION

Corresponding Author

*P.G.: e-mail, ghosh@pghosh.in; tel, +91-33-2428-7347; fax, +91-33-2477-3597.

ORCID

Thomas Weyhermüller: 0000-0002-0399-7999

Prasanta Ghosh: 0000-0002-2925-1802

Funding

SERB-DST (EMR/2016/005222) and UGC (F. No. 43-214/2014(SR), New Delhi, India.

Notes

The authors declare no competing financial interest.

■ ACKNOWLEDGMENTS

S.M. thanks the SERB (PDF/2016/001813), New Delhi, India, for fellowships. D.D. is an INSPIRE fellow of the DST, New Delhi, India.

■ ABBREVIATIONS

DFT, density functional theory;; TDDFT, time-dependent DFT; EPR, electron paramagnetic resonance; SOMO, single occupied molecular orbital.

REFERENCES

- (1) Phenoxyl radicals: (a) Ferreira, K. N.; Iverson, T. M.; Maghlaoui, K.; Barber, J.; Iwata, S. Architecture of the Photosynthetic Oxygen-Evolving Center. *Science* 2004, 303, 1831–1838. (b) Whittaker, J. W. Free Radical Catalysis by Galactose Oxidase. *Chem. Rev.* 2003, 103, 2347–2363. (c) Chaudhuri, P.; Wiegardt, K. Phenoxyl Radical Complexes. *Prog. Inorg. Chem.* 2002, 50, 151–216. (d) Wang, Y.; DuBois, J. L.; Hedman, B.; Hodgson, K. O.; Stack, T. D. P. Catalytic galactose oxidase models: biomimetic Cu(II)-phenoxyl-radical reactivity. *Science* 1998, 279, 537–540. (e) Nordlund, P.; Sjöberg, B.-M.; Eklund, H. Three-dimensional structure of the free radical protein of ribonucleotide reductase. *Nature* 1990, 345, 593–598. (f) Altmüller, E. R. The Chemistry of Stable Phenoxy Radicals. *Chem. Rev.* 1967, 67, 475–531.
- (2) Alkyl radicals: (a) Wile, B. M.; Trovitch, R. J.; Bart, S. C.; Tondreau, A. M.; Lobkovsky, E.; Milsman, C.; Bill, E.; Wiegardt, K.; Chirik, P. J. Reduction Chemistry of Aryl- and Alkyl-Substituted Bis(imino)pyridine Iron Dihalide Compounds: Molecular and Electronic Structures of [(PDI)₂Fe] Derivatives. *Inorg. Chem.* 2009, 48, 4190–4200. (b) Banerjee, R. Radical Carbon Skeleton Rearrangements: Catalysis by Coenzyme B₁₂-Dependent Mutases. *Chem. Rev.* 2003, 103, 2083–2094. (c) Cai, S.; Walker, F. A.; Licocchia, S. NMR and EPR Investigations of Iron Corrolates: Iron(III) Corrolate π Cation Radicals or Iron(IV) Corrolates? *Inorg. Chem.* 2000, 39, 3466–3478. (d) Chivers, T.; Eisler, D. J.; Fedorchuk, C.; Schatte, G.; Tuononen, H. M.; Boeré, R. T. Syntheses and Structures of Magnesium and Zinc Boraamidates: EPR and DFT Investigations of Li, Mg, Zn, B, and In Complexes of the [PhB(N^tBu)₂]^{•−} Anion Radical. *Inorg. Chem.* 2006, 45, 2119–2131.
- (3) Kaim, W. Odd Electron on Nitrogen: A Metal-Stabilized Aminyl Radical. *Science* 2005, 307, 216–217.
- (4) Stubbe, J. A.; van der Donk, W. A. Protein Radicals in Enzyme Catalysis. *Chem. Rev.* 1998, 98, 705–762.
- (5) Hicks, R. G. *Stable Radicals: Fundamentals and Applied Aspects of Odd-Electron Compounds*; Wiley: Wiltshire, U.K., 2010.
- (6) (a) Bera, S.; Maity, S.; Weyhermüller, T.; Ghosh, P. Arylamino radical complexes of ruthenium and osmium: dual radical counter in a molecule. *Dalton Trans* 2016, 45, 19428–19440. (b) Kochem, A.; Gellon, G.; Jarjays, O.; Philouze, C.; Leconte, N.; van Gastel, M.; Bill, E.; Thomas, F. A singlet ground state for a cobalt(II)-anilinosalen radical complex. *Chem. Commun.* 2014, 50, 4924–4926. (c) Tsou, C.-C.; Tsai, F.-T.; Chen, H.-Y.; Hsu, L.-J.; Liaw, W.-F. Insight into One-Electron Oxidation of the [Fe(NO)₂]⁹ Dinitrosyl Iron Complex (DNIC): Aminyl Radical Stabilized by [Fe(NO)₂] Motif. *Inorg. Chem.* 2013, 52, 1631–1639. (d) Kochem, A.; Gellon, G.; Leconte, N.; Baptiste, B.; Philouze, C.; Jarjays, O.; Orio, M.; Thomas, F. Stable Aniliny Radical Coordinated to Nickel: X-ray Crystal Structure and Characterization. *Chem. - Eur. J.* 2013, 19, 16707–16721. (e) Mankad, N. P.; Antholine, W. E.; Szilagyi, R. K.; Peters, J. C. Three-Coordinate Copper(I) Amido and Aminyl Radical Complexes. *J. Am. Chem. Soc.* 2009, 131, 3878–3880. (f) Adhikari, D.; Mossin, S.; Basuli, F.; Huffman, J. C.; Szilagyi, R. K.; Meyer, K.; Mindiola, D. J. Structural, Spectroscopic, and Theoretical Elucidation of a Redox-Active Pincer-Type Ancillary Applied in Catalysis. *J. Am. Chem. Soc.* 2008, 130, 3676–3682. (g) Donati, N.; Stein, D.; Büttner, T.; Schönberg, H.; Harmer, J.; Anadaram, S.; Grützmacher, H. Rhodium and Iridium Amino, Amido, and Aminyl Radical Complexes. *Eur. J. Inorg. Chem.* 2008, 2008, 4691–4703. (h) Miyazato, Y.; Wada, T.; Muckerman, J. T.; Fujita, E.; Tanaka, K. Generation of a Ru^{II}-Semiquinone-Anilino-Radical Complex through the Deprotonation of a Ru^{III}-Semiquinone-Anilido Complex. *Angew. Chem.* 2007, 119, 5830–5832. (i) Maire, P.; Königsmann, M.; Sreekanth, A.; Harmer, J.; Schweiger, A.; Grützmacher, H. A Tetracoordinated Rhodium Aminyl Radical Complex. *J. Am. Chem. Soc.* 2006, 128, 6578–6580. (j) Büttner, T.; Geier, J.; Frison, G.; Harmer, J.; Calle, C.; Schweiger, A.; Schönberg, H.; Grützmacher, H. A Stable Aminyl Radical Metal Complex. *Science* 2005, 307, 235–238. (k) Penkert, F. N.; Weyhermüller, T.; Bill, E.; Hildebrandt, P.; Leconte, S.; Wiegardt, K. Anilino Radical Complexes of Cobalt(III) and Manganese(IV) and Comparison with Their Phenoxyl Analogues. *J. Am. Chem. Soc.* 2000, 122, 9663–9673.
- (7) (a) Weinberg, D. R.; Gagliardi, C. J.; Hull, J. F.; Murphy, C. F.; Kent, C. A.; Westlake, B. C.; Paul, A.; Ess, D. H.; McCafferty, D. G.; Meyer, T. J. Proton-Coupled Electron Transfer. *Chem. Rev.* 2012, 112, 4016–4093. (b) Hammes-Schiffer, S. Introduction: Proton-Coupled Electron Transfer. *Chem. Rev.* 2010, 110, 6937–6938. (c) Huynh, M. H. V.; Meyer, T. J. Proton-Coupled Electron Transfer. *Chem. Rev.* 2007, 107, 5004–5064. (d) Mayer, J. M. PROTON-COUPLED ELECTRON TRANSFER: A Reaction Chemist's View. *Annu. Rev. Phys. Chem.* 2004, 55, 363–390.
- (8) Warren, J. J.; Tronic, T. A.; Mayer, J. M. Thermochemistry of Proton-Coupled Electron Transfer Reagents and its Implications. *Chem. Rev.* 2010, 110, 6961–7001.
- (9) Sjödin, M.; Styring, S.; Åkermark, B.; Sun, L.; Hammarström, L. Proton-Coupled Electron Transfer from Tyrosine in a Tyrosine-Ruthenium-tris-Bipyridine Complex: Comparison with Tyrosine Oxidation in Photosystem II. *J. Am. Chem. Soc.* 2000, 122, 3932–3936.
- (10) (a) Sheldrick, G. M. *Acta Crystallogr., Sect. A: Found. Crystallogr.* 2008, 64, 112–122. (b) Sheldrick, G. M. *Acta Crystallogr., Sect. C: Struct. Chem.* 2015, 71, 3–8.
- (11) Neese, F. The ORCA program system. *Wiley Interdiscip. Rev.: Comput. Mol. Sci.* 2012, 2, 73–78.
- (12) (a) Becke, A. D. Density-functional exchange-energy approximation with correct asymptotic behaviour. *Phys. Rev. A: At, Mol, Opt. Phys.* 1988, 38, 3098–3100. (b) Perdew, J. P. Density-functional approximation for the correlation energy of the inhomogeneous electron gas. *Phys. Rev. B: Condens. Matter Mater. Phys.* 1986, 33, 8822–8824.
- (13) (a) Becke, A. D. Density-functional thermochemistry. III. The Role of Exact Exchange. *J. Chem. Phys.* 1993, 98, 5648–5652. (b) Miehlich, B.; Savin, A.; Stoll, H.; Preuss, H. Results Obtained with the Correlation Energy Density Functionals of Becke and Lee, Yang and Parr. *Chem. Phys. Lett.* 1989, 157, 200–206. (c) Lee, C.; Yang, W.; Parr, R. G. Development of the Colle-Salvetti Correlation-Energy Formula into a Functional of the Electron Density. *Phys. Rev. B: Condens. Matter Mater. Phys.* 1988, 37, 785–789.
- (14) (a) Parr, R. G.; Yang, W. *Density Functional Theory of Atoms and Molecules*; Oxford University Press: Oxford, U.K., 1989. (b) Salahub, D. R.; Zerner, M. C. *The Challenge of d and f Electrons*; American Chemical Society: Washington, DC, 1989; ACS Symposium Series 394. (c) Kohn, W.; Sham, L. Self-Consistent Equations Including Exchange and Correlation Effects. *Phys. Rev.* 1965, 140, A1133–1138. (d) Hohenberg, P.; Kohn, W. Inhomogeneous Electron Gas. *Phys. Rev.* 1964, 136, B864–871.
- (15) (a) Weigend, F.; Ahlrichs, R. Balanced basis sets of split valence, triple zeta valence and quadruple zeta valence quality for H to Rn: Design and assessment of accuracy. *Phys. Chem. Chem. Phys.* 2005, 7, 3297–3305. (b) Weigend, F.; Furche, F.; Ahlrichs, R. Gaussian basis sets of quadruple zeta valence quality for atoms H-Kr. *J. Chem. Phys.* 2003, 119 (24), 12753–12762. (c) Eichkorn, K.; Weigend, F.; Treutler, O.; Ahlrichs, R. Auxiliary basis sets for main row atoms and transition metals and their use to approximate Coulomb potentials. *Theor. Chem. Acc.* 1997, 97, 119–124. (d) Schaefer, A.; Huber, C.; Ahlrichs, R. Fully optimized contracted Gaussian basis sets of triple zeta valence quality for atoms Li to Kr. *J. Chem. Phys.* 1994, 100 (8), 5829–5835. (e) Schaefer, A.; Horn, H.; Ahlrichs, R. Fully optimized contracted Gaussian basis sets for atoms Li to Kr. *J. Chem. Phys.* 1992, 97 (4), 2571–2577.
- (16) (a) Weigend, F. A fully direct RI-HF algorithm: Implementation, optimized auxiliary basis sets, demonstration of accuracy and efficiency. *Phys. Chem. Chem. Phys.* 2002, 4, 4285–4291. (b) Weigend, F.; Haser, M.; Patzelt, H.; Ahlrichs, R. RI-MP2: optimized auxiliary basis sets and demonstration of efficiency. *Chem. Phys. Lett.* 1998, 294, 143–152. (c) Feyereisen, M.; Fitzgerald, G.; Komornicki, A. Use of approximate integrals in ab initio theory. An application in MP2 energy calculations. *Chem. Phys. Lett.* 1993, 208, 359–363. (d) Vahtras, O.; Almlöf, J.; Feyereisen, M. W. Integral approximations

for LCAO-SCF calculations. *Chem. Phys. Lett.* **1993**, *213*, 514–518. (e) Mintmire, J. W.; Sabin, J. R.; Trickey, S. B. Local-density-functional methods in two-dimensionally periodic systems. Hydrogen and beryllium monolayers. *Phys. Rev. B: Condens. Matter Mater. Phys.* **1982**, *26*, 1743–1753. (f) Dunlap, B. I.; Connolly, J. W. D.; Sabin, J. R. On some approximations in applications of $X\alpha$ theory. *J. Chem. Phys.* **1979**, *71*, 3396–3402. (g) Whitten, J. L. Coulombic potential energy integrals and approximations. *J. Chem. Phys.* **1973**, *58*, 4496–4501.

(17) Kossmann, S.; Neese, F. Efficient Structure Optimization with Second-Order Many-Body Perturbation Theory: The RIJCOSX-MP2Method. *J. Chem. Theory Comput.* **2010**, *6*, 2325–2338.

(18) Schlegel, H. B.; McDouall, J. J. In *Computational Advances in Organic Chemistry*; Ogretir, C., Csizmadia, I. G., Eds.; Kluwer Academic: Dordrecht, The Netherlands, 1991.

(19) (a) Stratmann, R. E.; Scuseria, G. E.; Frisch, M. An efficient implementation of time-dependent density-functional theory for the calculation of excitation energies of large molecules. *J. Chem. Phys.* **1998**, *109*, 8218–8224. (b) Casida, M. E.; Jamorowski, C.; Casida, K. C.; Salahub, D. R. Molecular excitation energies to high-lying bound states from time-dependent density-functional response theory: Characterization and correction of the time-dependent local density approximation ionization threshold. *J. Chem. Phys.* **1998**, *108*, 4439–4449. (c) Bauernschmitt, R.; Haser, M.; Treutler, O.; Ahlrichs, R. Treatment of electronic excitations within the adiabatic approximation of time dependent density functional theory. *Chem. Phys. Lett.* **1996**, *256*, 454–464.

(20) (a) Cossi, M.; Rega, N.; Scalmani, G.; Barone, V. Energies, structures, and electronic properties of molecules in solution with the C-PCM solvation model. *J. Comput. Chem.* **2003**, *24*, 669–681. (b) Barone, V.; Cossi, M. Quantum Calculation of Molecular Energies and Energy Gradients in Solution by a Conductor Solvent Model. *J. Phys. Chem. A* **1998**, *102*, 1995–2001.

(21) Yanai, T.; Tew, D. P.; Handy, N. C. A new hybrid exchange-correlation functional using the Coulomb-attenuating method (CAM-B3LYP). *Chem. Phys. Lett.* **2004**, *393*, 51–57.

(22) Fielder, S. S.; Osborne, M. C.; Lever, A. B. P.; Pietro, W. J. First-Principles Interpretation of Ligand Electrochemical (E_L) Parameters. Factorization of the σ and π Donor and π Acceptor Capabilities of Ligands. *J. Am. Chem. Soc.* **1995**, *117*, 6990–6993.

(23) Menon, M.; Pramanik, A.; Bag, N.; Chakravorty, A. Chemistry of $[\text{RuL}_2(\text{PPh}_3)_2]^{2+}$ (HL = 8-hydroxyquinoline): Synthesis, Structure, Metal Redox Behaviour and Isomer Selectivity. *J. Chem. Soc., Dalton Trans.* **1995**, *0*, 1417–1422.

(24) (a) Biswas, M. K.; Patra, S. C.; Maity, A. N.; Ke, S. C.; Adhikary, N. D.; Ghosh, P. Electronic Structures of Ruthenium and Osmium Complexes of 9,10-Phenanthrenequinone. *Inorg. Chem.* **2012**, *51*, 6687–6699. (b) Roy, A. S.; Tuononen, H. M.; Rath, S. P.; Ghosh, P. First Ruthenium Complex of Glyoxalbis(N-phenyl)-osazone (LNHPhH₂): Synthesis, X-ray Structure, Spectra, and Density Functional Theory Calculations of (LNHPhH₂)Ru(PPh₃)-2Cl₂. *Inorg. Chem.* **2007**, *46*, 5942–5948.

(25) (a) Kaim, W. Manifestations of Noninnocent Ligand Behavior. *Inorg. Chem.* **2011**, *50*, 9752–9765. (b) Lever, A. B. P. Electronic characteristics of an extensive series of ruthenium complexes with the non-innocent *o*-benzoquinonediimine ligand: A pedagogical approach. *Coord. Chem. Rev.* **2010**, *254*, 1397–1405.

(26) (a) Lahiri, G. K.; Bhattacharya, S.; Mukherjee, M.; Mukherjee, A. K.; Chakravorty, A. Directed Metal Oxidation Levels in Azo-Ruthenium Cyclometalates. Synthesis and Structure of a Trivalent Family. *Inorg. Chem.* **1987**, *26*, 3359–3365. (b) Mahapatra, A. K.; Datta, S.; Goswami, S.; Mukherjee, M.; Mukherjee, A. K.; Chakravorty, A. Ruthenium Complexes of N,S- and C,N,S- Coordinating Azo Ligands: Synthesis, Reactions, and Structure. *Inorg. Chem.* **1986**, *25*, 1715–1721.



Ramakrishna Mission Residential College (Autonomous)
Kolkata 700103, WB, India

Collaborative research in coordination chemistry of organic radicals
Number 14

Institute 1: Ramakrishna Mission Residential College (Autonomous)

Concerned Faculty: Dr. Prasanta Ghosh, Dept of Chemistry

&

Institute 2: Max-Planck-Institut für Chemische Energiekonversion

Stiftstrasse 34 - 36 / D - 45470 Mülheim an der Ruhr

Concerned Scientist: Dr Thomas Weyhermüller

Period of Investigation: 01-06-2019 to 31-12-2019

Project: Metal promoted conversion of aromatic amines

Output: The result was published in a journal of international repute

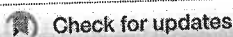
Publication: Metal promoted conversion of aromatic amines to ortho-phenylenediimine derivatives by a radical coupling path

Debarpan Dutta, Suman Kundu, Thomas Weyhermüller and Prasanta Ghosh*

Dalton Trans., 2020, 49, 5015-5019.

Dr. Prasanta Ghosh

Dr Thomas Weyhermüller



Cite this: DOI: 10.1039/d0dt00089b

Received 9th January 2020,
Accepted 17th February 2020

DOI: 10.1039/d0dt00089b

rsc.li/dalton

Metal promoted conversion of aromatic amines to
ortho-phenylenediimine derivatives by a radical
coupling path†Debarpan Dutta,^a Suman Kundu,^a Thomas Weyhermüller^b and Prasanta Ghosh[✉]^a

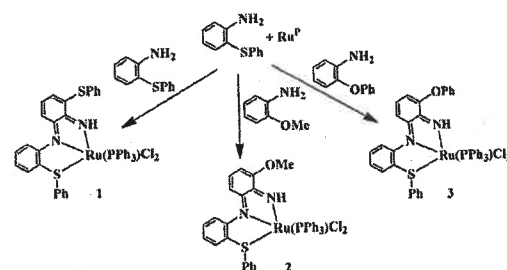
A radical path for the conversion of *o*-substituted arylamines to *o*-phenylenediimine derivatives is reported. In the presence of [Ru^{II}(PPh₃)₃Cl₂] (Ru^P), 2-(phenylthio)aniline (L^{SNH₂}) acts as an *o*-amination agent. Reaction of L^{SNH₂} with Ru^P in toluene promotes (4e + 4H⁺) oxidative dimerization affording an *o*-phenylenediimine complex of ruthenium(II). Similarly, intermolecular coupling between L^{SNH₂} and other arylamines has been achieved.

o-Phenylenediamine derivatives (OPDs) exhibit diverse medicinal^{1a} and anti-corrosion activities.^{1b} OPDs are precursors of bioactive benzimidazole derivatives^{2a} and several functional heterocycles.^{2b} OPDs have been used for constructing conductive polymers^{3a} and fluorescent probes.^{3b} However, the synthetic routes of OPDs are inadequate and they are generally prepared from nitro precursors and routes for the synthesis of OPDs from arylamines reported so far are very limited in scope.⁴ In this work 2-(phenylthio)aniline (L^{SNH₂}) has been established as an *o*-amination agent converting arylamines to OPDs in the presence of a ruthenium precursor with PPh₃ as a coligand.

Organic radicals are numerous,^{5a} but finding a radical unit that promotes a desired reaction is a challenge.^{5b} The oxidation of Ar-NH₂ affords ArNH[•] (anilino radical) and transition metal complexes of ArNH[•] are limited in scope,⁶ while isoelectronic phenoxyl radicals exhibit diverse biological activities.^{7a} The anilino radical is less explored and the significance of the anilino radical in biology has so far not been established.^{7b} In this study, a coordinated arylamino intermediate that promotes a redox cascade⁸ has been detected. The cascade

involves a C-N bond formation reaction generating a functional anilino radical intermediate.

Reaction of 2-(phenylthio)aniline (L^{SNH₂}) with [Ru^{II}(PPh₃)₃Cl₂] (Ru^P) in dry toluene affords a ruthenium(II) complex of L^{SNH₂} of type [Ru^{II}(L^{SNH₂})(PPh₃)₂Cl₂] (1) as shown in Scheme 1, where L^{SNH₂} is an [SNN]-donor OPD. Conversion of L^{SNH₂} to L^{SNH[•]} is a (4e + 4H⁺) oxidative dimerization reaction. Similarly, the reaction of L^{SNH₂} and 2-methoxyaniline (L^{ONH₂}) (1 : 1) with Ru^P produces a L^{SNH[•]} complex of ruthenium(II), [Ru^{II}(L^{SNH[•]})(PPh₃)₂Cl₂] (2), where L^{SNH[•]} is an OPD product of the coupling of L^{SNH₂} and L^{ONH₂} amines. The reaction of L^{SNH₂} and 2-phenoxyaniline (L^{ONH₂}) (1 : 1) with Ru^P affords a ruthenium(II) complex of L^{SNH[•]}, [Ru^{II}(L^{SNH[•]})(PPh₃)₂Cl₂] (3), where L^{SNH[•]} is an OPD product of the intermolecular coupling reaction. 3 was isolated as a co-crystal (3^{co-cryst}·solvent) of 3 (70%) and 1 (30%). It was found that the reaction of L^{SNH₂} with Ru^P in dry toluene in air affords a paramagnetic intermediate, [Ru(L^{SNH[•]})(PPh₃)₂Cl₂] (T_R)₁[•] (Scheme S1†), which is reactive and acts as a template leading to the intermolecular coupling reaction between two arylamines. The paramagnetic intermediate of the reaction of L^{SNH₂} and 2-methoxyaniline (L^{ONH₂}) (1 : 1) with Ru^P is [Ru(L^{ONH[•]})(PPh₃)₂Cl₂] (T_R)₂[•]. In the case of the reaction of L^{SNH₂} and 2-phenoxyaniline (L^{ONH₂}) (1 : 1) with Ru^P, both (T_R)₁[•] and [Ru(L^{ONH[•]})(PPh₃)₂Cl₂] (T_R)₃[•] act as tem-



Scheme 1 Conversions of arylamines to *o*-phenylenediimine derivatives.

^aDepartment of Chemistry, R. K. Mission Residential College, Narendrapur, Kolkata-700103, India. E-mail: ghosh@pghosh.in

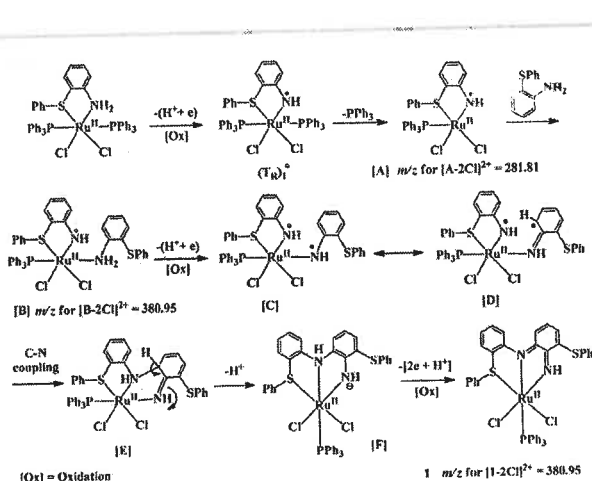
^bMax-Planck-Institut für Chemische Energiekonversion, Stiftstrasse 34-36, 45470 Mülheim an der Ruhr, Germany

† Electronic supplementary information (ESI) available: Experimental section, ESI mass and EPR spectra, mechanistic schemes, bond lengths, calculated and experimental UV-vis-NIR absorption spectra, cyclic voltammogram, frontier MOs, and optimised coordinates. CCDC 1948967–1948969. For ESI and crystallographic data in CIF or other electronic format see DOI: 10.1039/D0DT00089B

Communication

plates producing a co-crystal ($3^{\text{co-cryst}}$) of **3** (major) and **1** (minor). In this article the path of the coupling reactions and the molecular and electronic structures of **1**, **2**, $3^{\text{co-cryst}}$ and $(\text{Tr})_1^+$ – $(\text{Tr})_3^+$ were disclosed.

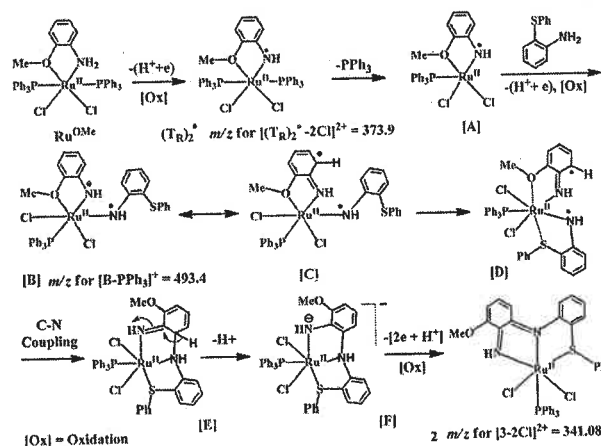
The details of the syntheses are outlined in the Experimental section (ESI†). The reaction of $\text{L}^{\text{SN}}\text{H}_2$ with Ru^{P} in dry toluene in air in the presence of tri-ethylamine (NEt_3) primarily affords a bluish green solution due to the formation of $(\text{Tr})_1^+$. Over time, the solution slowly turned darker ($\lambda_{\text{max}} = 670 \text{ nm}$) and black crystals of diamagnetic **1**-solvent separated out from this solution. The absorbance of the reaction mixture at 670 nm gradually increases with time (Fig. S1(a)†). The EPR spectrum of the solution at 298 K displays a strong signal at $g = 2.060$ due to the coordinated anilino radical with a contribution of the ruthenium(III) ion. The EPR spectra of the solution were recorded at an interval of 10 min until the solution turned dark blue (*vide infra*). $(\text{Tr})_1^+$ is labile and eliminates one of the PPh_3 ligands in solution affording an intermediate [A]. Dissociation of PPh_3 in solution was confirmed by ESI mass spectrometry. The ESI mass spectrum of the bluish solution displays two major m/z peaks respectively at 239 and 281 due to the $[\text{Ru}(\text{NET}_3)\text{Cl}]^+$ and $[(\text{Tr})_1^+ - \text{PPh}_3 - 2\text{Cl}]^{2+}$ ions as shown in Fig. S2a.† In addition to these peaks, the ESI mass spectrum of the darker solution (obtained after one hour of the reaction) exhibits another significant m/z peak at 380 due to the $[\text{Ru}(\text{L}_1^{\text{SNN}}\text{H}^0)(\text{PPh}_3)]^{2+}$ ion corresponding to the intermediates [B]–[F] and **1** (Fig. S2b†). The conversion of $\text{L}^{\text{SN}}\text{H}_2$ to $\text{L}_1^{\text{SNN}}\text{H}^0$ occurs by a $(4e + 4H^+)$ oxidative redox cascade (Scheme 2). The five coordinated intermediate [A] reacts further with another molecule of $\text{L}^{\text{SN}}\text{H}_2$ generating [B]. As expected, the coordinated $-\text{NH}_2$ function undergoes $(H^+ + e)$ oxidation and affords the diradical intermediate [C] that promotes a C–N coupling reaction and generates [E]. To gain aromaticity, [E] undergoes a deprotonation reaction and gives a tridentate amido derivative [F] that further undergoes $(H^+ + 2e)$ oxidation in air affording an $\text{L}_1^{\text{SNN}}\text{H}^0$ complex of ruthenium(II), **1**, in good yield.



Scheme 2 $(4e + 4H^+)$ oxidative dimerization of $\text{L}^{\text{SN}}\text{H}_2$ affording **1**.

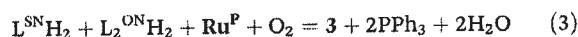
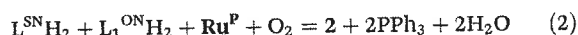
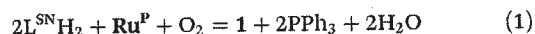
Similarly, the reaction of $\text{L}^{\text{SN}}\text{H}_2$ and $\text{L}_1^{\text{ON}}\text{H}_2$ (1 : 1) with Ru^{P} was analyzed and the absorption spectra of this reaction mixture were different from those obtained for the reaction of $\text{L}^{\text{SN}}\text{H}_2$ and Ru^{P} . In this transformation the radical intermediate is $[\text{Ru}(\text{L}_1^{\text{ON}}\text{H}^+)(\text{PPh}_3)_2\text{Cl}_2] (\text{Tr})_2^+$. In this case the reaction is relatively fast and the solution turns dark pink (λ_{max} , 505 nm, Fig. S1(b)†) immediately, indicating the existence of a different radical analogue. Notably, the EPR spectra of the solution and the frozen glass are different from that of $(\text{Tr})_1^+$ (*vide infra*). In the ESI mass spectrum, significant m/z peaks are observed at 339 and 375 corresponding to the half of the mass of the $[\text{Ru}(\text{L}_2^{\text{SNN}}\text{H}^0)(\text{PPh}_3)]^{2+}$ and $[(\text{Tr})_2^+ - 2\text{Cl}]^{2+}$ ions as shown in Fig. S3.† Also a minor m/z peak at 497 corresponding to the $[\text{Ru}(\text{L}_1^{\text{SNN}}\text{H}^0)]^+$ ion was observed. From the analyses we infer that $(\text{Tr})_2^+$ is the template for this cascade (Scheme 3). The notion was further established by reacting $\text{L}_1^{\text{ON}}\text{H}_2$ with Ru^{P} first and then with $\text{L}^{\text{SN}}\text{H}_2$ producing **2**. The calculated UV-vis absorption spectra of $(\text{Tr})_1^+$ and $(\text{Tr})_2^+$ obtained from the TD DFT calculations in CH_2Cl_2 support the assignment (*vide infra*).

The UV-vis absorption spectra of the reaction mixture of Ru^{P} with $\text{L}^{\text{SN}}\text{H}_2$ and $\text{L}_2^{\text{ON}}\text{H}_2$ (1 : 1) in toluene are relatively broad. In this case, λ_{max} spans a range of 600–680 nm as depicted in Fig. S1(c)†. Analysis by ESI mass spectrometry predicted the presence of both $[\text{Ru}(\text{L}_2^{\text{ON}}\text{H}^+)(\text{PPh}_3)_2\text{Cl}_2] (\text{Tr})_2^+$ and $(\text{Tr})_1^+$ intermediates in the reaction mixture indicating an equal probability of the formation of $(\text{Tr})_3^+$ and $(\text{Tr})_1^+$ from the corresponding amines in the presence of Ru^{P} . The mass spectrum displays m/z peaks at 497, 371, 339, 301 and 273 which are assigned to $[\text{Ru}(\text{L}_1^{\text{SNN}}\text{H}^0)]^+$, $[\text{Ru}(\text{L}_3^{\text{SNN}}\text{H}^0)(\text{PPh}_3)]^{2+}$, $[(\text{Tr})_1^+ - \text{PPh}_3 - \text{Cl}]^+$, $[\text{Ru}(\text{L}^{\text{SN}}\text{H})]^+$ and $[(\text{Tr})_3^+ - \text{PPh}_3 - 2\text{Cl}]^{2+}$ ions, respectively, as shown in Fig. S4.† The analyses strongly suggest the formation of both $\text{L}_1^{\text{SNN}}\text{H}^0$ and $\text{L}_3^{\text{SNN}}\text{H}^0$ diimines. The two reaction paths (Path 1 and Path 2) as proposed are given in Scheme S2.† The co-crystallization of **1** with **3** was confirmed by single crystal X-ray crystallography supporting the proposals



Scheme 3 $(4e + 4H^+)$ oxidative coupling between $\text{L}^{\text{SN}}\text{H}_2$ and $\text{L}_1^{\text{ON}}\text{H}_2$ affording **2**.

in Scheme S2.† The overall reactions of these three conversions are given in eqn (1)–(3).



The success of these reactions depends on the orientation of the non-chelated $\text{L}^{\text{SN}}\text{H}_2$ molecule in the intermediate, [B]. A similar reaction with aniline or *p*-toluidine does not furnish any isolable product justifying the essence of an *ortho* substitution of the incoming arylamine ligand. The interaction of one of the coordinated chloride ligands with the bulkier –SPh, –OMe and –OPh groups orients the phenyl ring obliquely, providing scope for interaction between two anilino radicals favourably as in the intermediate [D] in Scheme 2 and thus making of a C–N bond is successfully achieved. Notably, $\text{L}_1^{\text{SNN}}\text{H}_3$, $\text{L}_2^{\text{SNN}}\text{H}_3$ and $\text{L}_3^{\text{SNN}}\text{H}_3$ are redox noninnocent and exist in three different redox states. $\text{L}_1^{\text{SNN}}\text{H}^0$, $\text{L}_2^{\text{SNN}}\text{H}^0$ and $\text{L}_3^{\text{SNN}}\text{H}^0$ are the *o*-diiminobenzoquinone forms of the corresponding tri-dentate amines as shown in Scheme S3.†

1-solvent crystallizes in the $P\bar{1}$ space group. The molecular geometry of 1-solvent in crystals with the atom-labelling scheme is illustrated in Fig. 1. The solvent molecule in the crystal is severely disordered and removed by SQUEEZE. The electron counting of the void correlates with a CH_2Cl_2 molecule. The Ru–SPh length is 2.369(1) Å. The Ru(1)–N(1) and Ru(1)–N(2) lengths are comparable (Table S2†) and are 1.982(2) and 1.973(2) Å, respectively. The average Ru(1)–Cl length is 2.417(1) Å and Ru(1)–P(1) length is 2.321(1) Å, correlating with those of the ruthenium(II) complexes.⁹ In 1-solvent, the C(1)–N(1) length, 1.315(3) Å, is shorter and correlates well with that of the diiminobenzoquinone form of the *o*-phenylenediamine ligand.^{9,10} Similarly the C(6)–N(2) and C(7)–N(2) lengths, respectively 1.355(3) and 1.416(3) Å, are relatively short and consistent with those of the tridentate di-iminobenzoquinone ligand.¹⁰ Thus 1 is defined as an $\text{L}_1^{\text{SNN}}\text{H}^0$ complex of ruthenium(II).

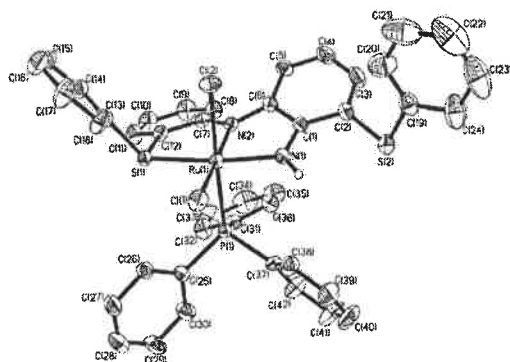


Fig. 1 Molecular geometry of 1-solvent in crystals (50% thermal ellipsoids, solvent molecules and hydrogen atoms are omitted for clarity).

The molecular geometry of 2-H₂O in crystals is shown in Fig. S5.† The Ru–SPh, Ru–N(1) and Ru–N(2) lengths (Table S3†) are similar to those of 1-solvent. The average Ru–Cl and the Ru–P lengths, respectively 2.435 and 2.333(2) Å, are also similar to those of 1-solvent and correlate well with the ruthenium(II) state. The relatively short C(1)–N(1), 1.314(6) Å, C(6)–N(2), 1.371(6) and C(7)–N(2), 1.390(6) Å, lengths strongly suggest the *o*-diiminobenzoquinone form of the ligand.¹⁰

The X-ray diffraction study confirmed that the reaction of Ru^{P} with $\text{L}^{\text{SN}}\text{H}_2$ and $\text{L}_2^{\text{ON}}\text{H}_2$ produces both 1 and 3 which co-crystallize as $3^{\text{cocryst}}\text{-solvent}$. The geometry of $3^{\text{cocryst}}\text{-solvent}$ was refined using a split atom model showing approximately 70% of –OPh and 30% of –SPh fragments. The orientations of the $\text{L}_1^{\text{SNN}}\text{H}^0$ and $\text{L}_3^{\text{SNN}}\text{H}^0$ ligands in the crystals of $3^{\text{cocryst}}\text{-solvent}$ are slightly different (Fig. S6†). The average Ru–Cl and Ru–SPh lengths are 2.422(2) and 2.366(2) Å (Table S4†). The Ru–N(1) and Ru–N(2) lengths corresponding to the –OPh fragment and the Ru–N(1') and Ru–N(2') lengths corresponding to the SPh fragment are similar. Notably, the average of the C(6)–N(2) and C(7)–N(2) lengths is 1.385(9) Å, while that of C(6')–N(2') and C(7')–N(2') is 1.386(12) Å correlating to those of 2-H₂O and 1-solvent.

The EPR spectra of $(\text{T}_\text{R})_1^+$ and $(\text{T}_\text{R})_2^+$ recorded in toluene at 298–115 K are illustrated in Fig. 2. The isotropic EPR spectrum of the blue solution of $(\text{T}_\text{R})_1^+$, obtained after 30 min of the reaction of Ru^{P} and $\text{L}^{\text{SN}}\text{H}_2$ in toluene at 298 K, displays a strong signal at $g = 2.060$ due to an organic radical. The time dependent fluid solution EPR spectra are depicted in Fig. S7(a).† The shift of the g value from those of the pure organic radicals¹¹ is an indicator of the contribution of the ruthenium(III) ion¹² to the ground electronic state of $(\text{T}_\text{R})_1^+$ (Scheme S4†). The anisotropic frozen glass spectrum exhibits hyperfine splitting due to

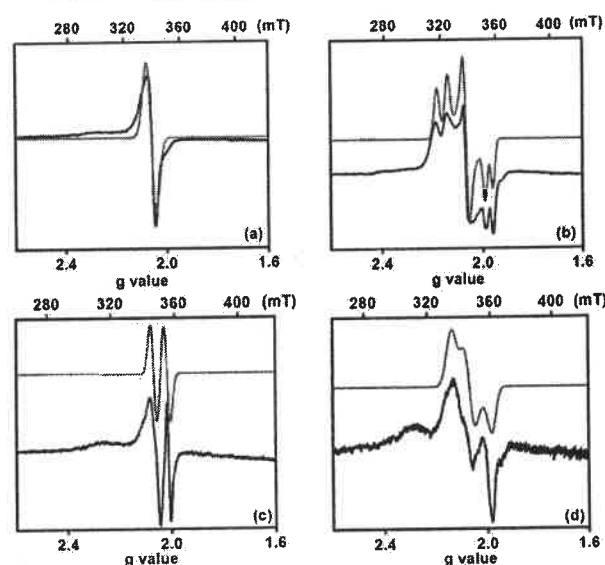


Fig. 2 X-band EPR spectra of $(\text{T}_\text{R})_1^+$: (a) fluid solution (298 K) and (b) frozen glass (115 K); $(\text{T}_\text{R})_2^+$: (c) fluid solution (298 K) and (d) frozen glass (115 K) in toluene (black, experimental; red, simulated).

Communication

the ^{31}P ($I = 1/2$) nucleus and it was simulated with $g_1 = 2.161$ ($A_P = 180$), $g_2 = 2.066$ and $g_3 = 1.976$ ($A_P = 145$ MHz). The g values ($g_{\text{avg}} = 2.067$) and the larger anisotropy ($\Delta g = 0.18$) predict that both $[\text{Ru}^{\text{II}}(\text{L}^{\text{SNNH}})] \leftrightarrow [\text{Ru}^{\text{III}}(\text{L}^{\text{SNNH}})]$ forms contribute to the ground electronic state of $(\text{T}_\text{R})_1^*$ which is stabilized in solution for further reaction making a C–N bond.

The isotropic EPR spectrum of the pink solution of $(\text{T}_\text{R})_2^*$, obtained after 30 min of the reaction of Ru^{P} and $\text{L}_1^{\text{ONH}_2}$ and L^{SNNH_2} (1 : 1) in toluene at 298 K, displays a strong hyperfine signal due to the ^{31}P nucleus (Fig. 2 and Fig. S7(b)†). The simulated g value is $g = 2.040$ with A_P , 245 MHz. In this case, the g value is less deviated from those of organic radicals, predicting a larger contribution of the anilino radical in the fluid solution of $(\text{T}_\text{R})_2^*$. The simulated g values of the frozen glass spectrum at 115 K are $g_1 = 2.140$, $g_2 = 2.068$ and $g_3 = 1.981$ ($g_{\text{avg}} = 2.063$), showing the contribution of both $[\text{Ru}^{\text{II}}(\text{L}_1^{\text{ONH}})] \leftrightarrow [\text{Ru}^{\text{III}}(\text{L}_1^{\text{ONH}})]$ forms to the ground electronic state of $(\text{T}_\text{R})_2^*$.

The isotropic EPR spectrum of the brownish solution obtained from a reaction of Ru^{P} with $\text{L}_2^{\text{ONH}_2}$ and L^{SNNH_2} (1 : 1) in toluene at 298 K displays a strong signal at $g = 2.066$ (Fig. S7(c) and S8†). The frozen glass spectrum at 113 K is relatively broad and the experimental g values ($g_1 = 2.144$, $g_2 = 2.058$, $g_3 = 1.987$ and $g_{\text{avg}} = 2.063$) compare well with those of $(\text{T}_\text{R})_1^*$, exhibiting a different hyperfine pattern. ESI mass spectrometry and X-ray crystallography predicted that both $(\text{T}_\text{R})_1^*$ and $(\text{T}_\text{R})_3^*$ radicals were generated in this reaction and the spectrum was not simulated.

In cyclic voltammetry both $[\text{Ru}^{\text{II}}(\text{L}^{\text{SNNH}})]/[\text{Ru}^{\text{III}}(\text{L}^{\text{SNNH}})]$ and $[\text{Ru}^{\text{II}}(\text{L}^{\text{SNNH}})]/[\text{Ru}^{\text{III}}(\text{L}^{\text{SNNH}})]$ redox couples of **1**, **2** and **3**^{co-cryst} are irreversible (Fig. S9 and Table S5†), indicating that the monoanionic $\text{L}_1^{\text{SNNH}}^-$, $\text{L}_2^{\text{SNNH}}^-$ and $\text{L}_3^{\text{SNNH}}^-$ and the dianionic complexes are not stable and $[1-3]^-$ and $[1-3]^{2-}$ are not isolable.

The UV-vis-NIR absorption spectra of **1**, **2** and **3**^{co-cryst} were recorded in CH_2Cl_2 at 298 K and are illustrated in Fig. S10†. The absorption spectra of **1–3** are notably different from those of the $(\text{T}_\text{R})_1^*$, $(\text{T}_\text{R})_2^*$ and $(\text{T}_\text{R})_3^*$ intermediates (Fig. S11†). **1** exhibits a strong absorption band at 560 nm and a weaker NIR band at 950 nm (Table S6†). Similarly the spectrum of **2** displays bands at 535 and 920 nm, whereas the absorption bands of **3**^{co-cryst} appear at 550 and 970 nm. Metal (d_{Ru}) to ligand (quinone form) charge transfer (MLCT) transitions have been assigned to the origin of the NIR bands of **1–3**^{co-cryst}.

The absorption spectra of **1**, $(\text{T}_\text{R})_1^*$ and $(\text{T}_\text{R})_2^*$ were further analyzed by TD DFT calculations using the ORCA program package.¹³ The geometry of **1** with the singlet spin state in CH_2Cl_2 using the CPCM model was optimized by the hybrid PBE0 DFT method. There is a significant mixing between d_{Ru} and π^* orbitals and the contribution of d_{Ru} to the HOMO and LUMO as illustrated in Fig. S11† supports the notion. The calculated spectrum (Fig. S12†) is similar to the experimental spectrum of **1** (Fig. S10†). The lower energy transition at $\lambda_{\text{exp}} = 950$ nm is assigned to the HOMO \rightarrow LUMO transition and the corresponding calculated wavelengths (λ_{cal}) are 1056.9 and 988 nm. All these transitions are assigned to mixed-metal–ligand to mixed-metal–ligand charge transfer transitions. The

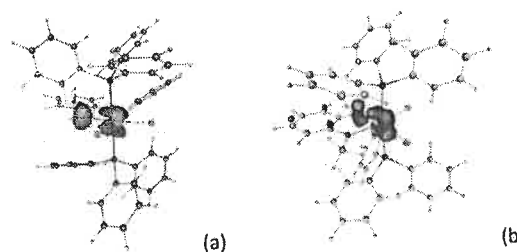


Fig. 3 Mulliken spin density plots of (a) $(\text{T}_\text{R})_1^*$ and (b) $(\text{T}_\text{R})_2^*$ with an isovalue of 0.01.

molecular geometries of $(\text{T}_\text{R})_1^*$ and $(\text{T}_\text{R})_2^*$ were optimized in CH_2Cl_2 with a doublet spin and the calculated significant bond parameters are summarized in Table S7.† Notably in these paramagnetic intermediates the spin scatters on both ruthenium and nitrogen atoms (Fig. 3). In the case of $(\text{T}_\text{R})_1^*$, 50.2% of the Mulliken spin is localized on the ruthenium ion and 34% of the spin is localized on the nitrogen atom. Similarly, in $(\text{T}_\text{R})_2^*$ the Mulliken spin disperses both on ruthenium (53.3%) and nitrogen (31.4%). The delocalization of the spin on both metal and ligand fragments is consistent with the higher EPR g parameters (2.060 for $(\text{T}_\text{R})_1^*$ and 2.040 for $(\text{T}_\text{R})_2^*$) in comparison to that of organic free radicals.¹¹ The calculated UV-vis absorption spectra of $(\text{T}_\text{R})_1^*$ and $(\text{T}_\text{R})_2^*$ in CH_2Cl_2 are shown in Fig. S13.† Notably, both calculated and experimental λ_{max} of $(\text{T}_\text{R})_2^*$ are blue shifted in comparison to those of $(\text{T}_\text{R})_1^*$. The λ_{cal} of $(\text{T}_\text{R})_1^*$, 603.6 nm, correlates well with the λ_{exp} value, 670 nm, while the λ_{cal} of $(\text{T}_\text{R})_2^*$ is 532.3 and the corresponding λ_{exp} is 505 nm (Table S8 and Fig. S14†). The similar features of the calculated and experimental spectra confirm the existence of $(\text{T}_\text{R})_1^*$ and $(\text{T}_\text{R})_2^*$ as reactive intermediates in solution for the conversions of $2\text{L}^{\text{SNNH}_2} \rightarrow \text{L}_1^{\text{SNNH}^0}$ and $(\text{L}_1^{\text{ONH}_2} + \text{L}^{\text{SNNH}_2}) \rightarrow \text{L}_2^{\text{SNNH}^0}$.

In conclusion, a ruthenium(II) precursor promoted transformation of *o*-substituted arylamines to *o*-phenylenediimine derivatives (OPDs) by a C–N radical coupling reaction is reported. The conversion occurs by a multistep redox cascade, where 2-(phenylthio)aniline (L^{SNNH_2}) acts as an *o*-amination agent. The $(4e + 4H^+)$ oxidative dimerization of L^{SNNH_2} and the intermolecular couplings between L^{SNNH_2} and 2-methoxyaniline and also L^{SNNH_2} and 2-phenoxyaniline producing the ruthenium complexes of the diimines provide scope for using arylamines as precursors to model OPDs.

Conflicts of interest

There are no conflicts to declare.

Acknowledgements

Financial support received from SERB-DST (EMR/2016/005222), New Delhi, India is gratefully acknowledged. DD is an INSPIRE fellow of DST (IF131158).

Notes and references

- 1 (a) H. D. Brown, A. R. Matzuk, I. R. Ilves, L. H. Peterson, S. A. Harris, L. H. Sarett, J. R. Egerton, J. J. Yakstis, W. C. Campbell and A. C. Cuckler, *J. Am. Chem. Soc.*, 1961, **83**, 1764–1765; (b) M. A. Malik, M. A. Hashim, F. Nabi, S. A. Al-Thabaiti and Z. Khan, *Int. J. Electrochem. Sci.*, 2011, **6**, 1927–1948.
- 2 (a) P. A. Milton and T. L. Brown, *J. Am. Chem. Soc.*, 1977, **99**, 1390; (b) W. Wang, Y. Shen, X. Meng, M. Zhao, Y. Chen and B. Chen, *Org. Lett.*, 2011, **13**, 4514–4517.
- 3 (a) X. Sun, S. Dong and E. Wang, *Chem. Commun.*, 2004, 1182; (b) M. J. Plater, I. Greig, M. H. Helfrich and S. H. Ralston, *J. Chem. Soc., Perkin Trans. 1*, 2001, 2553–2559.
- 4 (a) S. Mandal, S. Samanta, T. K. Mondal and S. Goswami, *Organometallics*, 2012, **31**, 5282–5293; (b) S. Samanta and S. Goswami, *J. Am. Chem. Soc.*, 2009, **131**, 924–925.
- 5 (a) S. Kumar, Y. Kumar, S. K. Keshri and P. Mukhopadhyay, *Magnetochemistry*, 2016, **2**, 42; (b) T. Storr and R. Mukherjee, *Inorg. Chem.*, 2018, **57**(16), 9577–9579.
- 6 (a) S. Kundu, D. Dutta, S. Maity, T. Weyhermüller and P. Ghosh, *Inorg. Chem.*, 2018, **57**, 11948–11960; (b) A. Kochem, G. Gellon, N. Leconte, B. Baptiste, C. Philouze, O. Jarjayes, M. Orio and F. Thomas, *Chem. – Eur. J.*, 2013, **19**, 16707–16721.
- 7 (a) P. Chaudhuri and K. Wieghardt, *Prog. Inorg. Chem.*, 2001, **50**, 151; (b) W. Kaim, *Science*, 2005, **307**, 216–217.
- 8 (a) S. Mondal, S. Bera and P. Ghosh, *J. Org. Chem.*, 2019, **84**, 1871–1881; (b) S. Mondal, S. Bera, S. Maity and P. Ghosh, *Inorg. Chem.*, 2017, **56**, 13194–13204; (c) S. Mondal, S. Maity and P. Ghosh, *Inorg. Chem.*, 2017, **56**, 8878–8888.
- 9 (a) S. C. Patra, T. Weyhermüller and P. Ghosh, *Inorg. Chem.*, 2014, **53**, 2427–2440; (b) M. K. Biswas, S. C. Patra, A. N. Maity, S. Ke, N. D. Adhikary and P. Ghosh, *Inorg. Chem.*, 2012, **51**, 6687–6699; (c) A. S. Roy, H. M. Tuononen, S. P. Rath and P. Ghosh, *Inorg. Chem.*, 2007, **46**, 5942–5948.
- 10 (a) K. Chłopek, E. Bill, T. Weyhermüller and K. Wieghardt, *Inorg. Chem.*, 2005, **44**, 7087–7098; (b) M. Bubrin, D. Schweinfurth, F. Ehret, S. Zális, H. Kvapilová, J. Fiedler, Q. Zeng, F. Hartl and W. Kaim, *Organometallics*, 2014, **33**, 4973.
- 11 R. G. Hicks, *Stable Radicals: Fundamentals and Applied Aspects of Odd-Electron Compounds*, John Wiley & Sons, Wiltshire, UK, 2010.
- 12 S. Maity, S. Kundu, A. S. Roy, T. Weyhermüller and P. Ghosh, *Inorg. Chem.*, 2015, **54**, 1384–1394.
- 13 F. Neese, *Wiley Interdiscip. Rev.: Comput. Mol. Sci.*, 2012, **2**, 73–78.



Ramakrishna Mission Residential College (Autonomous)
Kolkata 700103, WB, India

Collaborative research in coordination chemistry of organic radicals
Number 15

Institute 1: Ramakrishna Mission Residential College (Autonomous)

Concerned Faculty: Dr. Prasanta Ghosh, Dept of Chemistry
&

Institute 2: Max-Planck-Institut für Chemische Energiekonversion

Stiftstrasse 34 - 36 / D - 45470 Mülheim an der Ruhr

Concerned Scientist: Dr Thomas Weyhermüller

Period of Investigation: 01-12-2019 to 31-5-2020

Project: Coordination polymers of Ag(I) and Hg(I) ions with redox non-innocent ligands

Output: The result was published in a journal of international repute

Publication: Coordination polymers of Ag(I) and Hg(I) ions with 2,2'-azobispyridine: synthesis, characterization and enhancement of conductivity in the presence of Cu(II) ions

Suvendu Maity, Kaushik Naskar, Tanmay Bhowmik, Amalendu Bera, Thomas Weyhermüller, Chittaranjan Sinha and Prasanta Ghosh*
Dalton Trans., 2020, 49, 8438-8442.

Dr. Prasanta Ghosh

Dr Thomas Weyhermüller

COMMUNICATION



Cite this: *Dalton Trans.*, 2020, 49, 8438

Received 21st April 2020,
Accepted 2nd June 2020

DOI: 10.1039/d0dt01470b
rsc.li/dalton

Coordination polymers of Ag(I) and Hg(I) ions with 2,2'-azobispyridine: synthesis, characterization and enhancement of conductivity in the presence of Cu(II) ions†

Suvendu Maity,^{a,b} Kaushik Naskar,^b Tanmay Bhowmik,^a Amalendu Bera,^c Thomas Weyhermüller,^d Chittaranjan Sinha^b and Prasanta Ghosh^{*,a}

The cationic coordination polymers (CPs) of the types $[\text{Hg}_2(\text{abpy})_2]_n[\text{PF}_6]_{2n}$ (1) and $[\text{Ag}(\text{abpy})]_n[\text{PF}_6]_n$ (2) (abpy = 2,2'-azobispyridine) were synthesized and characterized. Experimentation using the crystals confirmed that 1 and 2 are conductors of electricity. The relative conductivity of 1 is 62 times greater than that of 2. The conductivity of 1 increases 70 fold when it reacts with Cu^{2+} ions.

The design and synthesis of long chain metal organic coordination polymers (CPs) have been a subject of modern research. During the last decades, in supra-molecular coordination chemistry and crystal engineering, their utilities and applications were widely explored.^{1–10} Due to their different structural features and topologies, CPs can exhibit a wide range of interesting physical and chemical behaviour. The cationic CPs bind anions through non-covalent interactions and the conformation and helicity of the polymer structure are controlled by the shape and size of the anions. Another important advantage of the cationic CPs is mainly the separation of higher molecular weight anions (like AsO_4 , PO_4 and other radioactive anion species, etc.) from solutions.^{11–16} Common examples of salts used for this purpose are NaPF_6 , NaBF_4 etc. Anion binding typically involves supra-molecular interactions, such as hydrogen bonding, electrostatic, $\pi \cdots \pi$ stacking, cation $\cdots\pi$, C–H $\cdots\pi$, non-covalent attractive force among anions and π -acidic (or electron-deficient) charge-neutral aromatic rings, namely, the anion- π interaction. These features have become a topic of interest in the field of crystal engineering for their wide applications in constructing molecular assemblies, new

types of materials and medicinal chemistry. Depending upon these interactions, various types of physical properties can be developed upon aggregation in supra molecular chemistry.^{17–20} The 1D/2D coordination chain or layer can be extended to 2D or 3D coordination polymers towards emphasizing structural variation, topologies, dimensionalities and novel properties. The important properties, mainly dimensionality, pore size and surface area, of these complexes could be modulated just by changing the linker size, geometry and functionalities.

2,2'-Azobispyridine (abpy) acts as a bridging ligand involving the azo group $-\text{N}=\text{N}-$ as the coordinating π acceptor functional group and it can form dinuclear complexes with unusual electronic and structural features.^{21–24} Particularly, abpy can bind in different modes with the transition metal ion, especially exhibiting self and cross binding modes. The coordination polymer of $[\text{Cu}(\text{abpy})]_n$ generated upon the chemical reduction of $[\text{Cu}(\text{abpy})\text{PF}_6]_n$ was used for the transformation of NO_2 gas to NO .²⁵ The abpy group is easily reduced to a radical bridging ligand and this property makes possible the reduction of the 1D coordination polymer $[\text{Cu}(\text{abpy})\text{PF}_6]_n$ to $[\text{Cu}(\text{abpy})]_n$, which is more conductive and porous in nature.²⁶ It was reported that the dinuclear $[\text{Cu}_2(\text{abpy})(\text{CH}_3\text{CN})_8][\text{BF}_4]_4$ complex decomposes to the Cu^{I} polymer $\{[\text{Cu}(\text{abpy})][\text{BF}_4]_2\}_n$.²⁷ Recently, we have reported that the reaction of $[\text{Cu}^{\text{II}}(\text{abpy})_3][\text{PF}_6]_2$ and $[\text{Cu}^{\text{II}}(\text{abpy})_2(\text{bpy})][\text{PF}_6]_2$ with catechol, *o*-aminophenol, *p*-phenylenediamine and diphenylamine (Ph–NH–Ph) in a 2:1 molar ratio affords $[\text{Cu}^{\text{I}}(\text{abpy})_2]^+$ and the corresponding quinone derivatives.²⁸ So the activities of the copper containing abpy ligand are important in synthetic and materials chemistry.

The copper containing MOF $\{[\text{Cu}_2(6\text{-Hmna})(6\text{-mn})]\cdot\text{NH}_4\}_n$ (6-Hmna = 6-mercaptonicotinic acid, 6-mn = 6-mercaptonicotinate) of a 2D $(-\text{Cu}-\text{S}-)_n$ motif was isolated *in situ* from an S–S bond cleavage reaction under hydrothermal conditions. The complex is found to have a low activation energy (6 meV), a small band gap (1.34 eV) and the highest electrical conductivity (10.96 S cm^{-1}) among the reported MOFs measured using single crystals.²⁹ The $[\text{Cd}_2(2,2\text{-DSB})_2(\text{INH})_2(\text{H}_2\text{O})_2]_n$ MOF

^aDepartment of Chemistry, R. K. Mission Residential College, Kolkata 700103, India.
E-mail: ghosh@pghosh.in

^bDepartment of Chemistry, Jadavpur University, Kolkata 700032, India

^cDepartment of Electronics, R. K. Mission Residential College, Kolkata 700103, India

^dMax-Planck-Institut für Chemische Energiekonversion, Stiftstrasse 34-36,
D-45470 Mülheim an der Ruhr, Germany

†Electronic supplementary information (ESI) available. CCDC 1993894 and 1993895. For ESI and crystallographic data in CIF or other electronic format see DOI: 10.1039/D0DT01470B

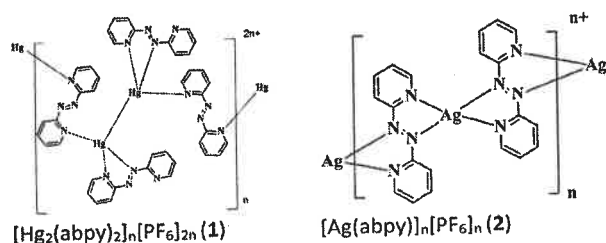


Chart 1 Binding modes of abpy ligand and the isolated coordination polymers of Hg(II) and Ag(I) ions.

showed a high order of electrical conductivity ($1.05 \times 10^{-3} \text{ S m}^{-1}$) and also exhibited the potential to be ~ 2.75 times more photosensitive from the dark to light phase.³⁰ In this search, the $[\text{Hg}_2(\text{abpy})_2]_n^{2n+}$ (1^{2n+}) and $[\text{Ag}(\text{abpy})]_n^{n+}$ (2^{n+}) complexes were isolated with the heavy metal Hg^{2+} and Ag^+ ions and their cationic polymeric configuration were established by single crystal X-ray structure determinations. In these complexes, the abpy ligand binds in η^1 and η^2 modes with two metal ions using N_{azo} and $\text{N}_{\text{pyridine}}$ donor sites. The isolated complexes are shown in Chart 1. The X-ray structure determinations confirmed that 1 contains both η^1 and η^2 binding modes while 2 reveals only the η^2 binding mode. Both 1 and 2 exhibit electrical conductivity in the solid state. In 1, one of the NN-chelating sides remains free and can chelate other transition metal ions. The electrical conductivity of 1 increases enormously, particularly in the presence of copper(II) ions.

1 was isolated from a reaction of $\text{Hg}_2(\text{NO}_3)_2$ with abpy in a 1:2 ratio in a mixture of MeOH and CH_3CN solvents. Similarly, 2 was prepared by the reaction of AgNO_3 and abpy in a 1:1 ratio. In both cases, the cationic coordination polymers were crystallized using NaPF_6 .

The X-ray crystal structures show that in 1 both the η^2 -NN and η^1 -N binding modes of the abpy ligand are present while in 2 only the η^2 -NN binding mode exists. In these crystals, many supramolecular interactions like $\pi \cdots \pi$ stacking, anion $\cdots\pi$, C-H $\cdots\pi$, and M \cdots F interactions are present. These coordination polymers are built through the combination of metal-coordination, anion-hydrogen bonding, and π - π stacking interactions that play an important role in conductivity.

The abpy ligand acts as the linker ligands in these CPs. 1 crystallizes in the $P2_1/n$ space group. Despite this, the gross structure has shown that the complex is an infinite helical coordination polymer with one Hg ion with the two ligands. Each Hg ion is tetrahedrally surrounded by the N_{azo} of one ligand, $\text{N}_{\text{pyridine}}$ of another ligand and Hg atom forming a Hg-Hg bond (Fig. 1(a)). The Hg-Hg bond length is 2.5313(3) Å. The Hg(1) ions are coordinated by two $\text{N}_{\text{pyridine}}$ units and Hg(1)-N(21) and Hg(1)-N(51) distances are respectively, 2.517(2) and 2.430(2) Å. One N_{azo} coordinates with Hg(1) and the Hg(1)-N(28) distance is 2.385(2) Å.

The $\text{N}=\text{N}$ azo bond length for the η^2 -NN-coordination, N(7)-N(8) and N(27)-N(28), are 1.254(3) and 1.249(3) Å, respectively, whereas in the η^1 -N-coordination, N(47)-N(47A) is 1.261(4) Å. The special feature of this crystal is a right handed

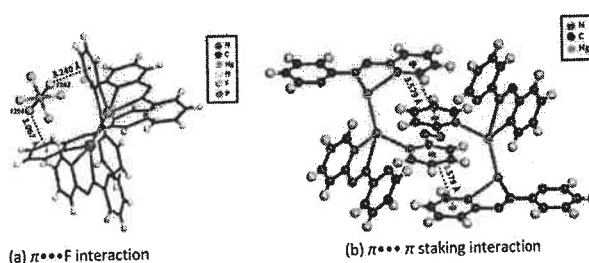


Fig. 1 (a) $\pi \cdots \text{F}$ and (b) $\pi \cdots \pi$ staking interactions constructing the 1D polymer.

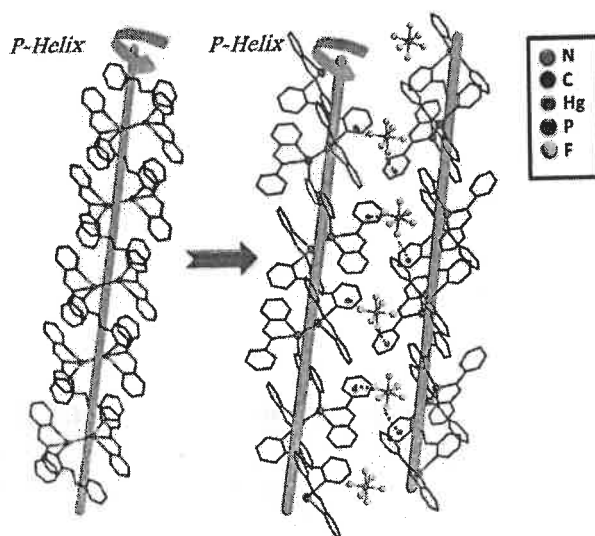


Fig. 2 Helical aspect of 1, viewed along the ab -plane side view of 1D chain, a P /right handed along the b -axis and the two helical stands present through the $\pi \cdots \text{F}$ interactions.

helical rearrangement of the metal ligand framework. The $\pi \cdots \text{F}$ interactions with the PF_6^- unit and π aromatic rings are shown in the Fig. 1(a). The distances between the $\pi \cdots \text{F}$ interactions are 3.067 and 3.240 Å. In 1, there is also $\pi \cdots \pi$ stacking interaction observed in the crystal structure. The distance of the $\pi \cdots \pi$ stacking interaction is 3.579 Å (Fig. 1(b)). The helical structure is observed in the case of 1, viewed along the ab -plane side view of 1D chain, a P /right handed along the b -axis and the two helical stands present through $\pi \cdots \text{F}$ interactions (Fig. 2). The arrangement of the CP of 1 and PF_6^- ions along a -axis is shown in Fig. S1.†

2 crystallizes in the $Pnna$ space group. The structural pattern in the crystals of 1 is completely different from that of 2. In the crystal structure of 2, several types of interactions are present and notable interactions are nonbonded $\pi \cdots \text{F}$, $\pi \cdots \pi$ staking, H \cdots F and Ag \cdots F interactions. The distance between two $\pi \cdots \pi$ stacked aromatic rings (considering centroids) is 3.652 Å (Fig. 3(a)). The interaction distance for the aromatic $\pi \cdots \text{F}$ is 3.073 Å and it is a stronger interaction than that in 1. The H \cdots F interaction is shown in Fig. 3(c). In complex 2, Ag \cdots F

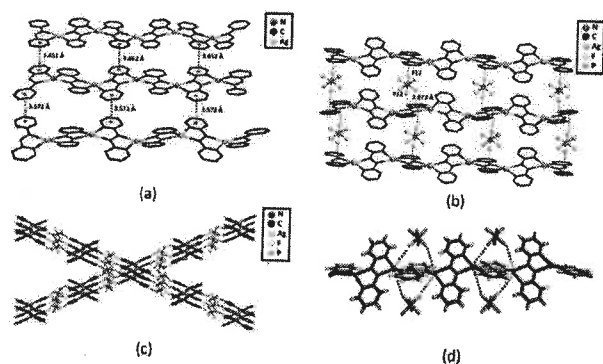


Fig. 3 (a) $\pi\cdots\pi$ stacking interaction along the c -axis, (b) $\pi\cdots\text{F}$ interaction along the c -axis, (c) $\text{H}\cdots\text{F}$ interaction along the a -axis and (d) $\text{Ag}\cdots\text{F}$ interaction along the c -axis in the coordination polymer of 2.

interaction is also present where the PF_6^- unit interacts with two silver ions (Fig. 3(d)).

The optical properties of the complexes were measured by UV-vis absorption spectroscopy in CH_2Cl_2 . Fig. S2† represents the normalized absorption spectra in the range of 300–800 nm. The λ_{max} of 1 and 2, respectively, are 343 nm and 336 nm. The optical bandgap energies of 1 and 2 have been determined by Tauc's equation.³¹

$$(\alpha h\nu) = A(h\nu - E_g)^n \quad (1)$$

where α is the absorption coefficient, E_g is the band gap energy, h is Planck's constant, ν is the frequency of light, and the exponent n is the electron transition processes dependent constant, for direct transition $n = 1/2$.³¹ A is a constant which is considered from the $(\alpha h\nu)^2$ vs. $h\nu$ plot of the synthesized compounds are portrayed in Fig. 4. By extrapolating the linear region of both the plots $(\alpha h\nu)^2$ vs. $h\nu$, the values of direct optical band gap energy for 1 and 2 were evaluated as 3.14 eV and 3.41 eV, respectively.

The phase purity of both samples was confirmed by PXRD and all of the major peaks of the PXRD patterns of the as-synthesized 1 and 2 match quite well with those simulated from single crystal data indicating the phase purity of the bulk compounds (Fig. S4†).

Current–voltage (I – V) measurements were performed using the crystals of 1 and 2. The current–voltage plots of 1 and 2 follow Ohm's law and the representative plots are shown in

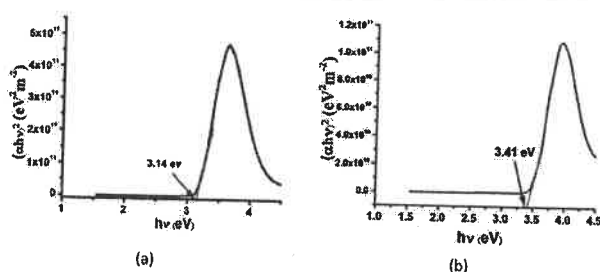


Fig. 4 Tauc's plots of (a) 1 and (b) 2.

Fig. S5(a) and (b)†, respectively, and data are given in Table S2.† 1 shows exceptionally higher electrical conductivity (320 S cm^{-1}) while the electrical conductivity of 2 is relatively lower, (5.1 S cm^{-1}) 62 times lower than that of 1.

Clayman *et al.* reported the porous polymer $[\text{Cu}(\text{abpy})]_n$ that exhibits conductivities approaching to 0.11 S cm^{-1} at room temperature.²⁶ 1 containing one free NN chelation site opens up the opportunity to investigate the effect on the electrical conductivity in the presence of copper(II) ions. Due to the interaction of the metal ion, the change of bandgap was estimated by UV-vis spectroscopy. In the presence of Cu^{2+} ions, the λ_{max} at 332 nm red shifted to 349 nm and the spectral change is shown in Fig. S3.† From this study, it is clear that the Hg CPs can be used for doping with Cu^{2+} ions for the conductivity study. Upon the treatment of 1 with $\text{Cu}(\text{acac})_2$ solution (1 : 1 mole ratio) for 24 h, the orange crystals of 1 turned deep brown. The conductivity of the new material was measured. The contact area was determined using the Hertzian elastic contact model. The conductivity of Hg@Cu is $2.34 \times 10^4 \text{ S cm}^{-1}$ (Fig. 5(a)). Surprisingly, the conductivity of the Hg@Cu compound is higher than that of pure 1. In the reaction of copper ions with 1 there are two possibilities, either trans-metalation where the mercurous ions are completely replaced by copper ions and the other is the incorporation of copper ions in 1. However, it has not been analyzed unambiguously. The incorporation of Cu^{2+} ions has been confirmed by the EPR spectrum (Fig. 5(b)) due to the presence of signals for the Cu^{2+} ions ($g = 2.2$).

The surface morphology of 1 and Hg@Cu was analyzed through SEM images. The SEM images of both 1 and Hg@Cu are shown in Fig. 6(a) and (b). It is clear that after addition of

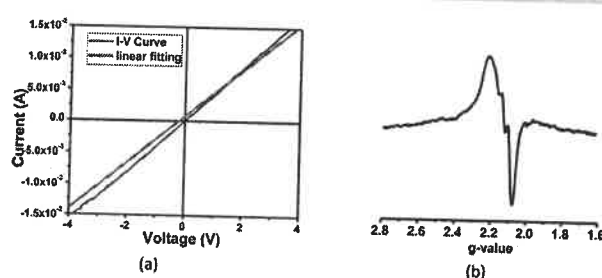


Fig. 5 (a) Current–voltage curves and (b) X-band EPR spectrum of Hg@Cu.

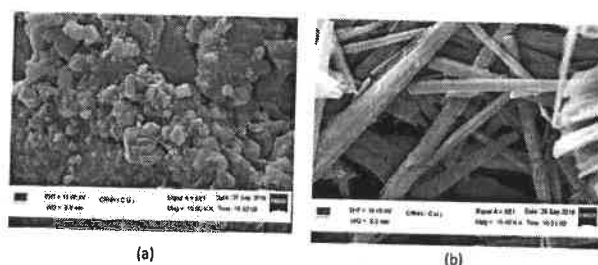


Fig. 6 The SEM images of (a) 1 and (b) Hg@Cu.

the Cu(II) solution, the surface morphology changes from an aggregated to hierarchical fibre structure. The elemental composition was confirmed through EDS measurement. It affirms that the compound **Hg@Cu** consists of Hg and Cu (Fig. S6†) resulting in the higher conductivity of the material than that of the original complex **1**.

Conclusion

Cationic conductive polymers (CP) of the types $[\text{Hg}_2(\text{abpy})_2]_n[\text{PF}_6]_{2n}$ (**1**) and $[\text{Ag}(\text{abpy})]_n[\text{PF}_6]_n$ (**2**) were synthesized and characterized by single crystal X-ray diffraction study and infrared spectroscopy. There are different types of supra-molecular interactions like $\pi\cdots\pi$ stacking, anion $\cdots\pi$, C-H \cdots anion and M \cdots anion present in both compounds leading to the formation of two dimensional (2D) architectures. The polymers in the solid state are conductors of electricity. The relative conductivity of **1** is greater than that of **2** and the optical band gap obtained from the UV-vis spectroscopy of **1** (3.14 eV) is lower than that of **2** (3.41 eV). The conductivity of **1** containing free NN chelating site increases significantly when it was doped with Cu^{2+} ions. The incorporation of Cu^{2+} ions in **1** was investigated by EPR spectroscopy and SEM and EDS study. The red shift of the λ_{max} further infers that the band gap of **1** decreases in the presence of Cu^{2+} ions.

Conflicts of interest

There are no conflicts of interest to declare.

Acknowledgements

The financial support received from SERB-DST (EMR/2016/005222), New Delhi, India is gratefully acknowledged. S. Maity is a DSK PDF fellow of UGC (CH/18-19/0029).

Notes and references

- O. M. Yaghi, M. O'Keeffe, N. W. Ockwig, H. K. Chae, M. Eddaoudi and J. Kim, *Nature*, 2003, **423**, 705–714.
- B. Moulton and M. J. Zaworotko, *Chem. Rev.*, 2001, **101**, 1629–1658.
- D. J. Levine, T. Runčevski, M. T. Kapelewski, B. K. Keitz, J. Oktawiec, D. A. Reed, J. A. Mason, H. Z. H. Jiang, K. A. Colwell, C. M. Legendre, S. A. Long and J. R. FitzGerald, *J. Am. Chem. Soc.*, 2016, **138**, 10143–10150.
- N. L. Rosi, J. Eckert, M. Eddaoudi, D. T. Vodak, J. Kim, M. O'Keeffe and M. O. Yaghi, *Science*, 2003, **300**, 1127–1129.
- R.-W. Huang, Y.-S. Wei, X.-Y. Dong, X.-H. Wu, C.-X. Du, S.-Q. Zang and T. C. W. Mak, *Nat. Chem.*, 2017, **9**, 689–697.
- S.-S. Zhang, X. Wang, H.-F. Su, L. Feng, Z. Wang, W.-Q. Ding, V. A. Blatov, M. Kurmoo, C.-H. Tung, D. Sun, L. Sun and L.-S. Zheng, *Inorg. Chem.*, 2017, **56**, 11891–11899.
- B. Dutta, C. Sinha and M. H. Mir, *Chem. Commun.*, 2019, 55, 11049–11051.
- H. Sakamoto, T. Chiba, M. Takata, Y. Kawazoe and Y. Mita, *Nature*, 2005, **436**, 238.
- N. Ahmad, H. A. Younus, A. H. Chughtai and F. Verpoort, *Chem. Soc. Rev.*, 2015, **44**, 9–25.
- Y.-Z. Chen and H.-L. Jiang, *Chem. Mater.*, 2016, **28**, 6698–6704.
- K. S. Min and M. P. Suh, *J. Am. Chem. Soc.*, 2000, **122**, 6834.
- R. Custelcean and B. A. Moyer, *Eur. J. Inorg. Chem.*, 2007, 1321–1340.
- J. R. Li, J. Sculley and H. C. Zhou, *Chem. Rev.*, 2012, **112**, 869–932.
- Y. Wang, P. Cheng, Y. Song, D. Z. Liao and S. P. Yan, *Chem. – Eur. J.*, 2007, **13**, 8131–8138.
- S.-Q. Deng, X.-J. Mo, S.-R. Zheng, X. Jin, Y. Gao, S.-L. Cai, J. Fan and W.-G. Zhang, *Inorg. Chem.*, 2019, **58**, 2899–2909.
- S. Sharma, A. V. Desai, B. Joarder and S. K. Ghosh, *Angew. Chem., Int. Ed.*, 2020, **132**, 7862–7866.
- B. L. Schottel, H. T. Chifotides, M. Shatruk, A. Chouai, L. M. Pérez, J. Bacsá and K. R. Dunbar, *J. Am. Chem. Soc.*, 2006, **128**, 5895–5912.
- M. Ko, L. Mendecki and K. A. Mirica, *Chem. Commun.*, 2018, **54**, 7873–7891.
- H.-N. Wang, X. Meng, L.-Z. Dong, Y. Chen, S.-L. Li and Y.-Q. Lan, *J. Mater. Chem. A*, 2019, **7**, 24059–24091.
- K. Zhao, W. Zhu, S. Liu, X. Wei, G. Ye, Y. Sua and Z. He, *Nanoscale Adv.*, 2020, **2**, 536–562.
- M. Bardaji, M. Barrio and P. Espinet, *Dalton Trans.*, 2011, **40**, 2570.
- S. Frantz, J. Fiedler, I. Hartenbach, T. Schleid and W. Kaim, *J. Organomet. Chem.*, 2004, **689**, 3031–3039.
- W. Kaim, *Coord. Chem. Rev.*, 2001, **219–221**, 463–488.
- B. Sarkar, S. Patra, J. Fiedler, R. B. Sunoj, D. Janardanan, S. M. Mobin, M. Niemeyer, G. K. Lahiri and W. Kaim, *Angew. Chem., Int. Ed.*, 2005, **44**, 5655–5658.
- N. E. Clayman, M. A. Manuppil, B. D. Matson, S. Wang, A. H. Slavney, R. Sarangi, H. I. Karunadasa and R. M. Waymouth, *Inorg. Chem.*, 2019, **58**, 10856–10860.
- N. E. Clayman, M. A. Manuppil, D. Umeyama, A. E. Rudenko, H. I. Karunadasa and R. M. Waymouth, *Angew. Chem., Int. Ed.*, 2018, **57**, 1–5.
- C. S. Campos-Fernández, J. R. Galán-Mascarós, B. W. Smucker and K. R. Dunbar, *Eur. J. Inorg. Chem.*, 2003, 988–994.
- S. Maity, S. Kundu, T. Weyhermiller and P. Ghosh, *Inorg. Chem.*, 2015, **54**, 1300–1313.

Communication

- 29 A. Pathak, J.-W. Shen, M. Usman, L.-F. Wei, S. Mendiratta, Y.-S. Chang, B. Sainbileg, C.-M. Ngue, R.-S. Chen, M. Hayashi, T.-T. Luo, F.-R. Chen, K.-H. Chen, T.-W. Tseng, L.-C. Chen and K.-L. Lu, *Nat. Commun.*, 2019, **10**, 1721.
- 30 K. Naskar, A. Dey, S. Maity, P. P. Ray, P. Ghosh and C. Sinha, *Inorg. Chem.*, 2020, **59**, 5518–5528.
- 31 A. Dey, S. Middya, R. Jana, M. Das, J. Datta, A. Layek and P. P. Ray, *J. Mater. Sci.: Mater. Electron.*, 2016, **27**, 6325–6335.



Ramakrishna Mission Residential College (Autonomous)
Kolkata 700103, WB, India

Collaborative research in synthetic and structural organic chemistry
Number 16

Institute 1: Ramakrishna Mission Residential College (Autonomous)

Concerned Faculty: Dr. Prasanta Ghosh, Dept of Chemistry

&

**Institute 2: Department of Chemistry, Rishi Bankim Chandra College
for Women, Naihati, 24-Parganas (N), Pin-743165, India**

Concerned Faculty: Dr. Suven Das

&

**Institute 3: Department of Chemistry, Rishi Bankim Chandra Evening College, Naihati,
24-Parganas (N), Pin-743165, India**

Concerned Faculty: Dr. Arpita Dutta

Period of Investigation: 01-06-2019 to 30-06-2020

Project: Ninhydrin-phenol derivatives and reaction with *o*-phenylenediamine

Output: The result was published in a journal of international repute

**Publication: Base Promoted Tandem Cyclization of *o*-Phenylenediamine with
Ninhydrin-phenol Adducts: An Unprecedented Route to Phenol Appended
Isoindolo[2,1-*a*]quinoxaline Fluorophore**

Suven Das, Suvendu Maity, Prasanta Ghosh, Bijan K. Paul and Arpita Dutta
ChemistrySelect, 2019, 04, 2656-2662. DOI: 10.1002/slct.201804069

Dr. Prasanta Ghosh

Dr. Suven Das

Dr. Arpita Dutta

Dr. Prasanta Ghosh

Associate Professor
Department of Chemistry
R.K.M. Residential College (Autonomous)
Narendrapur, Kolkata-700103

Organic & Supramolecular Chemistry

Base Promoted Tandem Cyclization of *o*-Phenylenediamine with Ninhydrin-phenol Adducts: An Unprecedented Route to Phenol Appended Isoindolo[2,1-*a*]quinoxaline FluorophoreSuven Das,^{*,[a]} Suvendu Maity,^[b] Prasanta Ghosh,^[b] Bijan K. Paul,^[c] and Arpita Dutta^[d]

Synthesis of fluorescent molecules has drawn considerable attention due to their potential applications in life and material sciences. Here we report a metal-free approach to a new class of fluorophore, namely, 6-(2-hydroxyaryl)isoindolo[2,1-*a*]quinoxalin-11(5*H*)-ones exploiting ninhydrin ring system via base promoted tandem cyclization. The readily obtainable phenolic adducts of ninhydrin undergoes smooth reaction with *o*-phenylenediamine in refluxing ethylene glycol/Et₃N via breaking of C–C bond, N-insertion, followed by heterocyclization to furnish the fully unsaturated isoindoloquinoxaline framework. Structures of the products are in good agreement with their IR, ¹HNMR, ¹³CNMR, and mass spectral data. The photophysical properties of the synthesized compounds were studied by UV-vis absorption and fluorescence spectroscopic techniques under ambient conditions, and the results reveal an interesting property of large Stokes shift.

Introduction

Among the large arsenal of heterocycles, isoindoles^[1] and quinoxalines^[2] are two important structural motifs with many applications in the field of pharmaceutical and material sciences. They are found in wide array of bioactive natural products and synthetic compounds.^[3] In particular, quinoxaline derivatives are well known for their diverse biological activities including antibiotic,^[4a] antimalarial,^[4b] P13Ka inhibitors,^[4c] multiple drug-resistance antagonists^[4d] and antineoplastic activity.^[4e] Quinoxaline scaffolds linked with pyridine or indole system

have been reported to exhibit antitumor and other biological properties (1, 2, 3, Figure 1).^[5] Usually polycyclic nitrogen heterocycles with planar structure are well known chemotherapeutic agents.^[6] Diana and co-workers revealed the potential of isoindole fused quinoxaline scaffolds to display antiproliferative activity against human cancer cells as well as inhibitors of tubulin polymerase and topoisomerase I (4, 5, Figure 1).^[7] Despite convincing pharmacological profile, methods of synthesis of isoindolo[2,1-*a*]quinoxaline framework are very limited, requiring harsh reaction conditions or complicated steps.^[7,8] For example, Dyker and co-workers reported the reaction of *o*-alkynylbenzaldehydes with *o*-phenylenediamine which led to a mixture of products where isoindolo[2,1-*a*]quinoxaline isolated in low yields after two days refluxing in nitrobenzene (Scheme 1a).^[8a] Another synthetic route demonstrated by Diana's group constitutes refluxing of 2-(2'-aminoaryl)-1-cyanoisoindole intermediate in acetic acid, employing highly toxic KCN in the intermediate formation step (Scheme 1b).^[7a] The tetracyclic core could also be constructed, as reported by Potikha, via prolonged heating of N-(2-amino-phenyl)isoindoles with formic acid (Scheme 1c).^[8b] However, these methods are not efficient enough for the synthesis of isoindoloquinoxaline fluorophores. Therefore, development of straightforward protocol to access this class of nitrogen-fused heterocyclic system with photophysical properties is of great significance.

Fluorophores, on the other hand, are important class of compounds with versatile applications. In recent time, synthesis of fluorescent molecules has become most active research area because of their immense influence in the field of chemistry, life sciences, and material sciences.^[9] Especially, hybrid heterocyclic systems with strong fluorescence are intriguing as they are frequently used as molecular probes in biochemical research.^[10] Since isoindolo[2,1-*a*]quinoxaline motif exhibits anticancer activity, the similar system enriched with fluorescence might serve as powerful tool for monitoring interactions with target molecules. Moreover, choice of appropriate non-toxic and non-volatile solvent for a desired synthesis is very crucial from the green chemistry point of view.^[11] In continuation of our ongoing efforts in the development of potentially bioactive heterocyclic skeletons from ninhydrin,^[12] herein we report simple synthesis of isoindolo[2,1-*a*]quinoxaline derivatives involving ethylene glycol as green solvent. The synthesized compounds are highly fluorescent with the

[a] Dr. S. Das
Department of Chemistry, Rishi Bankim Chandra College for Women,
Naihati, 24-Parganas (N), Pin-743165, India
E-mail: suvenchem@yahoo.co.in

[b] Dr. S. Maity, Dr. P. Ghosh
Department of Chemistry, R K Mission Residential College, Narendrapur,
Kolkata-103, India

[c] Dr. B. K. Paul
Department of Chemistry, Mahadevananda Mahavidyalaya, Barrackpore,
Kolkata 700 120, India

[d] Dr. A. Dutta
Department of Chemistry, Rishi Bankim Chandra Evening College, Naihati,
24-Parganas (N), Pin-743165, India

Supporting information for this article is available on the WWW under
<https://doi.org/10.1002/slct.201804069>

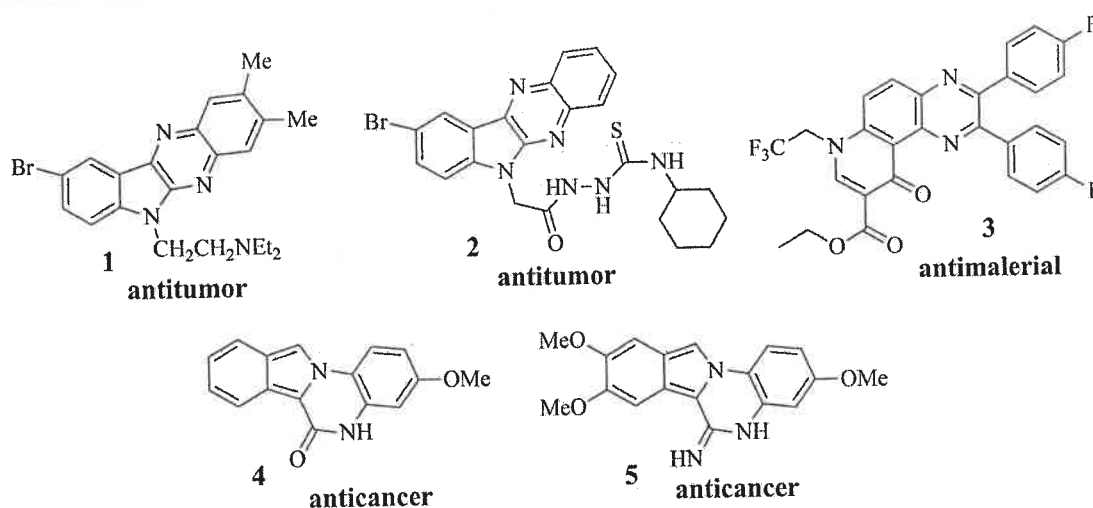
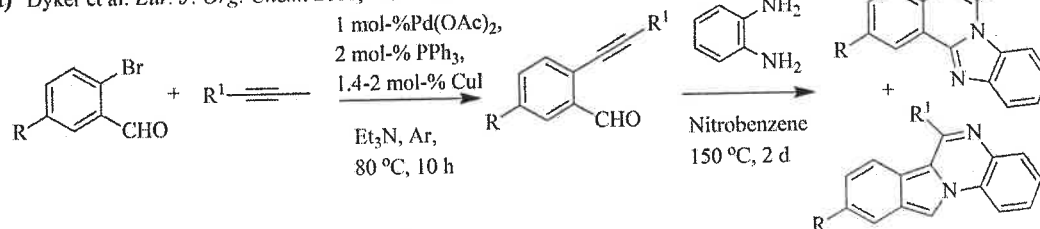


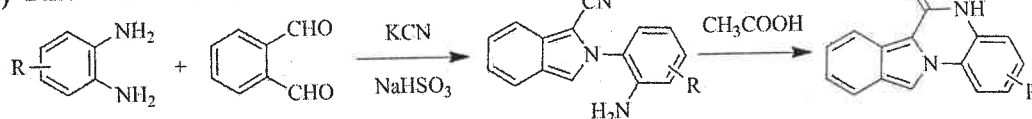
Figure 1. Biologically active heteroaryl fused quinoxaline derivatives

Previous works

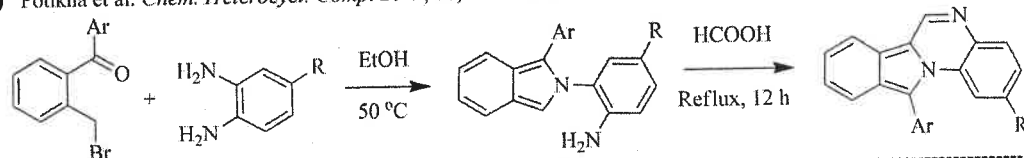
a) Dyker et al: *Eur. J. Org. Chem.* **2000**, 1433–1441



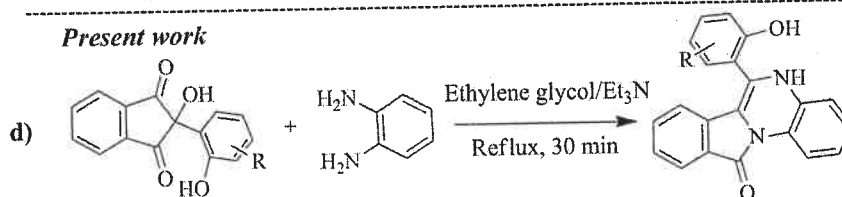
b) Diana et al: *J. Med. Chem.* **2008**, 51, 2387–2399



c) Potikha et al: *Chem. Heterocycl. Comp.* **2012**, 48, 1033–1042



Present work



Scheme 1. Different synthetic routes to isoindolo[2,1-*a*]quinoxaline core

emission wavelength in the range 540–550 nm. To our knowledge, this is the first report of development of isoindoloquinoxaline scaffold involving ninhydrin skeleton and exploration of their photophysical properties. It is worth noting that several quinoxalin-based compounds have been reported to exhibit fluorescence property with varied applications.^[13]

Results and discussion

Although ninhydrin is a valuable compound in biochemical and forensic sciences,^[14] it has also been widely applied as versatile building block for the construction of diverse heterocyclic scaffolds for the past several years.^[15] In fact, C-2 arylated ninhydrin is an effective synthon for various biologically



Ramakrishna Mission Residential College (Autonomous)
Kolkata 700103, WB, India

Collaborative research in synthetic and structural organic chemistry
Number 17

Institute 1: Ramakrishna Mission Residential College (Autonomous)

Concerned Faculty: Dr. Prasanta Ghosh, Dept of Chemistry

&

Institute 2: Department of Chemistry, Rishi Bankim Chandra College

for Women, Naihati, 24-Parganas (N), Pin-743165, India

Concerned Faculty: Dr. Suven Das

&

Institute 3: Department of Chemistry, Rishi Bankim Chandra Evening College, Naihati,

24-Parganas (N), Pin-743165, India

Concerned Faculty: Dr. Arpita Dutta

Period of Investigation: 01-05-2017 to 31-12-2017

Project: Ninhydrin-phenol derivatives and reaction with *o*-phenylenediamine

Output: The result was published in a journal of international repute

Publication: Insertion of the *o*-Aminophenol Core into Ninhydrin–Phenol Adducts:
Migration of Ninhydrin Carbon Leading to *N*-Phenylbenzoate-Substituted Phthalimides

Suven Das, Arpita Dutta, Suwendu Maity, Prasanta Ghosh and Kalachand Mahali
Synlett, 2018, 29, 581-584. DOI: 10.1055/s-0036-1589146

Dr. Prasanta Ghosh

Dr. Suven Das

Dr. Arpita Dutta

Dr. Prasanta Ghosh

Associate Professor

Department of Chemistry

R.K.M. Residential College (Autonomous)

Narendrapur, Kolkata-700103

Insertion of the *o*-Aminophenol Core into Ninhydrin–Phenol Adducts: Migration of Ninhydrin Carbon Leading to *N*-Phenylbenzoate-Substituted Phthalimides

Suven Das^{a*}

Arpita Dutta^b

Suvendu Maity^c

Prasanta Ghosh^c

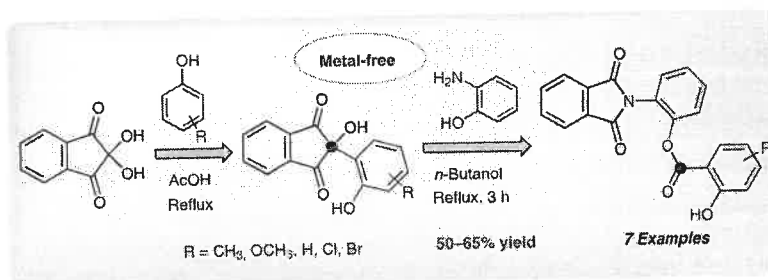
Kalachand Mahali^d

^a Department of Chemistry, Rishi Bankim Chandra College for Women, Naihati, 24-Parganas (N), Pin-743165, India
suvenchem@yahoo.co.in

^b Department of Chemistry, Rishi Bankim Chandra Evening College, Naihati, 24-Parganas (N), Pin-743165, India

^c Department of Chemistry, R K Mission Residential College, Narendrapur, Kolkata-103, India

^d Department of Chemistry, University of Kalyani, Nadia-741235, India



Received: 22.09.2017

Accepted after revision: 08.11.2017

Published online: 19.12.2017

DOI: 10.1055/s-0036-1589146; Art ID: st-2017-d0704-1

Abstract An unexpected migration of a ninhydrin carbon bearing a phenolic subunit has been observed when phenolic adducts of ninhydrin reacted with 2-aminophenol in butan-1-ol at the reflux temperature. The products were unambiguously assigned as 2-(1,3-dioxoisindolin-2-yl)phenyl benzoates on the basis of NMR spectroscopy and X-ray crystallographic analysis.

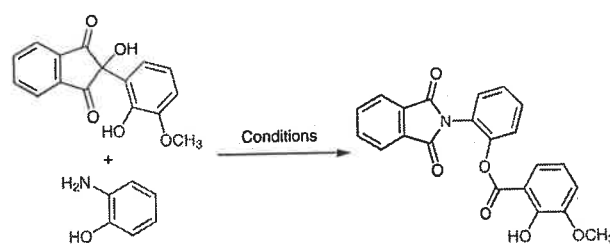
Key words phenols, rearrangement, heterocycles, migration, insertion

Isindole and its derivatives are found in a variety of naturally occurring alkaloids and pharmaceutical compounds.¹ Among them, *N*-substituted phthalimides [1*H*-isindole-1,3(2*H*)-diones] have been considered as attractive synthetic targets due to their diverse biological activities² and their applications as functional materials.³ Additionally, phthalimide photochemistry has been applied to chiral synthesis,⁴ as well as in the synthesis of macrocyclic polyethers.⁵ Recently, some substituted phthalimide derivatives have been reported to exhibit color-tunable luminescence.⁶ Therefore, access to *N*-substituted phthalimides remains an important challenge in current organic chemistry.

On the other hand, ninhydrin [2,2-dihydroxy-1*H*-indene-1,3(2*H*)-dione] is a compound with two hydroxy groups attached to the same carbon atom, which is flanked by two carbonyl groups. Adducts of ninhydrin have attracted considerable attention due to their applicability as building blocks in the development of various heterocyclic scaffolds.⁷ We recently reported the synthesis of benzimidazoisindole and benzodiazonine frameworks from ninhy-

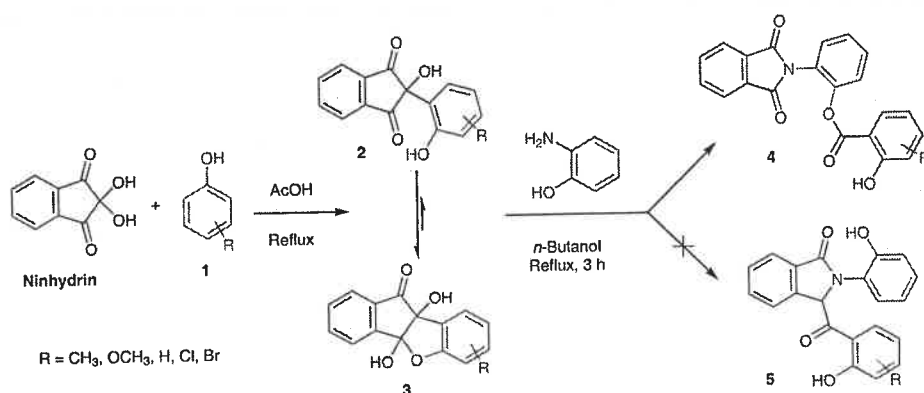
drin–phenol adducts.⁸ Consequently, it was thought of interest to explore the reactivity of ninhydrin adducts towards 2-aminophenol. However, the reaction did not afford the expected 3-(2-hydroxybenzoyl)-2-(2-hydroxyphenyl)isindolin-1-one **5**,⁹ but instead we observed an insertion of the 2-aminophenol core into the adducts in conjunction with a migration of the ninhydrin carbon to the aminophenol oxygen (Scheme 1). Although several related migration reactions have been documented for different

Table 1 Optimization of the Synthesis of Benzoate **4a**



Entry	Solvent	Temp.	Time (h)	Yield (%)
1	MeOH	r.t. (25 °C)	24	NR ^a
2	EtOH	r.t. (25 °C)	24	NR
3	BuOH	r.t. (25 °C)	24	NR
4	EtOH	reflux	8	NR
5	PrOH	reflux	8	trace
6	BuOH	reflux	3	60
7	MeCN	reflux	8	NR
8	toluene	reflux	8	NR

^a NR = no reaction.



Scheme 1 Synthesis of 2-(1,3-dioxoisindolin-2-yl)phenyl benzoates **4**

systems,¹⁰ to the best of our knowledge, migration of the ninhydrin ring carbon bearing a phenol is hitherto unreported. Here, we report an unprecedented synthesis of 2-(1,3-dioxoisindolin-2-yl)phenyl benzoates **4** from 2-aminophenol and ninhydrin–phenol adducts through this rearrangement.

The ninhydrin–phenol adducts, 2-hydroxy-2-(2-hydroxyaryl)-1,3-indanediones **2**, were prepared as reported previously¹¹ by refluxing the corresponding phenols **1** with ninhydrin in glacial acetic acid. The resulting adducts preferentially remain in the cyclic hemiketal form **3**.^{11a,b} In the next step, we treated the ninhydrin–guaiacol adduct **2a** with 2-aminophenol in various solvents. The reaction did not proceed in methanol, ethanol or butan-1-ol at 25 °C (Table 1, entries 1–3), and no reaction occurred refluxing ethanol, even after eight hours (entry 4); however, traces of the product were isolated when the reactants were heated in propan-1-ol (entry 5). When the reaction was carried out in refluxing butan-1-ol, the unexpected rearrangement product 2-(1,3-dioxo-1,3-dihydro-2*H*-isoindol-2-yl)phenyl 2-hydroxy-3-methoxybenzoate (**4a**) was isolated in 60%

yield within three hours (entry 6).¹² When the aprotic solvents toluene and acetonitrile were used, the reaction failed to give product **4a** (entries 7 and 8).

Under the optimized conditions, various substituted phenolic adducts **2b–g** gave products **4b–g** (Figure 1). Products **4a–g** were all obtained smoothly as precipitates from the reaction mixture in yields of 50–65%. Notably, simple filtration afforded phthalimide derivatives **4a–g** in a pure form, and no byproducts were detected in the filtrate.

The IR spectrum of compound **4a** exhibited bands at 1720 and 1688 cm^{−1} for the ester and imide carbonyl groups, respectively. In the ¹H NMR spectrum, the phenolic OH proton appeared as a singlet at δ = 9.89. Aromatic protons were observed in the range δ = 7.94–6.75. The ¹³C NMR spectrum showed distinct signals in agreement with the proposed structure. The structure of compound **4a** was supported by mass spectrometry, which showed a molecular ion [M + Na]⁺ at m/z = 412. The structure of **4a** was finally and unambiguously confirmed by single-crystal X-ray analysis (Figure 2).¹³

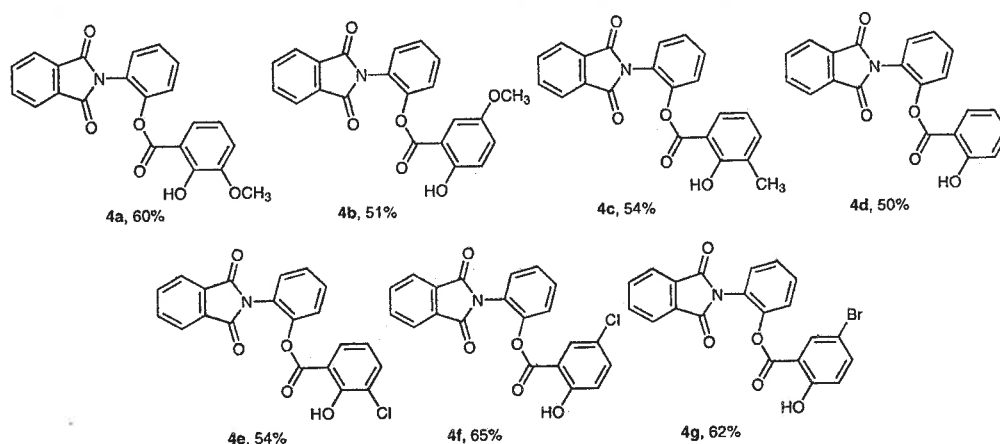


Figure 1 Synthesized 2-(1,3-dioxoisindolin-2-yl)phenyl benzoate derivatives **4a–g**



Ramakrishna Mission Residential College (Autonomous)

Kolkata 700103, WB, India

**Collaborative research in synthetic and structural organic chemistry
Number 18**

Institute 1: Ramakrishna Mission Residential College (Autonomous)

Concerned Faculty: Dr. Prasanta Ghosh, Dept of Chemistry

&

Institute 2: Department of Chemistry, Rishi Bankim Chandra College

for Women, Naihati, 24-Parganas (N), Pin-743165, India

Concerned Faculty: Dr. Suven Das

&

Institute 3: Department of Chemistry, Rishi Bankim Chandra Evening College, Naihati,

24-Parganas (N), Pin-743165, India

Concerned Faculty: Dr. Arpita Dutta

Period of Investigation: 02-09-2018 to 30-08-2019

Project: Condensation of ninhydrin with phenols

Output: The result was published in a journal of international repute

**Publication: Condensation of ninhydrin with phenols: Regioselective
formation of diverse organic scaffolds and crystal structure studies**

Purak Das, Suvendu Maity, Prasanta Ghosh, Arpita Dutta and Suven Das

***J. Molecular Structure*, 2020, 1202, 127260. DOI: 10.1016/j.molstruc.2019.127260**

Dr. Prasanta Ghosh

Dr. Suven Das

Dr. Arpita Dutta

Dr. Prasanta Ghosh

Associate Professor

Department of Chemistry

R.K.M. Residential College (Autonomous)

Narendrapur, Kolkata-700103



Get Access

Journal of Molecular Structure

Volume 1202, 15 February 2020, 127260

Condensation of ninhydrin with phenols: Regioselective formation of diverse organic scaffolds and crystal structure studies

Purak Das ^a, Suwendu Maity ^b, Prasanta Ghosh ^b, Arpita Dutta ^c, Suven Das ^a

Show more

Outline | Share Cite

<https://doi.org/10.1016/j.molstruc.2019.127260>

Get rights and content

Highlights

- Ninhydrin-phenols assembly regioselectively delivered diverse organic scaffolds.
- Indanone, indenofuran, benzofuran, spirolactone skeleton generated tuning substitution and acidity of medium.
- X-ray crystal structure of two representative compounds analyzed.

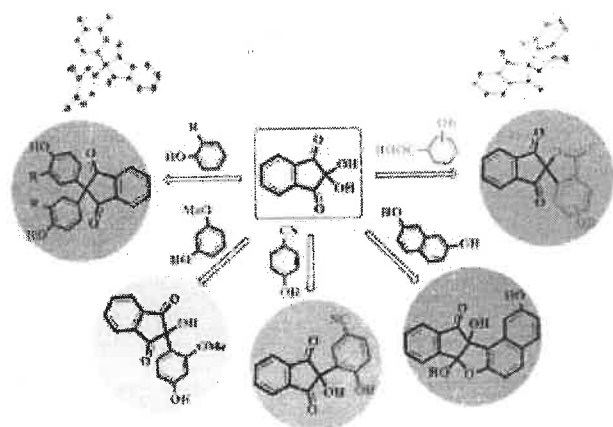
Abstract



Get Access

other hand, *ortho*-substituted phenols like *o*-cresol, guaiacol, *o*-chloro/iodophenol condense with ninhydrin to accomplish *para* selective diarylated adducts **5a-d**, whereas 3-methoxy phenol provides corresponding monoarylated adduct **5e** as the major product. Different hydroxy benzoic acids deliver versatile scaffolds like diarylated indanone, indenofuran, benzofuran or spirolactone **7a-e** depending upon the substitution pattern and acidity of the reaction medium. All the compounds are characterized by ^1H and ^{13}C NMR spectra. In the solid state, scissors-shaped molecule **5a** has been found to form inclusion complex with disordered *o*-cresol molecule and function as building unit of supramolecular network. In the crystal structure of spirolactone **7d**, anti-parallel motif of dipolar \cdots dipolar ($\text{C}=\text{O}^{(\delta-)} \cdots \text{C}^{(\delta+)}=\text{O}$) interaction results ladder-like arrangement.

Graphical abstract


[Download : Download high-res image \(212KB\)](#)
[Download : Download full-size image](#)

[Previous](#)
[Next](#)


Keywords

Ninhydrin; Phenols; Regioselectivity; NMR; Crystal structure



Ramakrishna Mission Residential College (Autonomous)

Kolkata 700103, WB, India

**Collaborative research in synthetic and structural organic chemistry
Number 19**

Institute 1: Ramakrishna Mission Residential College (Autonomous)

Concerned Faculty: Dr. Prasanta Ghosh, Dept of Chemistry

&

Institute 2: Department of Chemistry, Rishi Bankim Chandra College

for Women, Naihati, 24-Parganas (N), Pin-743165, India

Concerned Faculty: Dr. Suven Das

&

Institute 3: Department of Chemistry, Rishi Bankim Chandra Evening College, Naihati,

24-Parganas (N), Pin-743165, India

Concerned Faculty: Dr. Arpita Dutta

Period of Investigation: 01-01-2019 to 30-11-2019

Project: Self-assembly of the amino acid derivatives

Output: The result was published in a journal of international repute

**Publication: Fibril formation through self-assembly of a simple glycine derivative and
X-ray diffraction study**

Arpita Dutta, Suven Das, Purak Das, Suvendu Maity and Prasanta Ghosh

Zeitschrift Kristallographie - Crystalline M, 2020, 235, 47-51.

DOI: 10.1515/zkri-2019-0062

Dr. Prasanta Ghosh

Dr. Suven Das

Dr. Arpita Dutta

Dr. Prasanta Ghosh

Associate Professor

Department of Chemistry

R.K.M. Residential College (Autonomous)

Narendrapur, Kolkata-700103

Arpita Dutta*, Suven Das, Purak Das, Suwendu Maity and Prasanta Ghosh

Fibril formation through self-assembly of a simple glycine derivative and X-ray diffraction study

<https://doi.org/10.1515/zkri-2019-0062>

Received November 28, 2019; accepted January 5, 2020

Abstract: N-(N-benzoyl glycyl)-N,N'-dicyclohexylurea was synthesised by conjugating N-benzoyl glycine and dicyclohexylcarbodiimide (DCC) using triethylamine as base catalyst. A single crystal X-ray diffraction study reveals that the compound self-assembles into a supramolecular sheet structure by intermolecular N-H...O, C-H...O hydrogen bonding and non-bonding van der Waals interactions. A high resolution transmission electronic microscopic (HR-TEM) image of the compound exhibits formation of fibrils in the solid state.

Keywords: fibrils; glycine derivative; self-assembly; supramolecular sheet.

Introduction

In nature, various biological systems are the result of molecular self-assembly [1–4]. Supramolecular assemblies are often stabilised by hydrogen bonding, hydrophobic, hydrophilic interactions, π - π stacking etc [5, 6]. The design and synthesis of suitable molecular building blocks that self-assemble into desired supramolecular architectures is an active area of current research. Micro and nanoscale soft materials derived from amino acid based molecules are important for their versatile functionality. Construction of supramolecular sheet structures through self-assembly of small building blocks has attracted considerable attention for their diverse applications in the field of drug delivery, biosensing, 3D cell culture etc [7–10]. Several examples are available, where small peptide molecules are acting as suitable molecular building blocks for β -sheet self-assembly [11–15]. Very few reports are available where supramolecular structures

and morphological properties of small capped amino acid based molecules have been discussed. For example, *m*-aminobenzoic (non-coded amino acid) acid protected with Boc and N, N'-dicyclohexylurea was reported to adopt a supramolecular double helical motif in the solid state [16]. With these in mind, we wanted to explore the self-assembly and morphology of a small molecule derived from glycine. We have chosen glycine because it is a profuse biomonomer in nature as well as the smallest coded amino acid.

In this report, we prepared a compound, namely, N-(N-benzoyl glycyl)-N, N'-dicyclohexylurea **1** (Figure 1) and examined the formation of its supramolecular motif. Here, the N-terminal of glycine is intentionally protected by a benzoyl group to get an extra benefit to find order and directionality in the self-assembly process. Again two cyclohexyl groups in the C-terminal of glycine may provide hydrophobic interactions to promote the desired supramolecular structure. The title compound was synthesised by conjugating N-benzoyl glycine and dicyclohexylcarbodiimide (DCC) using triethylamine as base catalyst. The solid state structure of compound **1** was determined by single crystal X-ray diffraction. High resolution transmission electronic microscopy (HR-TEM) has also been employed to examine the morphological properties of the molecule.

Experimental

Synthesis

PhCO-Gly-OH (1.0 g, 5.6 mmol) was dissolved in 10 mL DMF, followed by dicyclohexylcarbodiimide (2.3 g, 8.4 mmol) and two drops of triethylamine were added and the reaction mixture was stirred at room temperature for 12 h. The reaction mixture was filtered and to the filtrate 20 mL of ethylacetate was added. The organic layer was washed with 1 N HCl (3 \times 30 mL), 1 M Na₂CO₃ solution (3 \times 30 mL) and brine, respectively. The solvent was then dried over anhydrous Na₂SO₄ and evaporated in *vacuo*, giving a white solid. Yield: 3.8 g (88%). Purification was done using silica gel as stationary phase and an ethyl acetate-petroleum ether mixture as the eluent. Single crystals were grown from methanol by slow evaporation and were stable at room temperature. Mp = 165–167 °C; ¹H NMR 500 MHz (DMSO-d₆, δ ppm): 8.65 (GlyNH, 1H, t, J = 5.5 Hz), 8.41 (Substituted urea NH, 1H, d, J = 8 Hz), 7.87–7.46 (Phenyl ring protons, 5H, m), 4.08 (C^oHs of Gly, 2H, d, J = 5.5 Hz), 3.95 (1H, m), 3.50 (1H, m), 1.83–1.69 (8H, m), 1.57–1.47 (4H, m), 1.00–1.32 (8H, m); ¹³C NMR 75 MHz (DMSO-d₆, δ ppm): 167.02,

*Corresponding author: Arpita Dutta, Department of Chemistry, Rishi Bankim Chandra Evening College, Naihati, 24-Parganas (N), Pin-743165, India, E-mail: arpitachem@yahoo.co.in

Suven Das and Purak Das: Department of Chemistry, Rishi Bankim Chandra College for Women, Naihati, 24-Parganas (N), Pin-743165, India

Suwendu Maity and Prasanta Ghosh: Department of Chemistry, R K Mission Residential College, Narendrapur, Kolkata-103, India

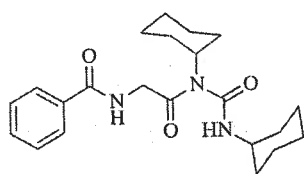


Fig. 1: Structure of compound 1.

166.90, 153.43, 134.49, 131.80, 128.76, 127.75, 53.89, 50.11, 42.13, 32.19, 30.71, 25.90, 25.59, 25.56, 24.85; DEPT-135: 42.13, 32.19, 30.71, 25.90, 25.60, 25.56, 24.85 (Negative).

Crystal structure determination

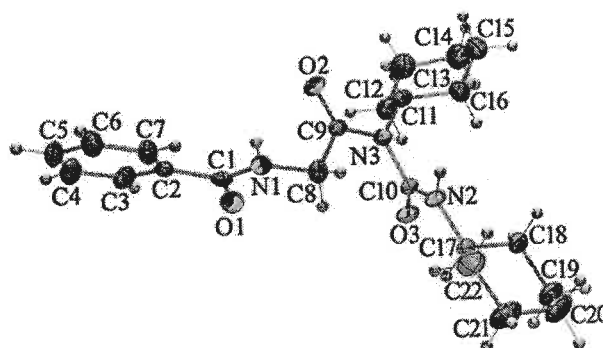
A single crystal suitable for X-ray diffraction of **1** was loaded on a Bruker AXS D8 QUEST ECO diffractometer and the diffraction data was collected using monochromatic Mo-target rotating-anode X-ray source and graphite monochromator (Mo-K α , $\lambda = 0.71073$ Å) with the ω and ϕ scan technique. The unit cell was determined using SMART [17], the diffraction data was integrated with the Bruker SAINT system [17] and the data was corrected for absorption using SADABS [17]. The structure was solved using SHELXS 97 [18] by Direct Methods and was refined by full matrix least squares based on F^2 using SHELXL-2018/3 [19]. All non-hydrogen atoms were refined anisotropically and the H atoms were included at calculated positions as riding atoms with C(sp²)-H distances of 0.93 Å and C(sp³)-H distances of 0.96 Å. Some low-angle reflections were excluded from the refinement as those were probably obscured by the beam stop. An ORTEP-plot and a packing diagram were generated with ORTEP-3 for Windows [20]. WinGX [20] was used to prepare the material for publication. CCDC 1906687 contains supplementary crystallographic data for this paper.

High resolution transmission electron microscopy (HR-TEM)

The morphology of our compound was investigated using high resolution transmission electron microscopy (HRTEM). A methanol solution of compound **1** (2 mM) was incubated over night at room temperature. TEM studies of the peptides were done using a small amount of the solution of the corresponding compounds on carbon coated copper grid (300 mesh) by slow evaporation and allowed to dry in *vacuum* at room temperature. An image was taken by JEOL JEM-2100.

Results and discussion

Compound **1** crystallizes in the orthorhombic space group $P2_12_12_1$ with one molecule in crystallographic asymmetric unit (Figure 2, Table 1). The molecule adopts an extended conformation characterized by the backbone torsion angle $\phi = 79.9(7)$ (C1-N1-C8-C9) and $\psi = -161.9(5)$ (N1-C8-C9-N3) at Gly (Figure 2, Table 2). There is an intramolecular C-H...O interaction [C(11)-H(11)...O(2), 2.34 Å] between

Fig. 2: ORTEP Diagram of compound **1** with thermal displacement ellipsoids shown at 25% probability.Tab. 1: Crystal data collection and structure refinement for **1**.

Crystal data	Compound 1
CCDC reference number	1906687
Empirical formula	C ₂₂ H ₃₁ N ₃ O ₃
Moiety formula	C ₂₂ H ₃₁ N ₃ O ₃
Formula weight	385.50
Crystal system	Orthorhombic
Space group	$P2_12_12_1$
Colour, habit	Colourless
Size, mm	0.20 × 0.19 × 0.17
Unit cell dimensions	
	$a = 8.9656(4)$
	$b = 13.0082(6)$
	$c = 19.0030(9)$
Volume Å ³	2216.25(18)
Z	4
Density (calculated), g/m ³	1.16
Absorption coefficient (mm ⁻¹)	0.1
F(000)	832
Data collection	
Temperature (K)	294(2)
Theta range for data collection	2.960°–24.994°
Index ranges	
	$-10 \leq h \leq 10$
	$-15 \leq k \leq 15$
	$-22 \leq l \leq 22$
Reflections collected	26,938
Unique reflections	2414
Observed reflections [$>2\sigma(I)$]	3647
R_{int}	0.0834
Completeness to θ (%)	24.994°, 99.2
Absorption correction	Multi-scan (SADABS; Sheldrick, 2000)
	$T_{min} = 0.978$, $T_{max} = 0.981$
Refinement	
Refinement method	Full-matrix least-squares on F^2
Data/restraints/parameters	3877/0/261
Goodness-of-fit on F^2	1.061
Final R indices [$I > 2\sigma(I)$]	$R_1 = 0.0768$, $wR_2 = 0.1528$
R indices (all data)	$R_1 = 0.1336$, $wR_2 = 0.1790$
Largest diff. peak and hole	0.22 and -0.20 e ⁻ Å ⁻³



Ramakrishna Mission Residential College (Autonomous)

Kolkata 700103, WB, India

Collaborative research in synthetic and structural organic chemistry

Number 20

Institute 1: Ramakrishna Mission Residential College (Autonomous)

Concerned Faculty: Dr. Prasanta Ghosh, Dept of Chemistry

&

Institute 2: Department of Chemistry, Rishi Bankim Chandra College

for Women, Naihati, 24-Parganas (N), Pin-743165, India

Concerned Faculty: Dr. Suven Das

&

Institute 3: Department of Chemistry, Rishi Bankim Chandra Evening College, Naihati,

24-Parganas (N), Pin-743165, India

Concerned Faculty: Dr. Arpita Dutta

Period of Investigation: 01-04-2017 to 31-04-2018

Project: Polyheterocycles derivatives from ninhydrin

Output: The result was published in the journal of international repute

**Publication: Benzimidazole-based polyheterocycles from ninhydrin: Synthesis, X-ray
crystal structure and photophysical property**

Suven Das, Purak Das, Suvendu Maity, Prasanta Ghosh, Bijan K. Paul and Arpita Dutta

***Journal of Molecular Structure*, 2018, 1168, 234-241. DOI: 10.1016/j.molstruc.2018.05.033**

Dr. Prasanta Ghosh

Dr. Suven Das

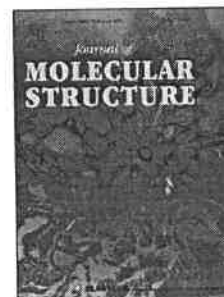
Dr. Arpita Dutta

Dr. Prasanta Ghosh
Associate Professor
Department of Chemistry
R.K.M. Residential College (Autonomous)
Narendrapur, Kolkata-700103

Accepted Manuscript

Benzimidazole-based polyheterocycles from ninhydrin: Synthesis, X-ray crystal structure and photophysical property

Suven Das, Purak Das, Suvendu Maity, Prasanta Ghosh, Bijan K. Paul, Arpita Dutta



PII: S0022-2860(18)30593-3

DOI: 10.1016/j.molstruc.2018.05.033

Reference: MOLSTR 25206

To appear in: *Journal of Molecular Structure*

Received Date: 16 March 2018

Revised Date: 8 May 2018

Accepted Date: 9 May 2018

Please cite this article as: S. Das, P. Das, S. Maity, P. Ghosh, B.K. Paul, A. Dutta, Benzimidazole-based polyheterocycles from ninhydrin: Synthesis, X-ray crystal structure and photophysical property, *Journal of Molecular Structure* (2018), doi: 10.1016/j.molstruc.2018.05.033.

This is a PDF file of an unedited manuscript that has been accepted for publication. As a service to our customers we are providing this early version of the manuscript. The manuscript will undergo copyediting, typesetting, and review of the resulting proof before it is published in its final form. Please note that during the production process errors may be discovered which could affect the content, and all legal disclaimers that apply to the journal pertain.

Benzimidazole-based polyheterocycles from ninhydrin: Synthesis, X-ray crystal structure and photophysical property

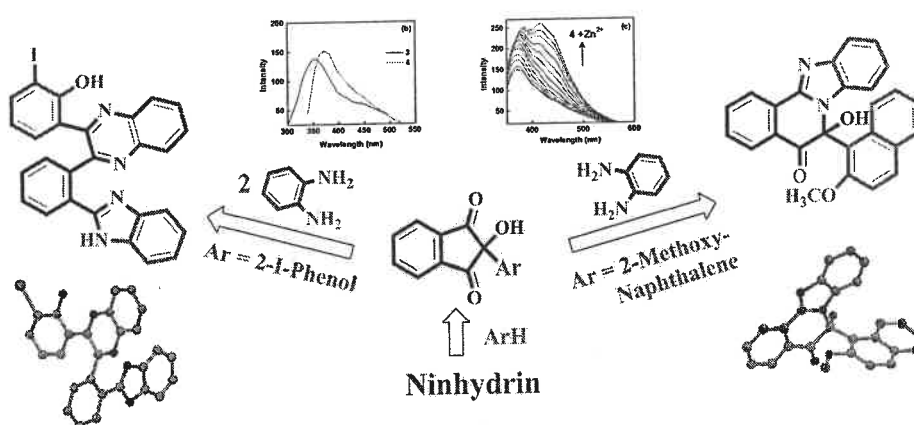
Suven Das^{a,*}, Purak Das^a, Suwendu Maity^b, Prasanta Ghosh^b, Bijan K. Paul^c, Arpita Dutta^d

^a Department of Chemistry, Rishi Bankim Chandra College for Women, Naihati, 24-Parganas (N), Pin-743165, India, e-mail: suvenchem@yahoo.co.in

^b Department of Chemistry, R K Mission Residential College, Narendrapur, Kolkata-103, India

^c Department of Chemistry, Mahadevananda Mahavidyalaya, Barrackpore, Kolkata 700 120, India

^d Department of Chemistry, Rishi Bankim Chandra Evening College, Naihati, 24-Parganas (N), Pin-743165, India



Abstract:

Ninhydrin was successfully employed to develop two different benzimidazole-embedded heterocyclic skeletons via reaction of arylated ninhydrin and *o*-phenylenediamine under acidic condition. While ninhydrin adduct of 2-iodophenol consumed two equivalent of *o*-phenylenediamine to furnish benzimidazole linked quinoxaline skeleton, under same reaction conditions corresponding 2-methoxynaphthalene adduct afforded benzimidazo[2,1-*a*]isoquinolinone framework. The hybrid heterocycles were identified as 2-(3-(2-(1*H*-benzo[*d*]imidazol-2-yl)phenyl)quinoxalin-2-yl)-6-iodophenol **3** and 6-hydroxy-6-(2-methoxynaphthalen-1-yl)benzo[4,5]imidazo[2,1-*a*]isoquinolin-5(6*H*)-one **4** by IR, NMR and single crystal X-ray diffraction studies. Fluorescence measurements reveal that compound **3** and **4** display differential fluorescence behaviour, particularly towards the presence of Zn²⁺ ion.

Keywords: Ninhydrin, Heterocycles, Benzimidazole, X-ray diffraction, Fluorescence